

Ph.D. Thesis

Perturbative quantities from Lattice formulations

(格子場の理論に基づく摂動的な物理量の計算)

Katsumasa Nakayama

Department of Physics, Nagoya University, Nagoya

KEK Theory Center, High Energy Accelerator Research Organization (KEK)

February 25, 2019

Abstract

We study the lattice calculation for the extraction of perturbative quantities such as the strong coupling constant α_s and quark mass. The lattice formulation with recently developed procedures and fine lattice spacings helps us to extract these fundamental parameters of the quantum field theory, including the Standard Model. The calculation based on the lattice formulation provides more precise numerical results, which are required in future experiments to test the Standard Model and search for physics beyond the Standard Model.

In this thesis, we explain lattice Quantum Chromo-Dynamics (QCD) with the Monte-Carlo method to determine the charm quark mass and the strong coupling constant by the moment method which uses short distance current-current correlator interaction. Short distance information can determine perturbative parameters, especially charm quark mass from time-moment of charmonium.

We also test perturbative expansion of Dirac spectral density in $O(\alpha_s^4)$ precision with the stochastic method. In order to reduce the discretization effect, we also introduce a generalization of domain-wall fermion formulation which is a good approximation of the physical properties on the lattice.

CONTENTS

I. Introduction	7
II. Lattice QCD and fermion formulations	10
A. Fermion formulations on the lattice	11
1. Non-local action	13
2. Non-hermitian action	14
3. Doubler identified action	15
4. Chiral symmetry broken action	17
5. Ginsparg-Wilson fermion	20
B. Overlap and Domain wall fermion	20
C. Generalized Pauli-Villars mass and discretization effects	28
III. Charm quark mass and the strong coupling constant from moments	35
A. Temporal moments	37
1. Moments in the perturbation and experiments	37
2. Formulae for the extraction of m_c and α_s	40
B. Lattice details	43
C. Vector current correlator and experimental data	45
D. Pseudoscalar current correlator	48
E. Estimates of systematic errors	51
1. Truncation of perturbative expansion	53
2. Non-perturbative corrections	54
3. dynamical charm quark	54
F. Determination of $m_c(\mu)$ and $\alpha_s(\mu)$	55
G. Summary	59
IV. Perturbative expansion of Dirac eigenvalue density	62
A. Dirac eigenvalue density	64
B. Perturbative formulae for Dirac spectral density	69
C. Discretization effects with lattice domain-wall fermion	71
D. Lattice calculation	76

1. Lattice ensembles	76
2. Stochastic calculation of the spectral density	76
E. Lattice results for the spectral function and its exponent	77
F. Extraction of α_s	84
G. Summary	86
V. Conclusions	88
Acknowledgments	89
Appendices	
Appendix A. Tensor network representation	90
a. SUSY QM	91
Appendix B. More continuum like eigenvalue with generalized parameters	93
a. Eigenvalue on the lattice	93
1. Domain Wall height M_0	93
2. Wilson mass term r	94
3. Möbius parameter c	94
4. Pauli-Villars mass m_p	95
b. Lorentz symmetry in momentum space	95
c. Eigenvalue density	97
Appendix C. Tuned parameter sets examples	97
a. Massless $m_f = 0$	97
1. For comparison: Wilson fermion	98
2. For comparison: Shamir domain-wall fermion	99
3. $m_p \rightarrow \infty$ limit	99
4. ($M_0 = 1.4, r = 1, c = 0.3265, m_p = 1$)	100
5. ($M_0 = 0.6478, r = 0.925, c = 0.0, m_p = 2.827$)	100
6. ($M_0 = 0.405, r = 1.28, c = 0.21, m_p = 3.8$)	101
b. Massive case $m_f \neq 0$	102
1. For comparison: Wilson fermion	102

2. For comparison: Shamir domain-wall fermion	102
3. $m_f = 1, m_p = 5.06, M_0 = 0.405, r = 1.28, c = 0.21$	103
Appendix D. pole and doubler	104
a. Effective mass and doubler	105
References	108

I. INTRODUCTION

Lattice calculation plays an important role in the study of non-perturbative aspects of quantum field theory. The theoretical calculations based on perturbative expansions are widely known as the great success of recent particle physics, such as short-distance current-current correlators [1, 2]. Since the contribution from the perturbative scale dominates these quantities, an analytical perturbative expansion can produce a reliable result which is comparable to experimental results. This is a way to reveal the physics. However, perturbative expansion cannot take into account the non-perturbative contribution which must be included to reproduce the experimental results. The hadron mass spectrum is one of the most simple and excellent examples of physics from the contribution. Long-distance correlators from lattice calculations precisely predict mass spectra which are consistent with the experiment [3, 4]. In order to understand particle physics, we need to recognize perturbation theories, lattice simulations, and experiments can complement each other. Perturbative expansions of the Standard Model or its effective model with lattice calculation provides a theoretical prediction with the non-perturbative contribution. The studies of the unitary triangle and branching ratio of decays are examples of the complementarity [5].

We focus on the complementarity between perturbative expansions and lattice calculations. In contrast to the long-distance contribution which determines the hadron mass spectrum, the perturbation theory mainly describes the short-distance contribution. Since the temporal moment is a quantity which is dominated by the short-distance contributions, the perturbative expansion can represent the moment with high precision [1, 2]. In perturbation theory, the temporal moment was calculated up to the $O(\alpha_s^3)$ order. On the other hand, since the recent progress of the lattice calculation allows us to reach this high-momentum region, corresponding quantities are now calculable on the lattice [6–9]. Consequently, fundamental parameters in the perturbative expansion, such as the charm quark mass m_c and strong coupling constant α_s , are determined with little theoretical uncertainty. For instance, the charm quark mass is determined with 1 % error.

The temporal moments or derivatives of vacuum polarization function was initially introduced in the continuum theory for the analysis of experimental data [10–13], and was later applied to the lattice calculation by the HPQCD collaborations [6–8]. We use the same method to extract the charm quark mass and the strong coupling constant from an indepen-

dent set of lattice configurations generated with a fermion formulation, that is different from those used by HPQCD, at smaller lattice spacings $a \simeq 0.080, 0.055,$ and 0.044 fm [9]. We study not only pseudo-scalar current correlators, but also vector current correlators which can be directly compared to experimental results. We confirmed that our lattice results are consistent with the experimental data. It supports the reliability of the temporal moment method. We also discuss and generalize the estimation of the systematic error due to the perturbative expansion. The result achieves 1 % precision with a conservative error estimate.

We also investigate the Dirac spectral density to perform another precision test of perturbation theory [14]. Dirac eigenmodes form a fundamental building block of quantum field theory such as Quantum ChromoDynamics (QCD) and reflect the dynamics of QCD. A well-known example is a relation between near-zero eigenvalue density and chiral condensate $\langle \bar{\psi}\psi \rangle$. The near-zero eigenvalue density is a quantity for which lattice calculations provide precise non-perturbative calculations. In the previous works by the JLQCD collaboration, the Ginsparg-Wilson fermion is employed to respect chiral symmetry on the lattice since the chiral condensate is the order parameter of the chiral symmetry breaking and is very sensitive to any violation of chiral symmetry on the lattice [15]. A precise determination of the chiral condensate $\langle \bar{\psi}\psi \rangle$ was achieved by the stochastic method to count the number of eigenvalues on the lattice [16]. In this thesis, we are interested in the region of higher eigenvalues, where perturbation theory is applicable. We introduce the perturbative calculation which is known to $O(\alpha_s^4)$ order to test the perturbative expansion [17, 18].

Since we utilize the eigenvalue density in the high momentum region, the analysis may severely suffer from the discretization effect. In order to solve this problem, we introduce a modified domain-wall fermion action by generalizing the Pauli-Villars mass degrees of freedom in the formulation of the domain-wall fermion. Because the Pauli-Villars mass determines the Dirac eigenvalue cutoff scale of domain-wall fermions, the systematic error may be reduced. After taking the continuum limit with this generalized domain-wall fermion, we compare numerical results obtained on the lattice with perturbative calculation.

We use the Hybrid Monte-Carlo method to generate gauge field configurations based on the path-integral formulation. Physical observables are statistically estimated utilizing generated configurations, and the numerical lattice QCD calculation has a great success to understand QCD. In that sense, our works with temporal moments and the Dirac spectral density are also the series of the numerical efforts.

In the appendix, we additionally discuss another numerical way to calculate physical quantities on the quantum field theory which is based on the path integral formulation. Recently, the tensor network representation is revalued as an alternative representation [19–22]. This representation overcomes a part of an inefficient sampling problem such as the sign problem and provides a more efficient process for studying one and two-dimensional systems. There are many related works for one or two-dimensional fermionic system [21, 23–30], four-dimensional finite chemical potential scalar theory [31], and four-dimensional QCD [20]. This topic is also studied in the context of the condensed matter physics and quantum simulations since they are also interested in the discrete system such as spin systems [19]. Although this method is still not applicable for four-dimensional QCD numerical calculations so far, we are interested in the dual representation since it provides a different description of the quantum field theory.

The rest of this thesis is organized as follows. In section II we introduce the generalized Pauli-Villars mass with a brief review of fermion formulations. After this introduction, we consider the time moment to extract charm quark mass and strong coupling constant precisely in section III. Section IV shows the lattice calculation of Dirac spectral density and its consistency with the perturbation series. We mention that the tensor representation of lattice theory based on the path-integral formulation in the appendix. The conclusion and discussion are given in section V.

II. LATTICE QCD AND FERMION FORMULATIONS

Since the lattice discretization violates chiral symmetry, the formulation of fermions on the lattice is a non-trivial problem. In this section, we first briefly review various fermion formulations on the lattice. If one naively discretize the fermionic action, unwanted particles, which are the so-called doubling particles or simply doublers, show up. Wilson already considered this problem in his seminal paper that proposed lattice gauge theory, and he constructed a fermion formulation (Wilson fermion) without the doubler [32, 33]. The problem is studied as the well-known Nielsen-Ninomiya No-go theorem relates to the chiral symmetry [34–36]. In this section, we introduce many kinds of fermion formulations with how the method escape from Nielsen-Ninomiya No-go theorem. We also mention this problem relates the definition of the momentum on the lattice.

After twenty years since Wilson first introduced the lattice fermion formulation, the domain-wall fermion was introduced as a fermion formulation that respects the chiral symmetry on the lattice [37–39]. The domain-wall fermion is a fermion formulation with the Ginsparg-Wilson relation [40]. We introduce a variety of domain-wall fermions more precisely, including the Möbius domain-wall fermion which is used in our works [41].

In addition to the context of the field theory, we comment on the relation between the fermion formulation in high-energy physics and the condensed matter physics. Some fermion formulations such as the domain-wall fermion and the minimal doubling fermion are also studied in the context of the condensed matter physics, and some formulations are initially developed in this area [42–44]. The domain-wall fermion (as a topological insulator) and the minimal doubling fermion (as graphene with the Dirac cone) are good examples. Since the lattice quantum field theory and the condensed matter physics include the system which is described by the same action, the study in other field helps us to understand the system from a different point of view.

We explicitly write down the Dirac operator of the domain-wall fermion with parameters in order to study the dependence on these parameters. In particular, we consider the dependence on the Pauli-Villars mass for the modification of the higher momentum region. Since the Pauli-Villars mass is the cut-off scale of the Dirac eigenvalue, it modifies the approximation of large eigenvalues. This modification for the calculation of Dirac spectral density eliminates discretization effects.

A. Fermion formulations on the lattice

Although the lattice regularization respects the gauge symmetry [45], the lattice discretization breaks important symmetries, such as the Lorentz symmetry and the chiral symmetry. The Lorentz symmetry and the Leibniz rule are the most straightforward and essential example of the violation from the space-time discretization. Since fermion field variables themselves are only defined on the discretized space-time, any continuous symmetry cannot be respected on the lattice.

These are also understandable in the momentum space corresponding to the lattice space-time since the momentum has to be a discrete value depending on a cut-off corresponding to the lattice spacing a . Usually the Fourier transformation defines the momentum space, and then the momentum should be defined as $ap = \frac{\pi}{L}$ with an integer $n \in \mathbb{Z}$, $-L < n \leq L$. In this context, the discreteness of the momentum causes the violation of the Lorentz symmetry. The Leibniz rule is also inevitably violated by the finiteness of the Brillouin zone at least in the UV momentum region ($ap \simeq 1$) as $ap_{12} \neq ap_1 + ap_2$ when the $ap_1 + ap_2 > \pi$. We define the Leibniz rule in the momentum space as $ap_{12} = ap_1 + ap_2$ from $\nabla(\phi_1\phi_2) = (\nabla\phi_1)\phi_2 + \phi_1(\nabla\phi_2)$.

We should respect the locality of field theory when we construct an action since we are usually interested in field theories with locality. The simplest case is a class of actions which contains the nearest-neighbor hopping terms of ψ_x , *i.e.* $\bar{\psi}_x\psi_{x\pm a}$ and the mass term $\bar{\psi}_x\psi_x$. This structure puts a particular constraint in the momentum space. Any function of momentum has to be a combination of 1, $\sin ap$, and $\cos ap$ with some coefficients. Consequently, the approximation of action in the IR momentum region ($ap \simeq 0$) on the lattice is also violated at least $O(a^2)$ when the nearest-neighbor hopping terms construct the action. This violation can be modified as we take into account next nearest neighbor or even longer (distance na) hoppings which are represented as $\sin anp$ and $\cos anp$ with an integer $n \in \mathbb{N}$ in the momentum space.

For example, we consider a symmetric difference operator ∇_x^S as an approximation of the differential ∂_x of free fermion theory,

$$\nabla_x^S\psi(x) \equiv \frac{\psi(x+a) - \psi(x-a)}{2a} = \sinh a\partial_x\psi(x). \quad (\text{II.1})$$

Then the symmetric difference ∇_x^S becomes $i\sin ap$ after taking the Fourier transformation $\psi(x+a) = \int dp\tilde{\psi}(p)e^{ip(x+a)}$. For the lattice Dirac operator, we need to approximate the

continuum action

$$\lim_{a \rightarrow 0} aD(p) = iap + O(a^n). \quad (\text{II.2})$$

where n is an integer $n \geq 2$. Of course the $\sin ap$ provides an approximation which is written in (II.2).

In this case, we can write down an iterative approximation by using the inverse function,

$$ap = \text{Arcsin}(\sin ap) = \sin ap + \frac{(\sin ap)^3}{6} + \frac{3(\sin ap)^5}{40} + \dots, \quad (\text{II.3})$$

in the momentum region $ap \leq \frac{\pi}{2}$. Because this approximation is an infinite order series of ∇^S , the corresponding difference operator ∇ is non-local¹. We note that even if the violation in the IR region is modified, the finiteness of the Brillouin zone causes a violation in the UV region. Moreover, this modification is valid at least at the classical level.

We should also consider the unwanted poles which are originated from the periodicity. Let us consider the most naive approximation $\nabla^S(ap) = i\sin ap$ as an example. The corresponding correlator is nothing but the inverse $(\nabla^S)^{-1} \propto \sin ap^{-1}$. This correlator has a pole at $ap = 0$, as in the continuum correlator, but there is another pole at $ap = \pi$. Since the pole must be identified as a physical degree of freedom, this pole should be considered as another particle in the system. This additional particle is the so-called doubler, which has to care to identify the lattice calculation coincides with the continuum theory. Some formulations such as the Staggered fermion and the minimal doubling fermion [46–51], recognize this doubler as a physical particle in the continuum theory, and other formulations eliminate this particle in the continuum limit by giving a mass of the cut-off scale to the doubler, like as the Wilson fermion, domain-wall fermion, and Brillouin fermion [52].

From now on we will discuss the fermion formulation corresponding to the Nielsen-Ninomiya no-go theorem [34–36]. The conflict between the number of fermion species and the chiral symmetry is essential. This situation is general and can be concisely summarized by the theorem. This theorem can be stated as follows.

No fermion on even dimension can satisfy all properties on the lattice:

- (1): No doubler.
- (2): Chirality, $\{D, \gamma_\mu\} = 0$.
- (3): Locality.
- (4): Hermiticity.

¹ The non-locality appears in the function $\text{Arcsin}(\sin ap)$ as the non-differentiable point $ap = \frac{\pi}{2}$.

In the following, we discuss the properties of various possible lattice fermion formulations.

1. Non-local action

Locality is required to guarantee the causality and renormalizability in relativistic quantum field theories and therefore is satisfied in most lattice formulations. The non-local action may, however, be useful to construct a theory for which other properties are more important than the locality. A typical example is a supersymmetric system. Supersymmetry is violated when the Leibniz rule is not satisfied. As we explained, the Leibniz rule is broken with the local hopping operators. Non-local action may improve the situation in the IR region, for example, one may introduce an operator $\nabla = \text{Arcsin}(\sin ap)$. This operator is exactly the same as the continuum theory in the IR region, *i.e.* $|ap| < \frac{\pi}{2}$.

This function has another pole at $ap = \pi$, which represents a doubler, since the function $\text{Arcsin}(\sin ap)$ can be expanded by the $\sin ap$. A well-known example of the non-local difference operator without doubler is the SLAC derivative ∇^{SLAC} , which is written as

$$\nabla_{nn'}^{\text{SLAC}} = (-1)^{n-n'} \frac{\pi/L}{\sin\pi(n-n')/L}, \quad (\text{II.4})$$

which is defined in space-time. The SLAC derivative is the same as the continuum theory for the lattice momentum within the Brillouin zone $-\pi < ap \leq \pi$. Then the derivative is represented as $\nabla^{\text{SLAC}} = iap$ in the momentum space. Non-locality can be seen as a discontinuity of the function at $ap = \pi$. Since the SLAC derivative does not suffer from doubling particles, fermions described by this derivative has sometimes been used to study supersymmetric systems [53, 54]².

Non-local actions have been studied in the context of supersymmetric theories. The Kato-Sakamoto-So no-go theorem and related works, in particular, established the relation between the locality and supersymmetry on the lattice [55, 56]. The statement is that the Leibniz rule is respected if and only if the difference operator and its product are non-local. Their works well describe the Leibniz rule violation in IR and UV. The non-locality of the difference operator eliminates the IR violation, and the non-local products such as the convolution can improve the UV part.

² Since the SLAC derivative corresponds to the momentum cut-off of the continuum theory, the formulation violates gauge invariance when we introduce the gauge field.

We also show the action which is constructed by the non-local difference and product, with the different definition of the momentum [57]. They introduced the non-local difference operator using the Gudermanian function,

$$\nabla^{\text{gd}} = \frac{1}{2} \log \frac{1 + \sin ap}{1 - \sin ap}. \quad (\text{II.5})$$

This formulation respects the additivity, momentum conservation law, associativity, and the Leibniz rule, although this model is no longer the lattice formulation since the lattice spacing does not regularize the theory. For this formulation, since they do not define the momentum on the lattice by using the Fourier transformation, the lattice spacings are no more the energy scale of the cutoff.

Although the non-local fermions are theoretically interesting, we should be careful about the problem caused by the non-locality in quantum field theory. When we study locally interacting theory, these formulations confront a severe difficulty, such as the oscillatory behavior of correlators [56, 58]. In the condensed matter physics, the non-local system may also be interesting as we may consider non-local interactions.

For the non-local theory on the lattice, it is hard to confirm the locality in the continuum limit. The staggered fermion with $(N_f \bmod 4) \neq 0$ has this problem. This formulation cannot be proven to be local since the fourth root of the fermion determinant has to be taken. Even though there is no apparent pathological behavior in QCD simulations, it may introduce uncontrollable systematic errors. Domain-wall fermion has an exponential locality even though this formulation contains the root. We will discuss the details of the locality of the domain-wall fermions in the following sections.

2. *Non-hermitian action*

The non-hermitian actions have not been studied well in the last thirty years [59–62]. The reason is that the hermiticity is one of the essential properties of the quantum field theory. The action without hermiticity might be considered in the context of the condensed matter physics for non-equilibrium system [63].

3. Doubler identified action

One way to get rid of the “doubler problem” is to identify doublers as physical particles of different flavors. A well-known example is the KS (Kogut-Suskind) or the staggered fermion [46]. This fermion formulation has been widely used in the frontier of numerical lattice QCD calculations. Since the staggered fermion has a long history including the development of improved actions such as HISQ (Highly Improved Staggered Quark) [64] or ASQTAD (A Squared TADpole improved staggered quark) [65, 66], the lattice discretization error is well understood. Another advantage is the efficiency of numerical calculation. The staggered quark action needs less numerical cost compared to other popular formulations, *i.e.* about $O(10)$ times faster than the Wilson fermion, and $O(10) \sim O(100)$ times or even faster than the domain-wall or overlap fermion. Although there are some advantages to staggered quarks, there are also well-known severe disadvantages. One of the disadvantages is the non-locality originated from the fourth-root trick as we mentioned in the section of the non-local action, and the other is a partial violation of the chiral symmetry. We will explain the details.

The staggered Dirac operator is written without the gamma matrix γ_μ ,

$$aD^{KS}(x) = i\eta_\mu(x)\nabla_\mu^S + am. \quad (\text{II.6})$$

The lack of γ_μ is a characteristic property of the staggered fermion, and the sign factor $\eta_\mu(x) \equiv (-1)^{x_1+\dots+x_{\mu-1}}$ is introduced. Using this operator, we can define four flavor Dirac fields,

$$aD^{KS}(p) = (\gamma_\mu \otimes \mathbf{1})\text{sin}ap_\mu + \sum_\mu (\gamma_5 \otimes \gamma_\mu^T \gamma_5^T)(\mathbf{1} - \text{cos}ap_\mu) + (\mathbf{1} \otimes \mathbf{1})am. \quad (\text{II.7})$$

The indices of tensor products run over spinor and flavors. As we can see in the second term, a part of the chiral symmetry is explicitly broken because γ_5 commutes with itself. This term also violates the flavor symmetry as it involves a non-trivial matrix in the flavor space. Although this second term is $O(a^2)$, how the artifact affects the results is non-trivial. The number of flavors depends on the number of dimensions d , and the action represents $2^{\lfloor d/2 \rfloor}$ flavors of Dirac fermions. This relation might be quite natural since the Dirac operator only uses the sign factor $\eta_\mu(x)$ in (II.6) without the gamma matrix γ_μ . Namely, the absence of the gamma matrix leads to a slightly different chiral symmetry defined by the sign factor, and it corresponds to a part of the usual chiral symmetry.

The locality is also broken when we simulate N_f -flavor fermion, $N_f(\text{mod}4 \neq 0)$ since we usually apply the fourth-root trick $\det D_{\text{flavor}}^{KS} \equiv (\det D^{KS})^{1/4}$. The fourth root of an operator may only be defined as an infinite series of it, and it generates the non-locality. This non-locality is not well studied, and although it does not seem to have significant effects on some observables, it can affect the physical quantities in some unknown way.

We mention that the staggered fermion is used in the condensed matter physics since it does not need the gamma matrices γ_μ . For example, systems with a fermionic degree of freedom with the Dirac cone are described by the staggered fermion [67–69].

The minimal doubling fermion is another formulation which has a long history and has revisited in the context of the research of graphene a decade ago [47–51]. This formulation was first introduced in the '80s by Karsten and Wilczek [47, 48]. Its Dirac operator is represented by

$$aD^{KW}(p) = i\gamma_\mu \sin ap_\mu + am + \sum_i \gamma'_i (\mathbf{1} - \cos ap_i), \quad (\text{II.8})$$

with a twisted gamma matrix $\gamma'_i \equiv \gamma_\mu$ with $i \neq \mu$. This action only contains $\sin ap$, $\cos ap$, and 1. It means that the action has only nearest-neighbor hopping terms. The chirality is also respected since the additional term is proportional to γ_μ . The interesting point is that this action reduces the number of doublers. For simplicity, we demonstrate the reduction of doubler in two-dimensional space-time in Figure 1. The number of intersection points corresponds to the number of poles. The naive fermion has four poles, while Karsten-Wilczek fermion has only two intersection points. After this reduction, we should identify all of these poles with particles in the real world as in the staggered fermion formulation.

In the '00s, this type of action was revisited by Borici and Creutz and summarized as the minimal doubling fermion. First, the fermion formulation of graphene is written down on the honeycomb lattice, and it is projected to the usual regular grid lattice system. The most general form of the minimal doubling fermion is written as

$$aD^{Mini}(p) = i\gamma_\mu \sin(ap_\mu + \beta_\mu) + am + \sum_i A_{\mu\nu} \gamma_\nu (\cos ap_\mu - \beta_\mu) - i\Gamma. \quad (\text{II.9})$$

Here, the matrix A is an orthogonal matrix. The matrix A has at least one eigenvalue, which equals 1, and all four components of each eigenvector are non-zero. We parametrize an eigenvector of A as $\sin 2\beta_\mu$, and define the matrix Γ as $\Gamma = \sum_\mu \gamma_\mu \sin 2\beta_\mu = \sum_\mu \gamma'_\mu \sin 2\beta_\mu$.

The minimal doubling fermion can reduce the number of the intersection to two; the degeneracy of flavor is two. On the contrary to the staggered fermion, chirality is respected.

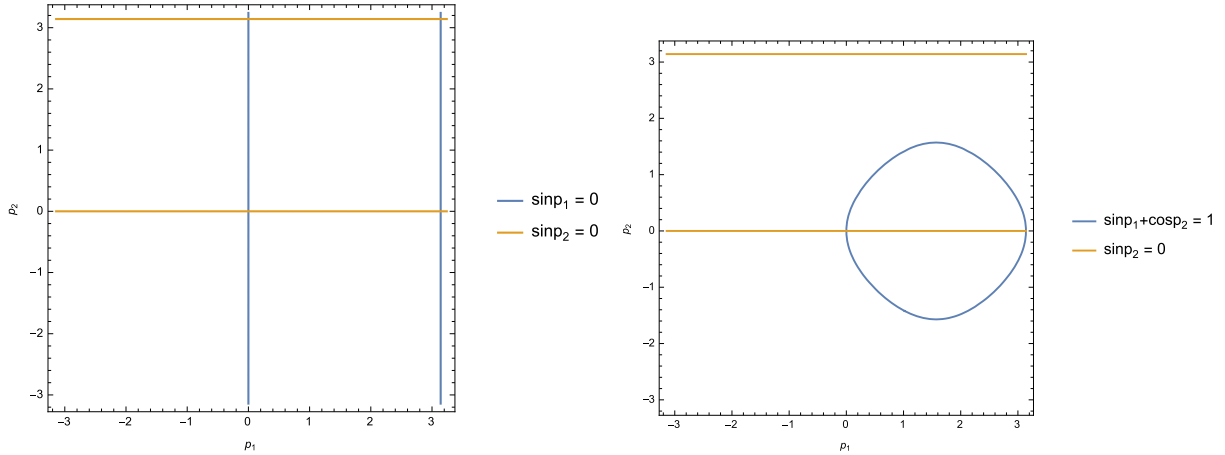


FIG. 1. The number of doublers is reduced from the naive fermion (left) to the minimal doubling fermion (right). Intersections correspond to the pole.

However, the minimal doubling fermion is not so popular since the fermion violates several discrete symmetries such as charge conjugation. For example, an oscillational behavior of correlators and contamination from the states with the same quantum number are problems for this formulation [70]. Therefore, despite the low computational cost, we need to carefully treat the source of systematic errors in order to achieve reliable results.

The minimal doubling fermion is also studied as the condensed matter physics. This fermion is known as the Kane-Mele-Hubbard model or the honeycomb lattice graphene with the Dirac cone [44]. The Kane-Mele-Hubbard model is nothing but an example of the topological insulator, and this type of actions has been well studied.

4. Chiral symmetry broken action

The simplest formulation is the fermion without exact chiral symmetry. We consider the nearest-neighbor operators $\{1, \sin ap_\mu, \cos ap_\mu\}$. As we already saw before, $\gamma_\mu \sin ap_\mu$ has exact chirality since it (anti-)commutes with gamma matrix γ_5 . Namely, the term without the gamma matrix γ_μ breaks the chiral symmetry. The simplest candidate of $O(a^2)$ term is $1 - \cos ap$, then Wilson proposed the action with a constant r as a free parameter [32, 33]:

$$aD^W(p) = i\gamma_\mu \sin ap_\mu + am + \frac{r}{2} \sum_{\mu} (1 - \cos ap_\mu). \quad (\text{II.10})$$

This action is also simply represented in coordinate space,

$$aD^W = \gamma_\mu \nabla_\mu^S + am - r\nabla_\mu^2. \quad (\text{II.11})$$

The Wilson term $r\nabla_\mu^2$ explicitly breaks the chiral symmetry. Although this term is of $O(a^2)$, the violation is a source of systematic error depending on physical quantities of interest.

This term decouples the doubler in the continuum limit. We can confirm the decoupling by considering the pole of the corresponding correlator. It appears as a solution of the equation $\sin ap_\mu^2 + (am - r/2 \sum (\mathbf{1} - \cos ap_\mu))^2 = 0$. Then the Wilson term acts as a momentum dependent mass term. Since the pole at $ap_\mu = \pi$ generates the doubler, this particle has a $O(1)$ dimensionless mass $\propto r^2$ while the physical pole has the $O(a)$ mass am . After taking the continuum limit, the doubler does not have a contribution to the physics due to decoupling.

Another way to understand the formulation comes from the periodicity of the operator. We can deform the second term as $1 - \cos ap_\mu = 2(\sin \frac{ap_\mu}{2})^2$, which has a 4π periodicity. This period is twice larger than the $\sin ap_\mu$ which is the period of 2π . Since the Brillouin zone is $-\pi < ap \leq \pi$, the longer periodic term lifts the Dirac spectrum at higher momentum.

Since Wilson fermion has a long history, its improvement has been well studied. A particularly useful improvement is Symanzik $O(a)$ improvement, which eliminates $O(a)$ artificial contribution at non-perturbative level. This improvement is based on the effective field theory of Wilson fermion at small a including possible composite operators allowed by the symmetries on the lattice. Then we add two terms to eliminate $O(a)$ artificial contribution with tuned parameters. Lattice simulations should determine the parameters since we must make the improvement non-perturbatively. We note that the improvement is not the same as the classical improvement of the action. Namely, it does not involve the higher dimensional operators as one construct $\text{Arcsin}(\sin ap)$ to eliminate $O(a^n)$ contributions in the classical action. The Symanzik $O(a)$ improved action is represented as

$$aD^{\text{Sym}} = aD^W + a^2 c_{sw} \frac{i}{4} \sigma_{\mu\nu} F_{\mu\nu}, \quad (\text{II.12})$$

with the parameter c_{sw} which is introduced by Sheikholeslami and Wohlert [71]. Here, $F_{\mu\nu}$ is the standard discretized field strength tensor, and $\sigma_{\mu\nu} = \frac{i}{2}[\gamma_\mu, \gamma_\nu]$.

Another method of the improvement, which is called the twisted mass fermion, is also often used [72–74]. The twisted mass fermion is introduced as

$$aD^{TM} = aD^W + i\mu\tau_3\gamma_5 \quad (\text{II.13})$$

with the twisted mass μ and Pauli-matrix τ_3 acting on flavor index. We tune the mass parameters am and $a\mu$ to eliminate the $O(a)$ contribution. The drawback of the twisted mass fermion is the $O(a^2)$ isospin breaking and limitation to $N_f = 2$ from the twisted mass term. Although we do not discuss the general operators, these limitations are the source of systematic uncertainty.

Finally, we also consider the Brillouin fermion, which is one of the improved Wilson fermion [52]. Let us compare the direction dependence of the Dirac operator at a momentum ap_μ and the lattice $\sin ap_\mu$. Namely, we compare the momentum ap_μ with the condition $|ap_\mu| = ap$; e.g., $ap_\mu = (2, 0, 0, 0)$ and $(1, 1, 1, 1)$ in four dimensions. It never changes the physics in the continuum. However, there is a different artificial contribution on the lattice since the $\sin ap_\mu$ is anisotropic. The discretized space-time is an origin of the Lorentz symmetry violation including the anisotropy. In order to eliminate the artifact, we often consider the artificial contribution from this anisotropic feature of the formulation and measurements. The Brillouin fermion improves the anisotropy of the action.

Since the complete expression is a bit lengthy, we write down its essence. The Brillouin fermion introduces a series of differences with constant c such as $\nabla_1^{Bri} \equiv i\sin ap_1(\cos ap_2 + c)(\cos ap_3 + c)(\cos ap_4 + c)/(c+1)^3$ as an approximation of the differential. The approximation for Laplacian ∇_μ^2 is also introduced using the combination of $\sin ap_\mu$ and $\cos ap_\mu$. We use these approximations to define more continuum like isotropic difference ∇_μ on the lattice. At least at the classical level, this kind of approximation can be used iteratively which is similar to the iterative approximation of difference, $\text{Arcsin}(\sin ap)$. Namely, we can improve approximation by using longer hopping terms. In this sense, the Brillouin fermion is a simple way to realize better approximation of the action.

The iterative approximation to reduce the anisotropy also improves the chirality on the lattice, which is known as the Ginsparg-Wilson relation. We can also approximately satisfy the Ginsparg-Wilson relation by using the series of difference, and then the Brillouin fermion has approximated the Ginsparg-Wilson chirality. The details of the relation are given below.

5. Ginsparg-Wilson fermion

The Ginsparg-Wilson relation was first introduced as a condition for the chirality on the lattice by Ginsparg and Wilson [40]. They considered a block spin transformation as a renormalization group transformation. Since the renormalization group transformation does not change physics, the action should be invariant and has the chiral symmetry. Following the discussion in their paper [40], Ginsparg-Wilson relation for Dirac operator D is represented as an $O(a)$ violation of chiral symmetry,

$$\{D, \gamma_5\} = RaD\gamma_5D, \quad (\text{II.14})$$

with some matrix or constant R .

This relation leads to an approximated chiral symmetry on the lattice. Namely, the Dirac fermion which satisfies this relation is invariant under the modified chiral transformation,

$$\delta\psi = \gamma_5(1 - aRZD)\psi, \quad \delta\bar{\psi} = \bar{\psi}(1 - aDR(1 - Z))\gamma_5, \quad (\text{II.15})$$

with a constant Z . This $O(a)$ modified chiral symmetry is often represented by using modified gamma matrix $\hat{\gamma}_5 \equiv \gamma_5(1 - RZaD)$, like $\delta\psi = \hat{\gamma}_5\psi$. Usually, we choose $Z = 1$ for $\hat{\gamma}_5^2 = 1$. Now we can explicitly understand the modified symmetry as $U_R(N) \times U_L(N)$ by $\hat{\gamma}_5$. The domain-wall fermion has the explicit form of symmetry, and it is an essential difference from other chiral breaking action such as Wilson fermion. The relation (II.14) can be also represented as the anti-comutation relation, $\gamma_5D + D\hat{\gamma}_5 = 0$.

In addition to the explicit representation of the modified chiral symmetry on the lattice, this relation is related to the $U(1)$ anomaly since the $U(N_f)$ chiral transformation contains $\hat{\gamma}_5$. Since $\hat{\gamma}_5$ contains the Dirac operator D , the functional measurement of the path integral is not invariant. It generates anomaly.

The overlap fermion and domain-wall fermion are implementations of the Ginsparg-Wilson relation. We will discuss these actions in the next section. We also show the fixed point fermion, which is sometimes called the complete fermion.

B. Overlap and Domain wall fermion

In this subsection, we introduce the overlap [75] and domain-wall fermion [38] as the fermion formulation with chirality on the lattice through the Ginsparg-Wilson relation. The

general form of the action respecting the Ginsparg-Wilson relation is

$$aD^{GW} = \frac{1}{R}(1 + am_f + (1 - am_f)V), \quad (\text{II.16})$$

which is constructed from the operator V with the condition $V^\dagger V = 1$ and $\gamma_5 V \gamma_5 = V^\dagger$ and a fermion mass m_f . At $m_f = 0$, the Ginsparg-Wilson relation is satisfied.

The overlap fermion can be simply written by the sign function with any kind of the Dirac operator on the lattice D^{Lattice} ,

$$aD^{OV} = \frac{1}{R}(1 + am_f + (1 - am_f)\gamma_5 \text{sign}(\gamma_5 D^{\text{Lattice}})). \quad (\text{II.17})$$

We identify $V \equiv \gamma_5 \text{sign}(\gamma_5 D) = \frac{D}{\sqrt{D^\dagger D}}$. One might think this example of the formulation is non-local since the infinite series of D defines operator V . However, this action is still local at the continuum limit even if all lattice points interact with each other. The exponential locality of the overlap fermion is proved by considering the taxi-driver length with the Legendre expansion [76]. To respect the locality, we need the admissibility condition³ for gauge field, which is written using the plaquette $U_{\mu\nu}$ and a small parameter ϵ as

$$\|1 - U_{\mu\nu}\| < \epsilon. \quad (\text{II.18})$$

This condition represents the continuity of gauge fields on the lattice. The admissibility condition is also required to define the topological charge on the lattice.

Although the overlap formulation has the locality in the continuum limit, the numerical cost is large since the formulation does not have nearest-neighbor locality. To calculate the fermionic part of the Boltzmann weight in the Hybrid Monte-Carlo simulation, we have to solve the inverse problem of the Dirac operator D^{Lattice} many times. For a $N \times N$ Dirac operator⁴, the cost is $O(N^3)$ to solve the eigenvalue problem. This is an additional cost compared with other formulations.

How can we reduce the numerical cost? Since the origin of the enormous cost comes from the sign function, one might consider approximating this part by a more efficient form. The domain-wall fermion is a formulation with an approximated sign function. In other words, the domain-wall fermion provides an approximation of the overlap fermion. Namely, we can

³ Since the admissibility condition is the hard condition in the actual numerical calculation, we sometimes pay attention to the locality in each simulation.

⁴ Typically, N is larger than $O(10^7)$ considering the number of lattice points, spinor, flavor and color degree of freedom.

formally introduce the domain-wall fermion by rewriting the sign function $\text{sign}(aD)$ by an approximated one, $\text{sign}_{L_s}(aD)$ with some parameter L_s .

Surprisingly, one can construct an approximation of the sign function using an extra dimension (or many flavors) with a negative mass term. Kaplan first introduced the idea to formulate chiral gauge theory, and it was utilized to define chiral Dirac fermions by Shamir [37, 38]. For simplicity, we first explain the Shamir-type domain-wall fermion.

Let us consider the free field theory $U_{\mu\nu} = 1$ to show chiral zero modes, which are localized in the surface of the fifth direction. We consider a five-dimensional Wilson fermion without gauge interaction in the fifth direction. Since we use γ_5 as the gamma matrix for the fifth direction, we can represent the fermion using the projection operators $P_{\pm} \equiv \frac{1 \pm \gamma_5}{2}$,

$$S_{\text{free}}^{DW} = \sum_{s,t} \int \frac{d^4 p}{(2\pi)^4} \bar{\psi}_s(-p) [i\gamma_{\mu} \sin p_{\mu} a + (MP_- + M^{\dagger}P_+)]_{st} \psi_t(p), \quad (\text{II.19})$$

with a mass term M and M^{\dagger} , which is a matrix in five dimensions,

$$\{(MP_- + M^{\dagger}P_+)\psi\}_s \equiv (1 - \nabla^2 - M_0)\psi_s - P_- \psi_{s+1} - P_+ \psi_{s-1}. \quad (\text{II.20})$$

The parameter M_0 represents a negative mass of the Wilson fermion in the five dimension, and often called as the domain-wall height.

When the mass matrix has zero eigenvalues, the chiral zero modes exist in theory. The zero eigenvalues are the solution of corresponding linear equations $M\mathbf{u}_L = 0$ and $M^{\dagger}\mathbf{u}_R = 0$ with Dirichlet boundary condition in the limit of infinite fifth dimension $L_s \rightarrow \infty$ when $|1 - \nabla^2 - M_0| < 1$. The condition $0 < M_0 < 10$ satisfies, with the different pole number. The relation is shown in table I, and we usually choose $0 < M_0 < 2$ or $M_0 = 1$ to take mild continuum extrapolation. We note that this relation is slightly changed in interacting theories, depending on the magnitude of gauge fields. The domain-wall height M_0 dependence in lattice formulation is well studied, and we sometimes choose $1 < M_0 < 2$ to reduce the artificial contribution⁵.

The solution of the linear equations $M\mathbf{u}_L = 0$ and $M^{\dagger}\mathbf{u}_R = 0$ are exponentially localized at the boundary of the fifth direction, $s = 0$ and $s = L_s$. Namely, the chiral fermion is nothing but $\psi_{s=0} = u_L$ and $\psi_{s=L_s} = u_R$ after taking the limit of infinite fifth direction,

⁵ After the smearing procedure to construct smoother gauge configuration $U_{\mu\nu} \simeq 1$, we often use $M_0 = 1$ since the relation becomes almost the same as a free fermion. Without the smearing, there are some studies to reduce the artificial contribution by choosing $1 < M_0$, for example, $M_0 = 1.8$.

p_μ	Pole number	M_0 Condition
(0,0,0,0)	1	$0 < M_0 < 2$
$(\frac{\pi}{a}, 0, 0, 0), \dots, (0, 0, 0, \frac{\pi}{a})$	4	$2 < M_0 < 4$
$(\frac{\pi}{a}, \frac{\pi}{a}, 0, 0), \dots, (0, 0, \frac{\pi}{a}, \frac{\pi}{a})$	6	$4 < M_0 < 6$
$(\frac{\pi}{a}, \frac{\pi}{a}, \frac{\pi}{a}, 0), \dots, (0, \frac{\pi}{a}, \frac{\pi}{a}, \frac{\pi}{a})$	4	$6 < M_0 < 8$
$(\frac{\pi}{a}, \frac{\pi}{a}, \frac{\pi}{a}, \frac{\pi}{a})$	1	$8 < M_0 < 10$

TABLE I. The pole number corresponds to the domain-wall height M_0 .

$L_s \rightarrow \infty$. The location also coincides with the defects of the domain-wall height M_0 since we introduced the Dirichlet condition. Domain-wall fermion uses these left-handed and right-handed chiral fermion to construct the Dirac fermion on the lattice. For more realistic fermion, we should introduce the fermion mass term as alternative boundary condition since the physical Dirac fermion are localized at the boundary.

One of the essential properties of the domain-wall fermion is the Partially Conserved Axial Current (PCAC) relation. Since this relation is proved in interacting theory, it is an evidence of zero mode existence in interacting theory. We consider an $SU(N_f)$ chiral transformation using the generator τ^a , $\psi_s \rightarrow \psi'_s = e^{i\theta_s^a \tau^a} \psi_s$ with a sign function $\theta_s^a = \theta^a \text{sign}(\frac{L_s+1}{2})$. Then we can study the corresponding Axial-Ward-Takahashi identity, with the anomalously breaking term,

$$j_5^a \equiv \bar{\psi}_{L_s/2+1} P_+ \tau^a \psi_{L_s/2} - \bar{\psi}_{L_s/2} P_- \tau^a \psi_{L_s/2+1}, \quad (\text{II.21})$$

which can be explicitly related to the gauge fields expression ($N_f > 1$),

$$\langle j_5^0 O \rangle = \langle \frac{g^2}{32\pi^2} \epsilon^{\mu\nu\alpha\beta} F_{\mu\nu} F_{\alpha\beta} O \rangle. \quad (\text{II.22})$$

Namely, the domain-wall fermion has the chirality on the lattice, even when we include the quantum effects of the theory with the gauge interaction.

However, this is strange for us if we remember the Nielsen-Ninomiya no-go theorem, *i.e.* the fermion without the doubler, with chirality and locality, must be prohibited. In fact, the naive construction of the five-dimensional lattice fermion does not work since the locality is not respected. This problem can be clearly understood when we construct the approximated overlap fermion from domain-wall fermion. We will show the relation, as a

procedure to approximate the sign function $\text{sign}(\gamma_5 D^{\text{Lattice}})$ in the overlap fermion. A key is the Pauli-Villars field.

The relation between the five-dimensional domain-wall fermion and the four-dimensional overlap fermion can be shown in two ways. One is quite simple. We can iteratively integrate out heavy (doubler and bulk) fermions in the fifth direction, and define effective action in the four-dimensional space-time. The other is represented in the context of approximation of the sign function. A systematic procedure of linear algebra, such as the LDU decomposition constructs the “projection” from the lattice five-dimensional space to physical four dimensions.

We first show the iterative integration for an instructive method. In this construction, we finally found the effective Dirac operator of quark fields after integration of $\psi_{s>0}$,

$$aD_{\text{eff}} = \frac{(1 + am_f) + (1 - am_f)\gamma_5 \tanh\left(\frac{L_s}{2} a_5 \gamma_5 D_{\text{Lattice}}\right)}{1 - \gamma_5 \tanh\left(\frac{L_s}{2} a_5 \gamma_5 D_{\text{Lattice}}\right)}. \quad (\text{II.23})$$

The inverse of this effective Dirac operator is quark propagator, $\langle q\bar{q} \rangle$, and then the operator is $aD_{\text{eff}}(m_f) = aD_{\text{eff}}(0) + m_f$. Although this is an effective Dirac operator of the domain-wall operator, this is not an overlap operator at $L_s \rightarrow \infty$ limit. To show this fact, the only thing we have to notice is that the hyperbolic tangent function $\tanh x$ is an approximated form of the sign function $\text{sign} x$. It is also known differentiable function which is called the sigmoid function in the field of numerical calculations. Anyway, we can express the tangent hyperbolic function as an approximated sign function,

$$\gamma_5 \tanh\left(\frac{L_s}{2} a_5 \gamma_5 D_{\text{Lattice}}\right) = \gamma_5 \text{sign}_{L_s}(\gamma_5 D_{\text{Lattice}}) = V, \quad (\text{II.24})$$

and then the exact chiral symmetry $\{D_{\text{eff}}, \gamma_5\} = 0$ is confirmed at $am_f = 0$ by using the γ_5 hermiticity $\gamma_5 V \gamma_5 = V^\dagger$ and unitarity $V^\dagger V = 1$.

We must violate this exact chirality to the Ginsparg-Wilson like chirality, without loss of the locality. Although the locality is not definite, we can introduce the chirality broken part to respect the Ginsparg-Wilson relation. We substitute (II.24) for (II.23), and compare it to D^{OV} of (II.17). Since the denominator of the effective operator is differ from the overlap operator, we would like to eliminate this part. The Pauli-Villars field which has different statistics with the heavy mass m_{PV} eliminates the denominator since the usual fermionic field determinant is $\det D_{\text{eff}}(m_f)$ while the Pauli-Villars field determinant is $(\det D_{PV})^{-1} = (\det D_{\text{eff}}(m_{PV}))^{-1}$. The domain-wall operator aD^{DW} , which corresponds

to the approximation of the overlap operator is now defined as a ratio,

$$\begin{aligned} aD^{DW} &= am_{PV} \frac{D_{\text{eff}}(m_f)}{D_{\text{eff}}(m_{PV})} \\ &= am_{PV} \frac{(1 + am_f) + (1 - am_f)\gamma_5 \tanh\left(\frac{L_s}{2} a_5 \gamma_5 D_{\text{Lattice}}\right)}{(1 + am_{PV}) + (1 - am_{PV})\gamma_5 \tanh\left(\frac{L_s}{2} a_5 \gamma_5 D_{\text{Lattice}}\right)}, \end{aligned} \quad (\text{II.25})$$

and then $aD^{OV}(m_f) = aD^{DW}(m_f)$ when we choose Pauli-Villars mass $am_{PV} = 1$, and $R = 2$. The Pauli-Villars field has a heavy mass since the mass is lattice cutoff order $m_p = O(a^{-1})$ and then the field violates exact chirality at $m_f = 0$ to $O(a)$ violated symmetry with satisfying the Ginsparg-Wilson relation by the mass term m_p ⁶.

The crisis at locality can be expressed as follows. We consider $m_f = 0$ with $am_{PV} = 1$ for simplicity, and then the effective operator D_{eff} can be represented by the overlap operator D^{OV} at $L_s \rightarrow \infty$,

$$aD_{\text{eff}} = \frac{aD^{OV}}{1 - aD^{OV}}. \quad (\text{II.26})$$

This form is defined by the infinite series of aD^{OV} since the overlap operator appears in the denominator. Although this is not a rigorous proof of the non-locality, it can violate the locality by this $O(a)$ contribution from the denominator.

We now briefly introduce the projection from the five-dimensional space to the physical four dimensions. Here we also introduce generalized domain-wall fermions including Möbius and Chiu fermion, not only the Shamir type fermion which is a standard and straightforward choice [41, 77].

The variations of the domain-wall fermions are formally represented as

$$\begin{aligned} aD^{GDW} &= aD_+^{(s)} \delta_{s,t} + aD_-^{(s)} [P_+ \delta_{s,t+1} + P_- \delta_{s,t-1}] \\ &\quad - (1 + am) aD_-^{(s)} [P_+ \delta_{s=1,t+1} + P_- \delta_{s=L_s,t-1}] \end{aligned} \quad (\text{II.27})$$

where operators defined by the lattice Dirac operator with kernel parameters b_5 and c_5 ,

$$aD_+^{(s)} \equiv b_5(s) aD_{\text{Lattice}} + 1, \quad (\text{II.28})$$

$$aD_-^{(s)} \equiv c_5(s) aD_{\text{Lattice}} - 1. \quad (\text{II.29})$$

The definition of parameters b_5 and c_5 defines how the projection approximates the sign function in the overlap operator.

⁶ $m_p = O(a^{-1})$ also means that the $aD(m_{PV}) = O(1)$, not $O(a)$ as usual $aD(m_f)$.

Shamir type fermion corresponds to $b_5 = 1$ and $c_5 = 0$, and also Borici type $b_5 = 1$ and $c_5 = 1$. The Möbius fermion is the generalization of these types, with any constants b_5 and c_5 . We will use the Möbius fermion for calculations of moments and Dirac eigenvalue density, with the parameter $b_5 = 2$ and $c_5 = 1$. We can consider the parameter dependence on the fifth direction for an approximation of the fermion. This fermion is the so-called optimal fermion which is introduced by Chiu. They define the approximation in the mathematical way to choose $b_5(s)$ and $c_5(s)$ depending on the fifth direction s , at finite regions.

For any domain-wall fermions, we use the projection in fifth direction \mathcal{P} ,

$$\mathcal{P}_{s,t} \equiv P_- \delta_{s,t} + P_+ \delta_{s,t-1}, \quad (\text{II.30})$$

to construct the overlap operator. The overlap operator can be constructed as

$$aD^{OV} = [\mathcal{P}^{-1}(aD_{\text{Lattice}}(m_{PV}))^{-1}(aD_{\text{Lattice}}(m_f))\mathcal{P}]_{s=1,t=1}. \quad (\text{II.31})$$

Since determinants of the left and right-hand side are the same as each other, the physics described by both operators is also the same. Here we introduce the Pauli-Villars part as the inverse, $(aD_{\text{Lattice}}(m_{PV}))^{-1}$, to approximate the overlap fermion. The approximated overlap fermion can be represented using the approximated sign function sign_{L_s} with the kernel operator D_{Ker} ,

$$aD^{OV} \equiv am_{PV} \frac{(1 + am_f) + (1 - am_f)\gamma_5 \text{sign}_{L_s} \gamma_5 aD_{Ker}}{(1 + am_{PV}) + (1 - am_{PV})\gamma_5 \text{sign}_{L_s} \gamma_5 aD_{Ker}}. \quad (\text{II.32})$$

The kernel of the sign function is defined as

$$aD_{Ker} \equiv \frac{(b_s + c_s)aD_{\text{Lattice}}}{(b_s - c_s)aD_{\text{Lattice}} + 2} \equiv \frac{baD_{\text{Lattice}}}{caD_{\text{Lattice}} + 2}. \quad (\text{II.33})$$

Here we introduce the constants b and c for simplicity. The approximated sign function is

$$\text{sign}_{L_s}(x) = \frac{(x+1)^{L_s} - (x-1)^{L_s}}{(x+1)^{L_s} + (x-1)^{L_s}} = \tanh\left(-\frac{L_s}{2} \ln\left(\frac{1-x}{1+x}\right)\right). \quad (\text{II.34})$$

Again the hyperbolic tangent function is an approximation of the sign function. Also, we can understand this function as an approximation in the context of the Newton method. We find an approximation of the sign function to apply the method to the function $f(x) = x^2 - 1$. This approximated form is sometimes called the polar decomposition.

Now we discuss what the approximation is. We can investigate the approximation in the small eigenvalue λ regions by the expansion $(1 \pm \lambda)^{L_s} = 1 \pm L_s \lambda + L_s(L_s - 1)\lambda^2/2$. Then the

approximated sign function is $\text{sign}_{L_s} x = L_s \lambda - O(\lambda^3)$. We also consider the large eigenvalue region using exact symmetry, $\text{sign}_{L_s} \lambda = \text{sign}_{L_s}(1/\lambda)$. Above of all, the polar decomposition provides the good approximation in the region $O(L_s^{-1}) < \lambda < O(L_s)$.

This deviation is, of course, a source of systematic error which can violate the Ginsparg-Wilson relation [78]. For example, we may suffer from the systematic effects when we consider the physical phenomena which are strongly related to the chiral symmetry such as the topological charge and the $U_A(1)$ symmetry. Although we usually expect that the violation is eliminated at infinite fifth direction limit $L_s \rightarrow \infty$, we should investigate the violation quantitatively.

The residual mass is an example. As we already introduced for the Ginsparg-Wilson relation as the chirality on the lattice, we can explicitly show the $U_R(N_f) \times U_L(N_f)$ chirality with the modified gamma matrix $\hat{\gamma}_5 \equiv \gamma_5(1 - RaD^{OV})$ and corresponding modified projection operators $\hat{P}_\pm \equiv \frac{1 \pm \hat{\gamma}_5}{2}$, straightforwardly⁷. This modified projection operators still have the properties, $\hat{P}_+^2 = \hat{P}_+$, $\hat{P}_-^2 = \hat{P}_-$, and $\hat{P}_+ \hat{P}_- = \hat{P}_- \hat{P}_+ = 0$. The residual mass is defined as the violation of this property,

$$\Delta_{L_s}(D_{Ker}) \equiv \hat{P}_+ \hat{P}_- = \frac{1 - \hat{\gamma}_5}{4} = \frac{1 - \text{sign}_{L_s}^2(\gamma_5 a D_{Ker})}{4}. \quad (\text{II.35})$$

Since of course the usual fermion mass term violates the chiral symmetry, this violation terms called as residual ‘‘mass’’. The violation from the mass term is $m_f \bar{\psi}(\gamma_5 + \hat{\gamma}_5)\psi \equiv 2\bar{\psi}\Delta_{m_f}\psi$, and then the total violation of the Ginsparg-Wilson relation of the domain-wall fermion is now represented as

$$\gamma_5 D^{OV} + D^{OV} \hat{\gamma}_5 = 2\bar{\psi}\Delta_{m_f}\psi + 2\gamma_5 \Delta_{L_s}(D_{Ker}). \quad (\text{II.36})$$

We need a sufficiently small residual mass for the reliable Ginsparg-Wilson like chirality on the lattice.

Here we mention that the Möbius fermion is a method to improve the approximation. The Möbius fermion use the positive constant scale $r > 0$ invariance of the sign function, $\text{sign}(rx) = \text{sign}(x)$. Since our approximated function $\text{sign}_{L_s}(x)$ has approximated range as $O(L_s^{-1}) < \lambda < O(L_s)$, we choose the (Möbius) parameters b and c to shift the eigenvalues more well approximated region. The parameter b changes the scale, and c also changes

⁷ We chose $Z = 1$ for the normalization of the modified projection operator \hat{P}_\pm .

higher a contributions in the kernel operator D_{Ker} . We can tune these parameters to get a better approximation.

As an interesting relationship with other areas, the domain-wall fermion can be understood as the topological insulator in the condensed matter physics. A simple example is (a typical choice of) two-band model in a two-dimensional system, which has the spin-orbital interaction [42–44]. Since this model has the same action with the domain-wall fermion in the classical level, the system has the same dynamics on the lattice. Condensed matter physicists can consider much more generalized action since lattice quantum field theorists have to respect Lorentz symmetry.

C. Generalized Pauli-Villars mass and discretization effects

We consider the overlap fermion with the Pauli-Villars mass $m_p \neq 1$ and general parameters such as domain-wall height M_0 and Möbius kernel parameter b and c . In this subsection, we discuss a series of systematic uncertainty from the domain-wall fermion and its parameter dependence in free field theory, $U_{\mu\nu} = 1$ with the infinite fifth direction, $L_s \rightarrow \infty$. As the most general form, we introduce the operator as

$$aD^{OV} \equiv M_0(2 - cM_0)am_p \frac{(1 + am_f) + (1 - am_f)\gamma_5 \text{sign} \gamma_5 aD_{Ker}}{(1 + am_{PV}) + (1 - am_{PV})\gamma_5 \text{sign} \gamma_5 aD_{Ker}}. \quad (\text{II.37})$$

The prefactor $M_0(2 - cM_0)am_p$ needs to realize $aD^{OV} \rightarrow iap + am_f^{\text{scaled}}$ at the continuum limit $a \rightarrow 0$. The scaled mass is defined as $am_f^{\text{scaled}} \equiv (2 - cM_0)M_0m_f$. Note that the Möbius parameter b only changes the scale of the kernel operator aD_{Ker} , to get a larger approximated range. Since we consider $L_s \rightarrow \infty$ limit for simplicity, this Möbius parameter does not contribute to the overlap operator.

Before we discuss the approximation of the operator numerically, we briefly review the previous works. The explicit representation of the quark propagators $\langle q\bar{q} \rangle$ provides the numerical study on the finite L_s with different Möbius parameters b and c . It shows that a series of massive doubling particles corresponding to each slice of fifth directions depending on parameters, especially Möbius parameters b and c . The explicit calculation provides the dispersion relation $E(\mathbf{p})$ on the finite L_s . We also discuss the dispersion relation of the overlap fermion operator aD^{OV} as the infinite $L_s \rightarrow \infty$ limit. The infinite L_s generates infinite numbers of the doubler, and then the inverse of the overlap operator has the cut on

the complex plane. This might be natural since the overlap operator has the square root in the sign function, $\gamma_5 \text{sign}(\gamma_5 D) = D/\sqrt{D^\dagger D}$.

The unphysical oscillation in correlators is also interesting in the context of the parameter dependence on the lattice [79, 80]. Although this oscillation is $O(a)$ or higher contribution which should eliminate at the continuum limit $a \rightarrow 0$, this contribution can be a source of the significant uncertainty. In particular, the artificial contribution is not so uncommon as we can see in the naive improvement of difference, the minimal doubling fermion, the staggered fermion, as examples.

The naive improvement of difference is the most simple example. We focus on the $ap \sim 0$ and the most naive action has two poles $(ap)^2 + (am)^2 = 0$. Since the improvement of difference provides higher differential contributions as $c_4(ap)^4$ with a constant c_4 , the number of poles are grown to four even if this artificial pole comes from the more higher a^n order. Depending on the action and modification, these poles often take imaginary numbers and generate the unphysical oscillational contribution for the corresponding correlators.

The decoupling condition for doubler $0 < M_0 < 2$ is also changed depending on the parameters, (r, M_0, c, m_p) . For constant term elimination ($0 < M_0 < 2$) becomes $0 < \frac{M_0}{2-cM_0}$ to get the Dirac operator $aD \rightarrow iap$. We can construct the operator without unphysical oscillation if the parameters satisfy $M_0 \leq 1$ with the Möbius parameter $c = 1$. Since we also require the no-doubler condition of the Wilson kernel, then the Wilson parameter has to satisfy the condition $M_0 < 2r$.

We can consider eigenvalues and the dispersion relation explicitly since there is no non-commutative gauge field. The hermite operators $aD_{Lattice}^\dagger aD_{Lattice}$ and $aD_{Lattice}^\dagger + aD_{Lattice}$ are explicitly written down without the gamma matrix γ_μ . For simplicity, we formally introduce the kernel operator $aD_{Lattice}$,

$$aD_{Lattice} \equiv i\gamma_\mu \sin ap_\mu + W - 1, \quad (\text{II.38})$$

with the function $W(p)$ which has no gamma matrix γ_μ . For example, $W = 1 - M_0 + r \sum (\mathbf{1} - \cos ap_\mu)$ for the Wilson fermion kernel. Using this representation, we can calculate these quantities analytically. Namely, $aD_{Lattice}^\dagger aD_{Lattice} = (\sin ap_\mu)^2 + (W - 1)^2$ and $aD_{Lattice}^\dagger + aD_{Lattice} = 2W - 2$. We also consider the hermite operators $aD_{Ker}^\dagger aD_{Ker}$ and $aD_{Ker}^\dagger + aD_{Ker}$

as the functions of $aD_{Lattice}^\dagger aD_{Lattice}$ and $aD_{Lattice}^\dagger + aD_{Lattice}$,

$$\begin{aligned} a^2 D_{Ker}^\dagger D_{Ker} &= \frac{b^2 a^2 D_{Lattice}^\dagger D_{Lattice}}{4 + 2c(aD_{Lattice}^\dagger + aD_{Lattice}) + c^2 a^2 D_{Lattice}^\dagger D_{Lattice}}, \\ aD_{Ker}^\dagger + aD_{Ker} &= \frac{2b(aD_{Lattice} + aD_{Lattice}^\dagger + ca^2 D_{Lattice}^\dagger D_{Lattice})}{4 + 2c(aD_{Lattice}^\dagger + aD_{Lattice}) + c^2 a^2 D_{Lattice}^\dagger D_{Lattice}}. \end{aligned} \quad (\text{II.39})$$

Again we also consider hermit combination of the operator $V \equiv \gamma_5 \text{sign}(\gamma_5 aD_{Ker})$, $V^\dagger V = 1$ and $V^\dagger + V$,

$$V^\dagger + V = \frac{D_{Ker}^\dagger + D_{Ker}}{\sqrt{D_{Ker}^\dagger D_{Ker}}}, \quad (\text{II.40})$$

and then finally we consider the overlap operator as the function of $V^\dagger + V$,

$$a^2 D_{OV}^\dagger D_{OV} = ((2 - cM_0)M_0 m_p)^2 \frac{2(1 + m_f^2) + (1 - m_f^2)(V^\dagger + V)}{2(1 + m_p^2) + (1 - m_p^2)(V^\dagger + V)}. \quad (\text{II.41})$$

For the discussion of the quark propagator and its pole, we also introduce another representation of the aD^{OV} using V ,

$$(2 - cM_0)M_0 m_p \frac{(2(1 + m_f m_p) + (1 - m_f m_p)(V + V^\dagger) + (m_p - m_f)(V - V^\dagger))}{2(1 + m_p^2) + (1 - m_p^2)(V + V^\dagger)}. \quad (\text{II.42})$$

The operator $V - V^\dagger$ contains the gamma matrix,

$$V - V^\dagger = \frac{4i\gamma_\mu \text{sin}ap_\mu}{\sqrt{D_{Ker}^\dagger D_{Ker}} \sqrt{(2 + caD_{Ker}^\dagger)(2 + caD_{Ker})}}. \quad (\text{II.43})$$

We will discuss the parameter dependence by using above representaitons.

These situations are still realized if we consider the mean field approximation for gauge fields, $U_{\mu\nu} = u_0$. Since the link variable is used at the difference operator ∇ , the corresponding changing is $\text{sin}ap \rightarrow u_0 \text{sin}ap$ and $\text{cos}ap \rightarrow u_0 \text{cos}ap$ in momentum space. We can redefine the parameter (M_0, b, c) to represent the mean field analysis of any u_0 , defined as $M_0^{(u_0)} \equiv \frac{1}{u_0}(M_0 - 4r(1 - u_0))$, $b^{(u_0)} \equiv u_0 b$, and $c^{(u_0)} \equiv u_0 c$. Namely, the mean field theory can identify the free field theory,

$$aD^{OV}(r, M_0, c, m_p, u_0) = aD^{OV}(r, M_0^{(u_0)}, c^{(u_0)}, m_p, u_0 = 1), \quad (\text{II.44})$$

with the corresponding domain wall height and Möbius parameters, $(M_0^{(u_0)}, b^{(u_0)}, c^{(u_0)})$. When we consider the action without smearing ($u_0 < 1$), we can understand that the parameter dependence is the gauge field u_0 contribution⁸.

⁸ Intuitively, the gauge field contribution changes the effective domain-wall height to the smaller value since the contribution lifts eigenvalues of the (Wilson) kernel operator. Then we sometime tune the bare domain-wall height to choose $M_0^{(u_0)} \simeq 1$.

We set parameters $r = 1$, $c = 1$, and $M_0 = 1$ which are our choice to describe the Pauli-Villars mass m_p dependence. The details of the parameters (r, M_0, c, m_p) dependence are discussed in Appendix. The explicit representation of this choice is already written down. For our parameters we can understand that the Pauli-Villars mass is a cut-off scale of this overlap operator, using $|\gamma_5 \text{sign}(\gamma_5 a D_{\text{Ker}})| = 1$. We substitute $\gamma_5 \text{sign}(\gamma_5 a D_{\text{Ker}}) = \pm 1$ to get the minimum and maximum of $|aD^{OV}|$,

$$am_f \leq |aD^{OV}(r = 1, M_0 = 1, c = 1, m_p)| \leq am_p. \quad (\text{II.45})$$

The Pauli-Villars mass determines the cut-off scale in the context of the eigenvalue.

On the other hand, there is no Pauli-Villars mass dependence on the pole of the correlators, *i.e.* there is no changing in the dispersion relation. It can be quite simply understandable since the denominator of $(aD^{OV})^{-1}$ only depends on m_f . Although the Pauli-Villars mass might affect doublers, the mass has the contribution to the physical pole which is only the overall coefficient, as we defined $am_f^{\text{scaled}} \equiv (2 - cM_0)M_0m_f$. Other contributions from the Pauli-Villars mass is in the loop level (eigenvalue level).

We also show the Pauli-Villars mass dependence of the chirality and locality. We can get the Ginsparg-Wilson relation as the chirality on the lattice by using $V^\dagger V = 1$ and $\gamma_5 V \gamma_5 = V^\dagger$,

$$\{(aD^{OV}(m_f = 0, m_p))^{-1}, \gamma_5\} = \frac{2a\gamma_5}{(2 - cM_0)M_0m_p}. \quad (\text{II.46})$$

This equation means that the $O(a)$ discrepancy between the lattice and the continuum depends on the Pauli-Villars mass: the chirality will be improved as the Pauli-Villars mass becomes heavy. This improvement is natural if we remember why the Pauli-Villars mass is needed. We introduce the Pauli-Villars field to realize the chirality as the Ginsparg-Wilson relation with the locality. Without Pauli-Villars fields, the operator has an exact chirality without locality. Since the infinite mass limit $m_p \rightarrow \infty$ means Pauli-Villars fields are decoupled from the theory, the theory should be non-local even if the chirality becomes exact. We will show the trade-off between the chirality and locality.

We show the similar trade-off property of the fixed-point fermion. The fermion has the Ginsparg-Wilson relation

$$\{(D^{FP})^{-1}, \gamma_5\} = \frac{2a\gamma_5}{\kappa_f}, \quad (\text{II.47})$$

with the parameter of the block spin transformation κ_f instead of m_p . When we consider the fixed point fermion, while the chirality and locality depend on κ_f .

For more detailed investigation, we prove the locality of the generalized operator. To focus on the locality crisis, we represent the operator as follows,

$$aD_{\text{OV}}(m_f = 0, m_p) = \frac{(2 - cM_0)M_0m_p}{1 - m_p} \left[1 - \frac{2m_p}{(1 + m_p) + (1 - m_p)V} \right]. \quad (\text{II.48})$$

From this representation, we clearly understand that $((1 + m_p) + (1 - m_p)V)^{-1}$ has the possibility of locality crisis. Note that the operator V is not an exact local operator. It also correlates with any point although it is exponentially localised. For the proof of locality, we expand the operator $((1 + m_p) + (1 - m_p)V)^{-1}$ by $M_R \equiv (1 - m_p)/(1 + m_p)$ when $m_p > 0$,

$$\frac{1 + m_p}{(1 + m_p) + (1 - m_p)V} = \sum_{k=0}^{\infty} (-1)^k (|M_R|V)^k. \quad (\text{II.49})$$

We use the norm properties, $|V| = 1$, $|A + B| \leq |A| + |B|$ and $|AB| \leq |A||B|$,

$$\left| \sum_{k=0}^{\infty} (-1)^k (|M_R|V)^k \right| \leq \sum_{k=0}^{\infty} (|M_R||V|)^k. \quad (\text{II.50})$$

We use $|V|^k = |V|$, and the Legendre expansion of the operator V ,

$$\left| \sum_{k=0}^{\infty} (-1)^k (|M_R|V)^k \right| \leq \sum_{k=0}^{\infty} \left(|M_R|^k |A| \kappa \sum_t e^{-\theta t} |P_t(z)| \right). \quad (\text{II.51})$$

Following the similar discussion with the normal Domain-Wall fermion locality [76], we consider the Taxi-driver length and count up the number of A and A^\dagger , we get the constraint, $t \geq \frac{|x-y|}{2}$.

Finlay we apply the property of the Legendre expansion $|P_t(z)| \leq 1$,

$$\left| \sum_{k=0}^{\infty} (-1)^k (|M_R|V)^k \right| \leq e^{-\theta \frac{|x-y|}{2}} \frac{1}{1 - |M_R|} |A| \kappa \frac{1}{1 - e^{-\theta}}. \quad (\text{II.52})$$

This expansion shows the exponential locality same as the locality before generalization.

For more about the locality, we discuss the tree level locality of the generalized domain-wall fermion and reveal the dependence of the Pauli-Villars mass. To consider its dependence, we remember the discussion of the pole of the free quark propagator. We can understand it as the locality dependence if we consider it as $m \leftrightarrow m_p$. Quark propagator $\langle q(-p)q(p) \rangle_m$ with fermion mass m is

$$\langle q(-p)q(p) \rangle_m = \frac{-i\gamma_\mu \sin p_\mu + m(1 - We^{-\alpha})}{-(1 - We^\alpha) + m^2(1 - We^{-\alpha})}, \quad (\text{II.53})$$

with Wilson term in momentum space $W(p) = 1 - M_0 + r \sum (1 - \cos ap_\mu)$, defined by the domain-wall height M_0 and Wilson parameter r [81]. We choose $M_0 = 1$ and $r = 1$, *i.e.* we use $W(p) = \sum (1 - \cos ap_\mu)$. In this parametrization, we define the parameter α by the equation,

$$\cosh(\alpha) = \frac{1 + W^2 + \sum_\mu \sin^2 p_\mu}{2W}. \quad (\text{II.54})$$

We calculate the pole of $\langle q(-p)q(p) \rangle_m$ as the locality weight in the conditions $p_0 \neq 0$ and $p_i = 0$ for simplicity. It means that if the propagator $\langle q(-p)q(p) \rangle_m$ has no cut on the Riemann surface, we get actual locality weight in this conditions. From (II.54) we get $2W \cosh \alpha = 1 + 2W$ and then we write $e^{\pm \alpha}$ as a function of W ,

$$We^{\pm \alpha} = W + \frac{1}{2} \pm \sqrt{W + \frac{1}{4}}. \quad (\text{II.55})$$

The pole of the propagator is the solution of the equation,

$$m^2 = \frac{\frac{1}{2} - W - \sqrt{W + \frac{1}{4}}}{\frac{1}{2} - W + \sqrt{W + \frac{1}{4}}}. \quad (\text{II.56})$$

The solution is represented by $Q = ((1 + m^2)/(1 - m^2))^2$,

$$W = \frac{1 + Q \pm \sqrt{3Q + Q^2}}{2}. \quad (\text{II.57})$$

If we substitute $m \in \mathbb{R}$ for Q , Q is positive definite and p_0 becomes imaginary $p_0 = im_1$ or $p_0 = im_2 + \pi$. Since Wilson term $W < 0$ for $p_0 = im_1$, the solution is written as follows,

$$m_1 = \text{Arccosh} \left(\frac{1 - Q + \sqrt{3Q + Q^2}}{2} \right). \quad (\text{II.58})$$

We also find the solution for $p_0 = im_2 + \pi$ with the condition $W > 0$,

$$m_2 = \text{Arccosh} \left(\frac{-1 + Q + \sqrt{3Q + Q^2}}{2} \right). \quad (\text{II.59})$$

These two different poles m_1 and m_2 are taken depending on the mass m . When we choose the mass $m \in \mathbb{R}$, Q is positive definite, $W \in \mathbb{R}$, $\cosh \alpha \in \mathbb{R}$, and $e^{\pm \alpha} \in \mathbb{R}$. From these conditions, there is a constraint on Wilson term, $W > -1/4$. If we substitute the mass $m^2 < 1$ for (II.56), we get the relation $|1 - We^\alpha| < |1 - We^{-\alpha}|$ and then the Wilson term

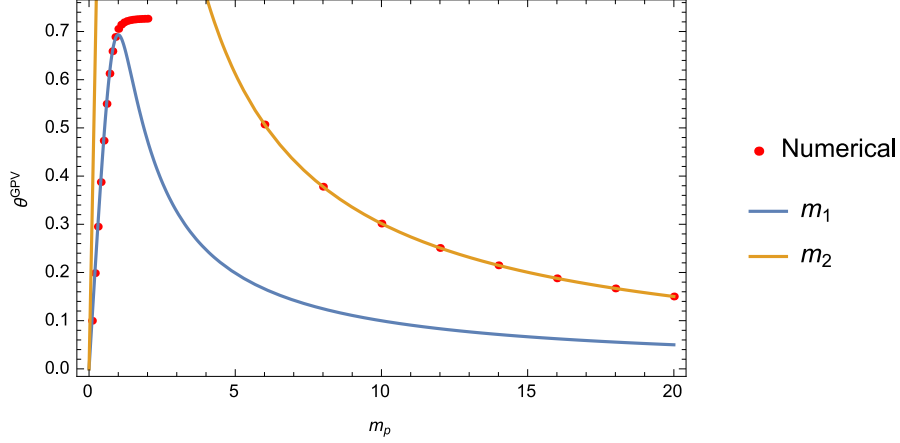


FIG. 2. The locality of the free domain wall propagator dependence of Pauli-Villars mass m_p is shown. The parameter θ^{GPV} is locality weight, which is defined as $e^{-\theta^{\text{GPV}}t}$. Lines are theoretical predictions, and points are numerical results.

is in $-1/4 < W < 1/2$. For $m^2 > 1$, we obtain the relation $|1 - We^\alpha| > |1 - We^{-\alpha}|$ and it becomes constraint on the Wilson term, $W > 1/2$ or $W < -1/4$.

The Wilson term is $W = 1 - \cosh m_1$ for m_1 and then $W < 0$. We also consider m_2 . The Wilson term is $W = 1 + \cosh m_2$ for M_1 and then $W > 2$. Figure 2 shows that the numerical calculation is consistent with the theoretical one. Note that the solution near $m_p \sim 1$ which differs from the theoretical prediction seems like the cut contribution since we ignore cut structures on the Riemann surface. Above all, m_1 is the pole if $m < 1$, and m_2 is the pole if $m > 1$. Two poles are not compatible.

We note that usual choice $m_p \sim 1$ is better for the locality, but there is still exponential locality if we generalize the parameter m_p . In particular, if we consider bigger $m_p > 1$, the locality is worse than before but the $O(a)$ chirality violation suppressed by the mass m_p . Namely, we can see the trade-off the locality and chirality depending on the Pauli-Villars mass m_p .

We will use the generalized Pauli-Villars action to modify the discretization effects in the high eigenvalue region, without loss of the chirality and the exponential locality. It helps us to test the standard model by using the perturbative and numerical calculations of the Dirac eigenvalue density $\rho(\lambda)$.

$D_{\text{phys}}^{\text{GPV}}(m_f, m_p)$	$m_p < 1$	$m_p > 1$
GW $O(a)$ Chirality	Worse ($\sim 1/m_p$)	Better ($\sim 1/m_p$)
Locality weight θ^{GPV}	Worse ($\sim m_p$)	Worse ($\sim 3/m_p$)
Approximation ($p \sim 0$)	Worse	Better
Approximation ($p \sim \pi$)	Worse	Better (tuning)

TABLE II. The dependence on the Pauli-Villars mass.

III. CHARM QUARK MASS AND THE STRONG COUPLING CONSTANT FROM MOMENTS

While non-perturbative aspects are essential to understanding QCD, the perturbative region is also accessible by using a numerical simulation of lattice QCD. Non-perturbative quantities such as hadron mass spectra and decay constants are determined from long-distance correlators in conventional lattice calculations. On the other hand, we can focus on the short-distance of the correlator to extract perturbative information without lacking the non-perturbative effect. Since perturbative expansions provide precise calculations for some physical quantities, we can extract parameters in perturbation such as the quark mass and the strong coupling constant α_s if we can prepare corresponding lattice results. We also use the information on short-distance from experiments. Since the short-distance information of the vector current correlator relates to the so-called R ratio $\sigma_{e^+e^- \rightarrow q\bar{q}}/\sigma_{e^+e^- \rightarrow \mu^+\mu^-}$ with the optical theorem, we can test our lattice calculation by experiments.

In the context of the perturbative parameter extraction using the lattice simulation, the pseudo-scalar quarkonium correlator determines the charm and bottom mass and the strong coupling constant [6–8]. They focus on the so-called temporal-moments of charmonium and bottomonium correlators. Since short-distance correlators construct the temporal-moments, perturbative calculations are performed up to the order of α_s^3 . We can extract the perturbative quantities from temporal moments since the function of the strong coupling constant α_s and quark mass m represents temporal-moments $G_n(\alpha_s, m)$. We can match the corresponding lattice results to the perturbative expansions, and extract the parameters as the solutions.

We follow the same method to extract these parameters using independently generated

lattice ensembles which are generated by the number of flavors $n_f = 2 + 1$ Möbius domain-wall fermion formulation [41] for our calculation. In order to reduce discretization error which is an indispensable source of the uncertainty, we take the continuum extrapolation using the lattice data for different lattice spacings a , $a \simeq 0.080, 0.055$, and 0.044 fm. Another systematic error source depending on the ensemble generation is the light quark masses tuning. Our simulation is done in the pion mass 230–500 MeV. Although the pion mass is not physical value, the effect from this pion mass is sufficiently small for the charmonium correlators.

We also basically follow the previous works in the perturbative calculations [6–8]. For more conservative estimation of the truncation error from perturbative expansion, we use the two different renormalization scales of the $\alpha_s(\mu_\alpha)$ and the charm quark mass $m_c(\mu_m)$. Since one of the most dominant parts of uncertainty usually has no rigorous definition, our extension of the truncation error may produce a safe choice.

Our results with this extension agree with those of the previous works [6–8]. Since we utilize different formulations and different error estimation, the result has slightly more considerable uncertainty. We also check the validity of our lattice calculation by comparing to the R -ratio from experiments. This confirmation is also a test of the discretization error in heavy quarkonium correlators. The extrapolation to the continuum shows that the slope is sufficiently small; this is a confirmation that the discretization effects are under control.

The rest of this section is organized as follows. In (III A), we review the temporal-moment method to determine the charm quark mass. We show the lattice details in (III B). (III C) shows the matching between our lattice calculation to the experimental data using vector correlator. After the confirmation, we provide the temporal-moment for pseudo-scalar correlator in (III D). Each error source in this work is discussed in (III E), and then finally provides the charm quark mass m_c and the strong coupling constant α_s for \overline{MS} scheme in (III F). We conclude in (III G).

A. Temporal moments

1. Moments in the perturbation and experiments

The dimensionless pseudo-scalar and the vector charmonium current-current correlator are defined on the lattice as follows,

$$G^{PS}(t) = a^6 \sum_{\mathbf{x}} (am_c)^2 \langle 0 | j_5(\mathbf{x}, t) j_5(0, 0) | 0 \rangle, \quad (\text{III.1})$$

$$G^V(t) = \frac{a^6}{3} \sum_{k=1}^3 \sum_{\mathbf{x}} Z_V^2 \langle 0 | j_k(\mathbf{x}, t) j_k(0, 0) | 0 \rangle. \quad (\text{III.2})$$

We define the pseudo-scalar current and vector current as $j_5 = i\bar{\psi}_c \gamma_5 \psi_c$ and $j_k = \bar{\psi}_c \gamma_k \psi_c$ by the charm quark field ψ_c . In the pseudo-scalar correlator, we introduce the bare charm quark mass m_c to set the quantity as the renormalization scale invariant. We have to introduce the renormalization constant for vector current as Z_V to match our lattice calculations to perturbations.

We can construct finite quantities which has typical distance scale using even integer $n \geq 4$

$$G_n^{PS} = \sum_t \left(\frac{t}{a} \right)^n G^{PS}(t), \quad (\text{III.3})$$

$$G_n^V = \sum_t \left(\frac{t}{a} \right)^n G^V(t). \quad (\text{III.4})$$

The time coordinate t/a is defined in the range from $-T/2a+1$ to $T/2a$ with the T temporal size of the lattice.

As usual correlators of mesons, both of $G^{PS}(t)$ and $G^V(t)$ are damping exponentially as t growing at large t . On the other hand, the small t region is growing up as some power function t^n . Namely, the n -th temporal-moment has a typical scale $t \sim n/M$ with corresponding meson mass $G(t) \sim e^{-Mt}$. We show the integrand of temporal-moments with the integer $n=4, 8$, and 12 in Figure 3 as examples. All of these moments are dominated by the perturbative region $t < \pi/(300 \text{ MeV})$ with the peak point, $t \sim n/M$. The contribution from excited states slightly shifts the peak to a smaller t/a . We note the lowest moment $n = 4$ can suffer from the sizable discretization effects since it has the contribution from the region $t/a \simeq 1-2$. Then we do not use the moment of $n = 4$ for the extraction of parameters.

We can express the relation between the temporal-moment of vector currents and the

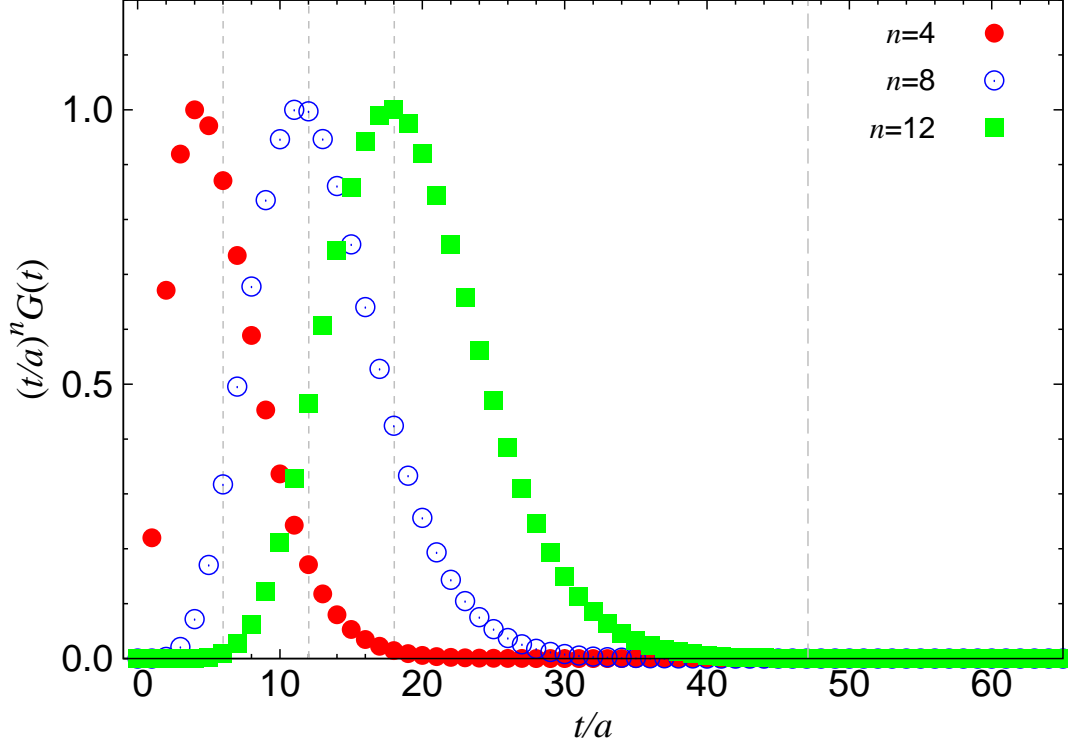


FIG. 3. The integrand of the moments $(t/a)^n G(t)$ on the $64^3 \times 128$ at $a = 0.044$ fm. We show the result $n = 4, 8$, and 12 by the filled circle, open circle, and square, respectively. Three vertical lines represent each peak position n/M . All data are normalized by its peak. Non-perturbative contribution dominated distance $t/a \sim 48$ ($\pi/(300 \text{ MeV})$) is plotted by the long-dashed line. We note that the dimensionless meson mass is $Ma = 0.6656$.

experiments. We define the vacuum polarization function $\Pi^V(q^2)$ as follow,

$$(q^\mu q^\nu - q^2 g^{\mu\nu}) \Pi^V(q^2) = i \int d^4x e^{iqx} \langle 0 | j^\mu(x) j^\nu(0) | 0 \rangle. \quad (\text{III.5})$$

The experimental data provides derivatives of the function $\Pi^V(q^2)$.

$$\frac{12\pi^2 Q_f^2}{k!} \left(\frac{\partial}{\partial q^2} \right)^k (\Pi(q^2)) |_{q^2=Q_0^2} = M_k \equiv \int_{s_0}^{\infty} ds \frac{1}{(s - Q_0^2)^{k+1}} R(s), \quad (\text{III.6})$$

using the R -ratio $R(s) \equiv \sigma_{e^+e^- \rightarrow c\bar{c}}(s) / \sigma_{e^+e^- \rightarrow \mu^+\mu^-}(s)$. Now, the charm quark electromagnetic charge is introduced as Q_f . We can tune the reference scale Q_0^2 arbitrary although we often set $Q_0^2 = 0$. The maximum of another scale s_0 is the J/ψ mass. Since the derivatives of polarization function are nothing but the temporal-moments, we define

$$g_{2k+2}^V = (2m(\mu))^{2k} \frac{12\pi^2 Q_f^2}{k!} \left(\frac{\partial}{\partial q^2} \right)^k (\Pi^V(q^2)) |_{q^2=0}, \quad (\text{III.7})$$

and then the moments on the lattice and continuum space are related by

$$G_n^V = \frac{g_n^V}{(am(\mu))^{n-2}}. \quad (\text{III.8})$$

We will show the comparison of the experimental data with our lattice calculation in (III.C). As previous studies, the moment M_n is phenomenologically estimated in [2, 11, 82, 83].

We also consider the pseudo-scalar density correlator

$$q^2 \Pi^{PS}(q^2) = i \int d^4x e^{iqx} \langle 0 | j_5(x) j_5(0) | 0 \rangle, \quad (\text{III.9})$$

without its corresponding experimental value. Again we also analogously define g_n^{PS} as in (III.7). Then the relation between the derivatives of the vacuum polarization function and the temporal-moment is represented as

$$G_n^{PS} = \frac{g_n^{PS}}{(am(\mu))^{n-4}}. \quad (\text{III.10})$$

In order to calculate the moments, we may use the parametrization which is represented as below,

$$\Pi^{PS}(q^2) = \frac{3}{16\pi^2} \sum_{k=-1}^{\infty} C_k^{PS} z^k, \quad (\text{III.11})$$

$$\Pi^V(q^2) = \frac{3}{16\pi^2} \sum_{k=-1}^{\infty} C_k^V z^k, \quad (\text{III.12})$$

with the dimensionless parameter $z = q^2/(2m_c(\mu))^2$ and coefficient C_k . These coefficients C_k are expanded by perturbation theory in terms of α_s/π :

$$\begin{aligned} C_k &= C_k^{(0)} + \frac{\alpha_s(\mu)}{\pi} \left(C_k^{(10)} + C_k^{(11)} l_m \right) \\ &+ \left(\frac{\alpha_s(\mu)}{\pi} \right)^2 \left(C_k^{(20)} + C_k^{(21)} l_m + C_k^{(22)} l_m^2 \right) \\ &+ \left(\frac{\alpha_s(\mu)}{\pi} \right)^3 \left(C_k^{(30)} + C_k^{(31)} l_m + C_k^{(32)} l_m^2 + C_k^{(33)} l_m^3 \right) + \dots \end{aligned} \quad (\text{III.13})$$

with the quark mass running contribution $l_m = \log(m_c^2(\mu)/\mu^2)$. These coefficients in conventional $\overline{\text{MS}}$ renormalization scheme are known up to $O(\alpha_s^3)$ [1, 2, 7, 82–87]. Table III summarize the coefficients for $n_f = 4$ for convenience.

n	k	$C_k^{(0)}$	$C_k^{(10)}$	$C_k^{(11)}$	$C_k^{(20)}$	$C_k^{(21)}$	$C_k^{(22)}$	$C_k^{(30)}$	$C_k^{(31)}$	$C_k^{(32)}$	$C_k^{(33)}$
4	1	1.33333	3.11111	0.00000	0.115353	-6.48148	0.00000	-1.22241	2.50084	13.5031	0.00000
6	2	0.533333	2.06420	1.06667	7.23618	1.590947	-0.0444444	7.06593	-7.58522	0.550549	0.0320988
8	3	0.304762	1.21171	1.21905	5.99920	4.33726	1.16825	14.5789	7.36258	4.25232	-0.0649030
10	4	0.203275	0.712756	1.21905	4.26701	4.80644	2.38730	13.3285	14.7645	11.0345	1.45891
12	5	0.1478	0.4013	1.1821	2.9149	4.3282	3.4971		16.0798	16.6772	4.4685
14	6	0.1137	0.1944	1.1366	1.9656	3.4173	4.4992		14.1098	19.9049	8.7485
16	7	0.0909	0.0500	1.0912	1.3353	2.2995	5.4104		10.7755	20.3500	14.1272
18	8	0.0749	-0.0545	1.0484	0.9453	1.0837	6.2466		7.2863	17.9597	20.4750

TABLE III. $n_f = 4$ coefficients for the pseudo-scalar correlator from perturbation in [1, 2].

n	k	$C_k^{(0)}$	$C_k^{(10)}$	$C_k^{(11)}$	$C_k^{(20)}$	$C_k^{(21)}$	$C_k^{(22)}$	$C_k^{(30)}$	$C_k^{(31)}$	$C_k^{(32)}$	$C_k^{(33)}$
4	1	1.06667	2.55473	2.13333	2.49671	3.31303	-0.0888889	-5.64043	4.06686	0.959031	0.0641975
6	2	0.457142	1.10956	1.82857	2.77702	5.14888	1.75238	-3.49373	6.72161	6.49161	-0.0973544
8	3	0.270899	0.519396	1.62540	1.63882	4.72072	3.18307	-2.83951	7.57355	13.1654	1.94521
10	4	0.1847	0.2031	1.4776	0.7956	3.6440	4.3713	-3.349	4.9487	17.4612	5.5856
12	5	0.1364	0.0106	1.3640	0.2781	2.3385	5.3990		0.9026	18.7458	10.4981
14	6	0.1061	-0.1158	1.2730	0.0070	0.9553	6.3121		-3.1990	16.9759	16.4817
16	7	0.0856	-0.2033	1.1982	-0.0860	-0.4423	7.1390		-6.5399	12.2613	23.4000
18	8	0.0709	-0.2660	1.1351	-0.0496	-1.8261	7.8984		-8.6310	4.7480	31.1546

TABLE IV. $n_f = 4$ coefficients for the vector correlator from perturbation in [1, 2, 85].

2. Formulae for the extraction of m_c and α_s

We follow the method in [6, 7]. The lattice and perturbative moments determine m_c and α_s as the solution of equality. From now on we sometimes neglect superscript PS for simplicity.

We introduce the reduced moment R_n to reduce discretization effects. Using the tree

level moments $G_n^{(0)}$ with the same lattice formulation,

$$R_n = \begin{cases} \frac{G_4}{G_4^{(0)}} & \text{for } n = 4, \\ \frac{am_{\eta_c}}{2a\tilde{m}_c} \left(\frac{G_n}{G_n^{(0)}} \right)^{1/(n-4)} & \text{for } n \geq 6. \end{cases} \quad (\text{III.14})$$

$$R_n^V = \frac{am_{J/\psi}}{2a\tilde{m}_c} \left(\frac{G_n^V}{G_n^{V(0)}} \right)^{1/(n-2)} \quad \text{for } n \geq 4. \quad (\text{III.15})$$

with the meson mass from lattice calculation m_{η_c} and $m_{J/\psi}$. We also define the charm quark pole mass \tilde{m}_c for the reduced moment. The pole mass is given at tree-level domain-wall fermions as

$$a\tilde{m}_c = am_c \left[1 - \frac{1}{6}(am_c)^2 - \frac{7}{40}(am_c)^4 - \frac{5}{112}(am_c)^6 + \frac{53}{1152}(am_c)^8 + \dots \right] \quad (\text{III.16})$$

as a function of the quark mass am_c which is the input parameter of the lattice simulation. The propagator of domain-wall fermion formulation at the tree-level on the lattice is written as [81]

$$\langle q(-p)q(p) \rangle = \frac{-i\gamma_\mu \sin p_\mu + m(1 - We^{-\alpha})}{-(1 - We^\alpha) + m^2(1 - We^{-\alpha})}, \quad (\text{III.17})$$

where the Wilson term $W(p)$ is

$$W(p) = 1 - M - r \sum_{\mu} (1 - \cos p_\mu). \quad (\text{III.18})$$

We use the parameters $M = 1$ and $r = -1$ in our simulations.

The pole mass at the tree-level \tilde{m}_1 is found as a pole of $\langle q(-p)q(p) \rangle$. We solve the equation to define the pole $p_0 = i\tilde{m}_1$ for zero spatial momentum. The result is

$$\tilde{m}_1 = \cosh^{-1} \left(\frac{1 - Q + \sqrt{3Q + Q^2}}{2} \right) \quad (\text{III.19})$$

with $Q = ((1 + m^2)/(1 - m^2))^2$.

The pole mass correction starts at $(am_c)^2$, and its size is 3.9% at $am_c = 0.4404$ even for our coarsest lattice setup. We expect that the correction partially eliminates the discretization effect in the calculation of am_{η_c} . The ratio in (III.14) also reduces the discretization effects at the leading order $O(\alpha_s^0)$. Then the remaining uncertainty starts at $O(\alpha_s a^2)$ since the domain-wall fermion is a kind of $O(a)$ -improved lattice actions.

We use another definition \tilde{R}_n which is introduced in [8]:

$$\tilde{R}_n = \frac{a}{a\tilde{m}_c} \left(\frac{G_n}{G_n^{(0)}} \right)^{1/(n-4)} \quad \text{for } n \geq 6. \quad (\text{III.20})$$

This definition is free from the fitting uncertainty of the meson mass since it does not include the meson mass am_{η_c} . However, this definition contains the lattice spacing a explicitly. Then the error of the lattice spacing is directly reflected in the result of α_s and m_c . In our case, this uncertainty is about 1.7% which inevitably appeared in the final results. For that reason, we use R_n to provide a precise determination. With R_n , there is no “direct” uncertainty from the lattice spacing since the meson mass effectively sets the scale to determine m_c in (III.14) (or in (III.15)). In our case, this is an advantage of R_n .

We also introduce the reduced moment r_n in the continuum. Using the derivatives of the vacuum polarization function $q^2\Pi(q^2)$ with respect to q^2

$$g_{2k} \equiv \frac{12\pi^2 Q_f^2}{k!} \left(\frac{\partial}{\partial z} \right)^k (z\Pi(q^2)) \Big|_{q^2=0} = \frac{12\pi^2 Q_f^2}{(k-1)!} \left(\frac{\partial}{\partial z} \right)^{k-1} (\Pi(q^2)) \Big|_{q^2=0}, \quad (\text{III.21})$$

we define the reduced moment in the continuum as

$$r_n = \begin{cases} g_4/g_4^{(0)} = C_1/C_1^{(0)} & \text{for } n = 4, \\ (g_n/g_n^{(0)})^{1/(n-4)} = (C_{n/2-1}/C_{n/2-1}^{(0)})^{1/(n-4)} & \text{for } n \geq 6. \end{cases} \quad (\text{III.22})$$

$$r_n^V = (g_n^V/g_n^{V(0)})^{1/(n-2)} = (C_{n/2-1}/C_{n/2-1}^{(0)})^{1/(n-2)} \quad \text{for } n \geq 4. \quad (\text{III.23})$$

For convinence, the tree-level moment $g_n^{(0)}$ is explicitly written as [88]

$$g_{2n+2}^{(0)} = 12\pi^2 Q_f^2 \frac{3}{8\pi^2} \frac{2^n(n-1)!}{(2n+1)!!}, \quad (\text{III.24})$$

and $g_{2k+2}^{V(0)}$ as

$$g_{2n+2}^{V(0)} = 12\pi^2 Q_f^2 \frac{1}{4\pi^2} \frac{2^n(n+1)(n-1)!}{(2n+3)!!}. \quad (\text{III.25})$$

After all the equality (III.10) can be rewritten as

$$R_n = \frac{m_{\eta_c}^{\text{exp}}}{2m_c(\mu)} r_n(\alpha_s(\mu), m_c(\mu)). \quad (\text{III.26})$$

We use this equation to match our non-perturbative lattice calculation R_n to the perturbative expansion r_n as the function of parameters $\alpha_s(\mu)$ and $m_c(\mu)$. We also discuss the ratio of the reduced moments,

$$\frac{R_n}{R_{n+2}} = \frac{r_n(\alpha_s(\mu), m_c(\mu))}{r_{n+2}(\alpha_s(\mu), m_c(\mu))}, \quad (\text{III.27})$$

since the convergence of the perturbative expansion is different from that of individual moment r_n .

We choose integer n to suppress a series of errors. The perturbative expansion is reliable in sufficiently higher scale compared to the scale Λ_{QCD} in QCD. It means that the perturbative regime is nothing but the short-distance regime. We should take the integer n as $n/M \ll \pi/\Lambda_{QCD}$. This condition determines the maximum of the integer n . We substitute $\simeq 3$ GeV as charmonium mass, and then its upper limit of n is about 10 or smaller. The non-perturbative contribution appears as the gluon condensate in the Operator Product Expansion (OPE) as is shown in (III E 2). As we discussed, the non-perturbative contribution rapidly grows for larger n as shown in (III.33).

The lower limit for n is already discussed earlier. Above all, there is a window of n to suppress the systematic uncertainties of this method. We only chose $n = 6, 8,$ and 10 in our analyses. We remark that the $n \geq 12$ are not useful practically since the perturbative calculation of $O(\alpha_s^3)$ coefficients of r_n are still unknown.

B. Lattice details

Our lattice QCD simulations are performed by using $n_f = 2 + 1$ fermions with Symanzik improved gauge actions. We take the stout smearing three times [89]. We use the Möbius domain-wall fermions [41]. Our lattice simulation has sufficiently small residual mass, *i.e.*, the mass is $O(1$ MeV) for our coarsest lattice. Since the small residual mass shows the violation of the Ginsparg-Wilson relation, the violation in our setup is under control. Then the contribution from violation to charmonium can be neglected. We also consider the artifacts from slightly mistuned dynamical quark masses. In R_n , since the error from this deviation is also small, the uncertainty from this contribution is not severe.

To take the continuum limit and investigate finite volume effects, we prepare 15 ensembles with different parameters. We choose three different lattice spacings: $a = 0.080, 0.055,$ and 0.044 fm with the lattice size for spacial direction $L/a = 32, 48,$ and $64,$ respectively. The size corresponds to ~ 2.6 – 2.8 fm. We set the temporal size T/a to be $64, 96,$ and $128.$ We prepare 50-100 gauge configurations from 10,000 molecular dynamics trajectories in each ensemble. To improve statistical fluctuation, we use Z_2 noise with eight or twelve times charmonium calculation starting from different time slices. “#meas” on the table is the

β	a^{-1} [GeV]	$L^3 \times T(\times L_5)$	N_{src}	#meas	am_{ud}	am_s	m_π [MeV]	$m_\pi L$	id
4.17	2.453(4)	$32^3 \times 64(\times 12)$	8	800	0.0035	0.040	230(1)	3.0	C-ud2-sa
					0.007	0.030	310(1)	4.0	C-ud3-sb
					0.007	0.040	309(1)	4.0	C-ud3-sa
					0.012	0.030	397(1)	5.2	C-ud4-sb
					0.012	0.040	399(1)	5.2	C-ud4-sa
					0.019	0.030	498(1)	6.5	C-ud5-sb
					0.019	0.040	499(1)	6.5	C-ud5-sa
		$48^3 \times 96(\times 12)$	8	800	0.0035	0.040	226(1)	4.4	C-ud2-sa-L
4.35	3.610(9)	$48^3 \times 96(\times 8)$	12	600	0.0042	0.0180	296(1)	3.9	M-ud3-sb
					0.0042	0.0250	300(1)	3.9	M-ud3-sa
					0.0080	0.0180	407(1)	5.4	M-ud4-sb
					0.0080	0.0250	408(1)	5.4	M-ud4-sa
					0.0120	0.0180	499(1)	6.6	M-ud5-sb
					0.0120	0.0250	501(1)	6.6	M-ud5-sa
4.47	4.496(9)	$64^3 \times 128(\times 8)$	8	400	0.0030	0.015	284(1)	4.0	F-ud3-sa

TABLE V. The setup of lattice ensembles.

number of measurement for each ensemble.

The $Z_2 (\pm 1)$ noise on a source for charm quark propagator improves the statistical signal. We calculate propagators with the noise which is any points on a time-slice and calculate the results as the mean value. The results should be gauge invariant since any other contaminations are removed to respect local invariance of Z_2 . After all, the signal is improved.

We distinguish the lattice spacings using by a label “id”. The capital letter comes from the coarse, medium, and fine. In C and M ensembles, strange quark mass is chosen from two different values (a and b). One larger volume $48^3 \times 96$ is prepared by a lable “-L” for the coarse lattice with lightest ud quark mass to estimate the finite volume effects. Since the ud mass is the lightest one, the possible finite volume effects can be significant in our choice. The difference between C-ud2-sa and C-ud2-sa-L shows representative estimate from finite

volume effect.

We set the lattice spacing a by the scale from Wilson-flow $t_0^{1/2} = 0.1465(21)(13)$ fm as an input [90, 91]. Table V lists the corresponding values of lattice spacings a^{-1} with the statistical error in our measurement.

Since the ensemble is the same with JLQCD works, the details of the ensemble are also shown in the previous papers [92, 93]. This ensemble is also used in η' meson mass calculation, the determination of renormalization constant, and the decay constants of heavy mesons [94–96]. We use the IroIro++ code for simulation [97].

From the previous paper, we use the renormalization constant Z_V [98]. We use $Z_V = \{0.9553(92), 0.9636(58), 0.9699(47)\}$ for each beta $\beta = \{4.17, 4.35, 4.47\}$. The error is the quadrature sum of the uncertainty from statistical and systematic.

We use the charm quark mass $m_c = \{0.4404, 0.2723, 0.2105\}$ for each beta $\beta = \{4.17, 4.35, 4.47\}$. These values should be slightly shifted to the physical value, $(m_{\eta_c} + 3m_{J/\psi})/4$.

We prepare extra configuration with different charm quark masses to interpolate to $(m_{\eta_c} + 3m_{J/\psi})/4$. Even if the calculation from these extra configurations are not so precise since the correlators are calculated with a local source, the precision is enough to interpolate the primary results to the correct charm quark mass.

For precision, we should consider the disconnected diagrams which are not taken into account in our lattice calculation. The flavor-singlet operators such as $j_5 = \bar{\psi}_c \gamma_5 \psi_c$ can generate this contribution. This lack of disconnected diagrams does not matter to match the perturbative and lattice calculations since one can omit the diagrams from perturbative expansion. Since we use the η_c or J/ψ mass as an input parameter for lattice calculation to tune input mass parameters, the lack of disconnected diagrams and electromagnetic correction can contribute to our results as error sources. We will discuss these sources of uncertainties in (III F).

C. Vector current correlator and experimental data

We compare the temporal moments of the J/ψ correlator with the experimental value. We use the same quantity R_n^V for the vector moments similar to the pseudo-scalar moments (III.14). The correspondence between the lattice and the continuum is simply written down

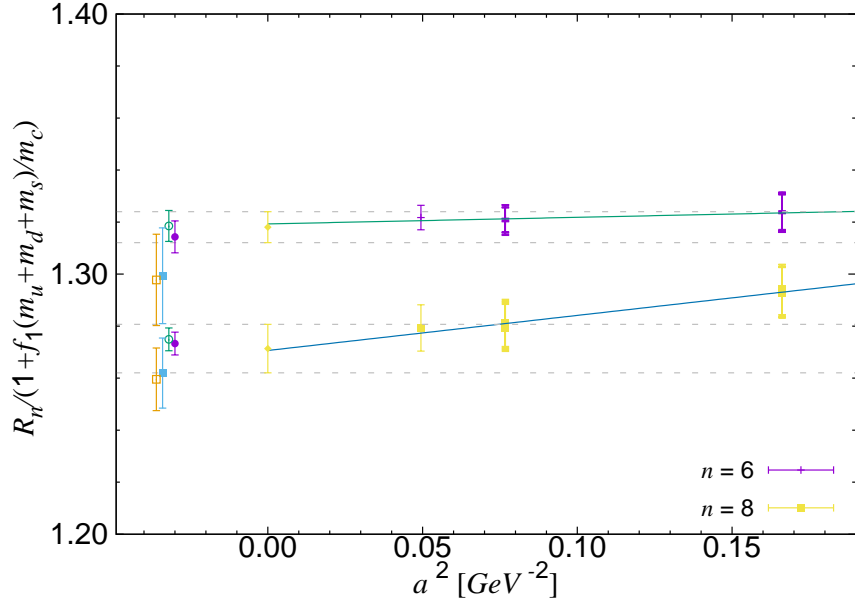


FIG. 4. The points at $a^2 = 0$ are produced by our continuum extrapolation for the vector moments R_n^V ($n = 6$ (pluses) and 8 (squares)). Phenomenological estimates of corresponding quantities are plotted on the left: Dehnadi *et al.* [10] (filled circle), Kuhn *et al.* [11] (open circle), Kuhn *et al.* [12] (filled square), and Hoang *et al.* [13] (open square).

using (III.8) as

$$R_{2k+2}^V = m_{J/\psi} \left(\frac{M_k}{g_{2k+2}^{V(0)}} \right)^{\frac{1}{2k}}. \quad (\text{III.28})$$

Table VI shows numerical results of vector reduced moments $Z_V^{-\frac{2}{n-2}} R_n^V$ for useful order n at the physical m_c . The extrapolation as a function of a^2 is plotted in Figure 4. The details of this extrapolation are discussed below.

The function for the extrapolation R_n^V is

$$R_n^V = R_n^V(0) (1 + c_1(am_c)^2) \times \left(1 + f_1 \frac{m_u + m_d + m_s}{m_c} \right), \quad (\text{III.29})$$

with free parameters $R_n^V(0)$, c_1 , and f_1 . Then the remaining error is suppressed as $O(a^4)$ by the $O(a^2)$ extrapolation. We estimate the systematic error of the fitting by the linear fitting on a^2 with and without the coarsest lattice point. The χ^2/dof value is slightly underestimated since we do not consider the correlated error of Z_V between different β . We use the mean value of the extrapolation with and without coarsest lattice point as our result, and estimate the systematic error using deviation from the mean value. For example, our

	$Z_V^{-\frac{2}{n-2}} R_6^V$	$Z_V^{-\frac{2}{n-2}} R_8^V$	$Z_V^{-\frac{2}{n-2}} R_{10}^V$	$Z_V^{-\frac{2}{n-2}} R_{12}^V$
C-ud2-sa	1.3563(5)	1.3101(5)	1.2722(5)	1.2429(5)
C-ud3-sb	1.3562(5)	1.3101(5)	1.2721(5)	1.2428(5)
C-ud3-sa	1.3563(5)	1.3102(5)	1.2722(5)	1.2430(5)
C-ud4-sb	1.3564(5)	1.3103(5)	1.2723(5)	1.2430(5)
C-ud4-sa	1.3576(5)	1.3112(5)	1.2731(5)	1.2437(5)
C-ud5-sb	1.3589(5)	1.3125(5)	1.2742(5)	1.2448(5)
C-ud5-sa	1.3594(5)	1.3130(5)	1.2747(5)	1.2452(5)
C-ud2-sa-L	1.3559(5)	1.3099(4)	1.2721(4)	1.2432(4)
M-ud3-sb	1.3461(7)	1.2919(6)	1.2553(6)	1.2285(6)
M-ud3-sa	1.3475(6)	1.2932(6)	1.2564(6)	1.2296(5)
M-ud4-sb	1.3483(7)	1.2939(6)	1.2571(6)	1.2302(6)
M-ud4-sa	1.3489(6)	1.2944(6)	1.2575(6)	1.2306(6)
M-ud5-sb	1.3499(7)	1.2953(6)	1.2583(6)	1.2312(6)
M-ud5-sa	1.3511(6)	1.2964(6)	1.2594(6)	1.2323(6)
F-ud3-sa	1.3435(7)	1.2892(6)	1.2536(6)	1.2275(6)

TABLE VI. Reduced moment $Z_V^{-\frac{2}{n-2}} R_n^V$ for each ensemble.

fit yields $\chi^2/\text{dof} = 0.17$ (0.40) for $n = 6$ (8). We also consider the systematic error from the quark mass dependence. The dependence can be tiny ($f_1 \sim 0$) if we assume the dependence is linear in $m_u + m_d + m_s$. We can ignore its higher order contributions.

We also consider the systematic difference from the flavor number. Our lattice calculation is done by $n_f = 3$, but we have to translate it to that of $n_f = 4$ by multiplying coefficient from perturbative calculation, $r_n^V(n_f = 4)/r_n^V(n_f = 3)$. This factor is an estimation of the contribution from the charm quark loop by using the perturbation. The $O(\alpha_s^3)$ coefficients are given in [1, 2]. The coefficients are 0.9992(26), 1.0026(68), 1.0156(342) for $n = 6, 8$, and 10, respectively. For our analysis, these corrections are sufficiently small.

We summarize numerical calculation for $R_n^V(0)$ in Table VII. We estimate the perturbative error by dependence in $\mu = 2\text{--}4\text{GeV}$. Since there is no $O(\alpha_s^3)$ calculation for $n = 10$, our $n = 10$ result has larger uncertainty. Our results at the continuum limit can be compared

	Our results		Phenomenological estimates			
	$n_f = 3$	$n_f = 4$	[10]	[11]	[12]	[13]
$R_6^V(0)$	1.3191(33)(12)(4)(34)	1.3181(33)(13)(4)(33)(34)	1.3143(61)	1.3185(59)	1.2994(184)	1.2978(176)
$R_8^V(0)$	1.2680(22)(7)(2)(28)	1.2714(22)(8)(2)(28)(86)	1.2732(44)	1.2749(44)	1.2620(135)	1.2596(120)
$R_{10}^V(0)$	1.2365(16)(13)(0)(22)	1.2558(16)(13)(0)(22)(423)	1.2439(35)	1.2447(34)	1.2352(104)	1.2330(91)

TABLE VII. Reduced moments $R_n^V(0)$ at continuum limit. The errors in “Our results” are statistical, discretization, finite volume, and the input value of $t_0^{1/2}$, respectively. $n_f = 3$ is our lattice calculation, while $n_f = 4$ are the corrected value by $r_n(n_f = 4)/r_n(n_f = 3)$. We add the error for “ $n_f = 4$ ” from the truncation of perturbation. Phenomenological estimates from [10–13] are also shown.

with the phenomenological estimates [10–13, 99]. This is remarkable since the results are consistent with the comparable uncertainty from the updated estimates in [10, 11].

D. Pseudoscalar current correlator

We also calculate the temporal moment of pseudoscalar current correlator R_n , and we summarize moments in Table VIII and their ratios R_n/R_{n+2} are in Table IX.

We estimate the uncertainty from finite volume using $48^3 \times 96$ (C-ud2-sa-L) and $32^3 \times 64$ (C-ud2-sa). They are sizable discrepancies for $n = 4$ and 6. On the other hand, the values coincide for R_8 , R_{10} , and R_{12} . We assume the similar finite volume effects are in any other ensembles. It should be a conservative estimation since the finite volume effects are more severe for lighter dynamical sea quarks. Except for the ensemble (C-ud2-sa), our setup satisfies $m_\pi L > 3.9$. The finite volume effects are not crucial as is shown in the final results (Table XI) since the other uncertainty is more substantial about the order of magnitude. Namely, finite volume effects is negligible at least present calculation.

We should interpolate the temporal moment R_n to the physical charmonium mass point considering the spin averaged mass $(m_{\eta_c} + 3m_{J/\psi})/4$ coincide with the experiment, 3.0687 GeV. We assume the slope in m_π^2 is independent of β to extrapolate our results to the physical pion mass as shown in Figure 5. The χ^2/dof is 1.9.

The results of our lattice calculations are slightly lower than the experimental results at

	R_6	R_8	R_{10}	R_{12}
C- <i>ud2-sa</i>	1.4689(6)	1.3681(5)	1.3087(4)	1.2679(4)
C- <i>ud3-sb</i>	1.4696(5)	1.3686(5)	1.3090(4)	1.2682(4)
C- <i>ud3-sa</i>	1.4692(5)	1.3683(5)	1.3089(4)	1.2681(4)
C- <i>ud4-sb</i>	1.4696(6)	1.3687(5)	1.3091(4)	1.2683(4)
C- <i>ud4-sa</i>	1.4706(5)	1.3693(5)	1.3097(4)	1.2687(4)
C- <i>ud5-sb</i>	1.4720(5)	1.3705(5)	1.3107(4)	1.2696(4)
C- <i>ud5-sa</i>	1.4722(6)	1.3708(5)	1.3109(4)	1.2699(4)
C- <i>ud2-sa-L</i>	1.4693(5)	1.3684(4)	1.3091(4)	1.2685(4)
M- <i>ud3-sb</i>	1.4869(6)	1.3598(5)	1.2977(5)	1.2582(4)
M- <i>ud3-sa</i>	1.4882(6)	1.3609(5)	1.2986(5)	1.2590(4)
M- <i>ud4-sb</i>	1.4888(7)	1.3611(6)	1.2987(5)	1.2590(5)
M- <i>ud4-sa</i>	1.4896(6)	1.3618(5)	1.2994(5)	1.2596(4)
M- <i>ud5-sb</i>	1.4899(7)	1.3621(5)	1.2996(5)	1.2598(5)
M- <i>ud5-sa</i>	1.4912(6)	1.3631(5)	1.3005(4)	1.2605(4)
F- <i>ud3-sa</i>	1.4961(6)	1.3616(5)	1.2987(5)	1.2590(4)

TABLE VIII. Reduced moment R_n with statistical error.

the physical pion mass. We correct the 0.1–0.3% deviation originated from the mistuning of the input parameter m_c by using the supplemental data which has three independent m_c 's for each β .

We plot the interpolation of R_6 at $\beta = 4.47$. to physical $a(m_{\eta_c} + 3m_{J/\psi})/4$ (filled square) in Figure 6. We use the slope from the supplemental data to correct our data. Although our supplemental data has a more substantial statistical error, the precision is sufficient to correct our data. The correction factor is $\sim 0.03\%$. We ignore this correlation among the three data points since the correlation only has a small effect on the final result.

The error from $t_0^{1/2}$ propagates to our result through the determination of m_c . To estimate the error propagation, we repeat the following analysis with lattice spacing a set to the maximum and minimum of its one standard deviation.

	R_6/R_8	R_8/R_{10}	R_{10}/R_{12}
C- <i>ud2-sa</i>	1.07365(8)	1.04540(3)	1.03216(2)
C- <i>ud3-sb</i>	1.07381(7)	1.04548(3)	1.03220(2)
C- <i>ud3-sa</i>	1.07368(7)	1.04542(3)	1.03217(2)
C- <i>ud4-sb</i>	1.07377(7)	1.04547(3)	1.03221(2)
C- <i>ud4-sa</i>	1.07396(7)	1.04555(3)	1.03226(2)
C- <i>ud5-sb</i>	1.07406(7)	1.04563(3)	1.03234(2)
C- <i>ud5-sa</i>	1.07400(8)	1.04563(3)	1.03235(2)
C- <i>ud2-sa-L</i>	1.07369(5)	1.04529(2)	1.03204(1)
M- <i>ud3-sb</i>	1.09346(11)	1.04783(5)	1.03144(3)
M- <i>ud3-sa</i>	1.09360(9)	1.04792(4)	1.03151(2)
M- <i>ud4-sb</i>	1.09380(12)	1.04801(5)	1.03157(3)
M- <i>ud4-sa</i>	1.09384(12)	1.04802(5)	1.03158(3)
M- <i>ud5-sb</i>	1.09388(12)	1.04808(5)	1.03162(3)
M- <i>ud5-sa</i>	1.09401(9)	1.04814(4)	1.03167(2)
F- <i>ud3-sa</i>	1.09882(10)	1.04839(4)	1.03150(3)

TABLE IX. Ratios of the reduced moment R_n/R_{n+2} with statistical error.

We assume the form similar to (III.29) to extrapolate R_n :

$$R_n = R_n(0) (1 + c_1(am_c)^2) \times \left(1 + f_1 \frac{m_u + m_d + m_s}{m_c} \right). \quad (\text{III.30})$$

We show the extrapolation in Figure 7.

The systematic error in the extrapolation is estimated by the difference between extrapolations with and without coarsest lattice data. Besides, the dependence of the lattice spacings and input masses are insignificant. The value of χ^2/dof is 2.1, 4.1, 5.1, 4.6, and 3.9 for R_6 , R_8 , R_{10} , R_{12} , and R_{14} , respectively.

The results for $R_n(0)$ are summarized in Table X with the series of systematic errors. We modify our lattice calculation for $n_f = 3$ to $n_f = 4$ multiplying by the perturbatively estimated factor $r_n(n_f = 4)/r_n(n_f = 3)$. This is numerically 1.0031, 1.0014, and 1.0026 for $n = 6, 8$, and 10 , respectively. We also listed corrected values on Table X.

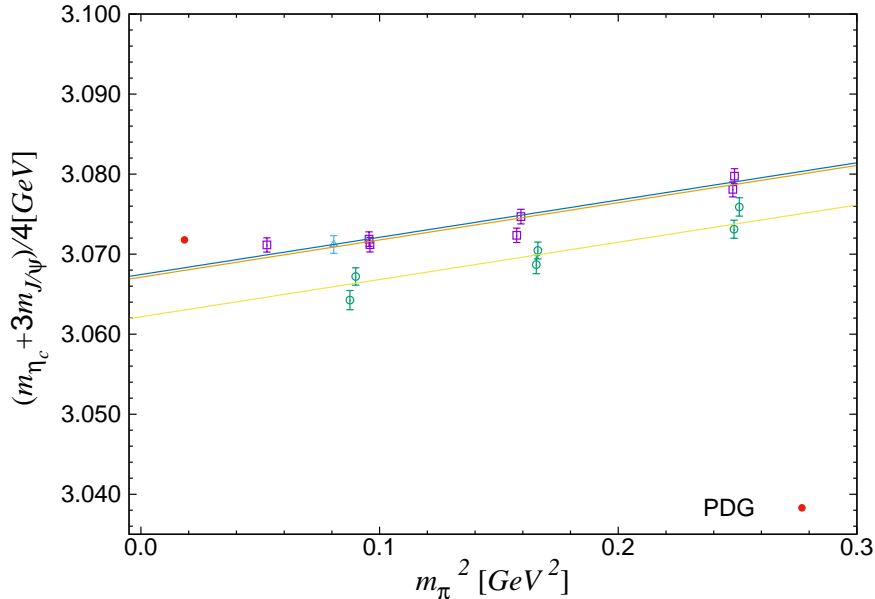


FIG. 5. Spin-averaged mass $(m_{\eta_c} + 3m_{J/\psi})/4$ as a function of m_{π}^2 . A filled circle is an experimental value, 3.072 GeV. Data at $\beta = 4.17$ (square), $\beta = 4.35$ (circle), and $\beta = 4.47$ (triangle) are plotted.

	$n_f = 3$	$n_f = 4$
$R_6(0)$	1.5048(5)(5)(4)(66)	1.5094(5)(5)(4)(66)
$R_8(0)$	1.3570(4)(22)(3)(39)	1.3589(4)(22)(3)(39)
$R_{10}(0)$	1.2931(4)(27)(5)(27)	1.2965(4)(27)(5)(27)
$R_6(0)/R_8(0)$	1.1089(1)(13)(0)(17)	1.1108(1)(13)(0)(17)
$R_8(0)/R_{10}(0)$	1.0494(0)(5)(1)(8)	1.0481(0)(5)(1)(8)

TABLE X. Reduced moments R_n and their ratios. $n_f = 3$ denotes our calculation of $n_f = 2 + 1$, and $n_f = 4$ are corrected value by a factor $r_n(n_f = 4)/r_n(n_f = 3)$ for R_n or $(r_n(n_f = 4)/r_n(n_f = 3))/(r_{n+2}(n_f = 4)/r_{n+2}(n_f = 3))$ for R_n/R_{n+2} . The errors represent statistical, discretization effect, finite volume effect, and the input value of $t_0^{1/2}$ in the order given.

E. Estimates of systematic errors

In order to extract the strong coupling constant and the charm quark mass as summarized in Section III A, we need to estimate systematic errors from several sources. We precisely discuss systematic errors.

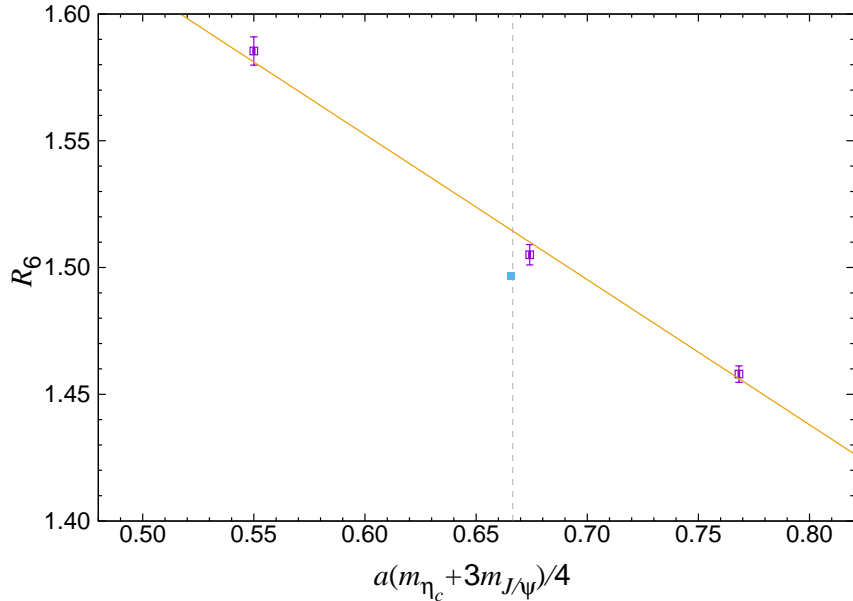


FIG. 6. We plot the interpolation of R_6 at $\beta = 4.47$. to physical $a(m_{\eta_c} + 3m_{J/\psi})/4$ (filled square). The extra data set (open square) and physical spin-averaged mass (dashed line) are also shown.

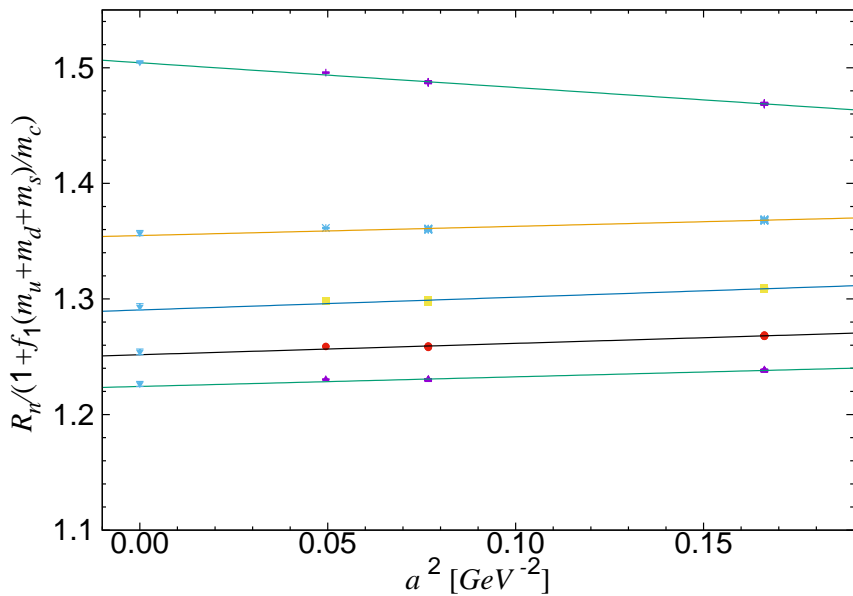


FIG. 7. R_6 , R_8 , R_{10} , R_{12} , and R_{14} are shown from top to bottom. The continuum extrapolation by (III.30) are drawn by lines. We use the mean value of the extrapolated points two (without coarsest lattice spacings) or three data as the result of $a = 0$.

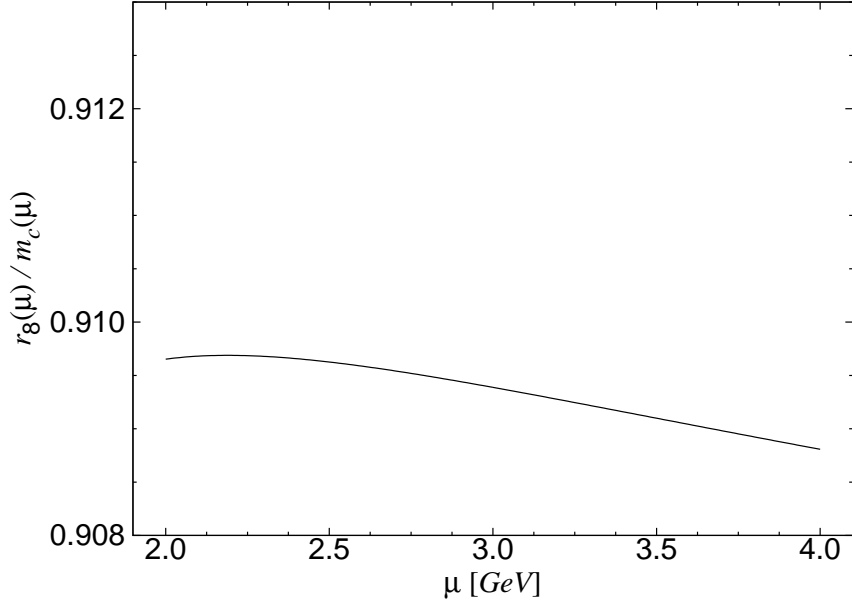


FIG. 8. Residual scale dependence of $r_n(\mu)/m_c(\mu)$.

1. Truncation of perturbative expansion

Since the perturbative expansion is known up to $O(\alpha_s^3)$ which is summarized in Table III, there is systematic error from the $O(\alpha_s^4)$ contribution. We estimate this truncation error from the residual μ dependence of $r_n(\alpha_s(\mu), m_c(\mu))/m_c(\mu)$. Since the lattice calculation (III.26) is a value without the scale μ , our procedure can estimate the systematic uncertainty. We set the scale $\mu = 3$ GeV and estimate the systematic error in the range of ± 1 GeV. We show an example for $n = 8$ on Figure 8. The μ dependence of the r_n and m_c is almost canceled with each other, but still has small non-zero remnant dependence of μ . We estimate the truncation error by using this dependence.

We generalize this argument to different scales for $\alpha_s(\mu)$ and $m_c(\mu)$. We reorganize the perturbative expansion in terms of $\alpha_s(\mu_\alpha)$ and $m_c(\mu_m)$ with $\mu_\alpha \neq \mu_m$ [10, 99]. Namely, we substitute an expansion of $\alpha_s(\mu = \mu_m)$ in terms of $\alpha_s(\mu_\alpha)$ into the expansion of $r_n(\alpha_s(\mu), m_c(\mu))$ and rearranging the series.

After the generalization, the error is calculated with the analysis in $\mu_\alpha = \mu_m \pm 1$ GeV with $2 \text{ GeV} \leq \min\{\mu_\alpha, \mu_m\}$ and $\max\{\mu_\alpha, \mu_m\} \leq 4 \text{ GeV}$. This estimate provides more conservative errors than merely taking $2 \text{ GeV} \leq \mu_\alpha = \mu_m \leq 4 \text{ GeV}$. Since the error is the dominant part, our final results have a more substantial truncation error than those in the

previous works.

2. Non-perturbative corrections

In the operator product expansion, we should consider the non-perturbative corrections to correct the perturbative series. We should carefully examine the power corrections before introducing the perturbative series.

At the lowest non-trivial order, the gluon condensate $\langle(\alpha_s/\pi)G_{\mu\nu}^2\rangle$ appears [100]. The $O(\alpha_s^2)$ calculation is done as

$$\frac{\partial}{\partial q^2} (z\Pi(q^2)^{GG}) = \frac{\partial}{\partial q^2} \left(\frac{\langle(\alpha_s/\pi)G_{\mu\nu}^2\rangle}{(2m_{\text{OS}})^4} \sum_{\ell} \left(a_{\ell} + \frac{\alpha_s}{\pi} c_{\ell} \right) z^{\ell} \right). \quad (\text{III.31})$$

Here we use m_{OS} as an on-shell heavy quark mass, and a_{ℓ} and c_{ℓ} are numerical coefficients which may be found in [100]. We can translate the on-shell mass m_{OS} to $\overline{\text{MS}}$ mass $m_c(\mu)$ by using $m_{\text{OS}} = m_c(\mu)[1 + \alpha_s/\pi(4/3 - \log m_c(\mu)^2/\mu^2)]$ up to $O(\alpha_s^2)$ truncation.

Time moments have the correction from the contribution of gluon condensate $g_{2\ell}^{GG}$. It can be simply written as

$$g_{2\ell}^{GG} = \frac{\langle(\alpha_s/\pi)G_{\mu\nu}^2\rangle}{(2m_{\text{OS}})^4} \left(a_{\ell} + \frac{\alpha_s}{\pi} c_{\ell} \right), \quad (\text{III.32})$$

and the corresponding reduced moment r_n is written down as

$$r_n^{n-4} = \frac{1}{C_{n/2-1}^{(0)}} \left(C_{n/2-1} + \frac{16\pi^2}{3} \frac{\langle(\alpha_s/\pi)G_{\mu\nu}^2\rangle}{(2m_{\text{OS}})^4} \left(a_{n/2} + \frac{\alpha_s}{\pi} c_{n/2} \right) \right). \quad (\text{III.33})$$

In the analysis of gluon condensate, the uncertainty is large: $\langle(\alpha_s/\pi)G_{\mu\nu}^2\rangle = 0.006 \pm 0.012$ GeV⁴ from τ decay analysis [101], or based on charmonium moments $\langle(\alpha_s/\pi)G_{\mu\nu}^2\rangle = 0.005 \pm 0.004$ GeV⁴ [102, 103], 0.022 ± 0.004 GeV⁴ [104]. We do not use these value as input value and treat $\langle(\alpha_s/\pi)G_{\mu\nu}^2\rangle$ as a free parameter. We simulataneously determine $\langle(\alpha_s/\pi)G_{\mu\nu}^2\rangle$, $m_c(\mu)$, and $\alpha_s(\mu)$ from the temporal moments. For this determination, we do not need to consider the error which is originated from the gluon condensate.

3. dynamical charm quark

Although our calculation does not dynamically simulate the charm quark, the effect is expected to be small since this is $O(\alpha_s^2)$ with $1/m_c^2$ suppression. As we already discussed, we

estimate the effects using perturbative calculation of the ratio $r_n(n_f = 4)/r_n(n_f = 3)$. The correction factor is calculated up to the $O(\alpha_s^3)$ with inputs from PDG $m_c(\mu = 3 \text{ GeV}) = 0.9791 \text{ GeV}$, and $\alpha_s(\mu = 3 \text{ GeV}) = 0.2567$. For the pseudo-scalar, the numerical factor is 1.0031, 1.0014, and 1.0026 for $n = 6, 8$, and 10, respectively.

F. Determination of $m_c(\mu)$ and $\alpha_s(\mu)$

Before we extract the charm quark mass and strong coupling constant from the non-perturbative lattice calculation of R_n with perturbative one, we consider some minor correction from other systematics.

The contribution from the disconnected diagram and electromagnetic interactions are sources of error since our lattice calculations miss these effects. In our analysis, this contribution should be considered as a tiny shift of η_c and J/ψ mesons since this shift can affect the tuning of the charm quark mass and systematic error. Namely, the shift contributes to the value of $m_{\eta_c}^{\text{exp}}$ in (III.26). The previous lattice study shows that the disconnected diagram effect reduces the meson mass by 2.4(8) MeV [64]. The electromagnetic interactions also reduces the η_c mass by 2.6(1.3) MeV [105].

With all corrections, we use the meson mass as an input value $m_{\eta_c}^{\text{exp}} = 2983.6(0.7) + 2.4(0.8)_{\text{Disc.}} + 2.6(1.3)_{\text{EM}}$ MeV.

We consider discretization effects for the charmonium mass. In particular, the hyperfine splitting $\Delta_{J/\psi-\eta_c} = m_{J/\psi} - m_{\eta_c}$ is sensitive to this source of error. As is shown in Figure 9, the hyperfine splitting has a significant a^2 dependence on the lattice data. We assume a linear dependence on a^2 to extrapolate to the continuum point. The result at the continuum limit 111.4(1.8) MeV coincides with the experimental value, 110.9(2.1) MeV. This result is another evidence that our lattice simulation well controls the discretization effect of the temporal moment after the continuum extrapolation.

Finally, we extract the three value: $m_c(\mu)$, $\alpha_s(\mu)$, and $\langle(\alpha/\pi)G^2\rangle/m_{\text{OS}}^4$. We use three temporal moments R_6 , R_8 and R_{10} as inputs for (III.26). We also consider the ratio of the moment R_6/R_8 as in (III.27). Although this is not independent of individual moments, it can provide a consistency check and a different dependency of each parameter.

Figure 10 shows the constraints on $m_c(\mu)$ and $\alpha_s(\mu)$ at $\mu = 3 \text{ GeV}$ using the moments R_6 , R_8 , R_{10} , and its ratio R_6/R_8 . The gluon condensate is determined by the combination

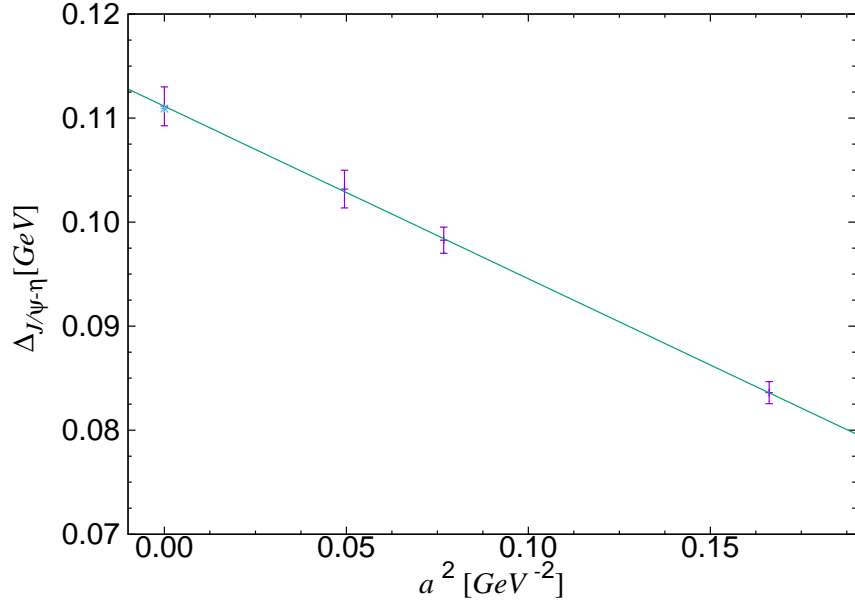


FIG. 9. Hyperfine splitting $\Delta_{J/\psi-\eta}$ and its continuum extrapolation. We add the error of lattice scale a from $t^{1/2}$ for each data point.

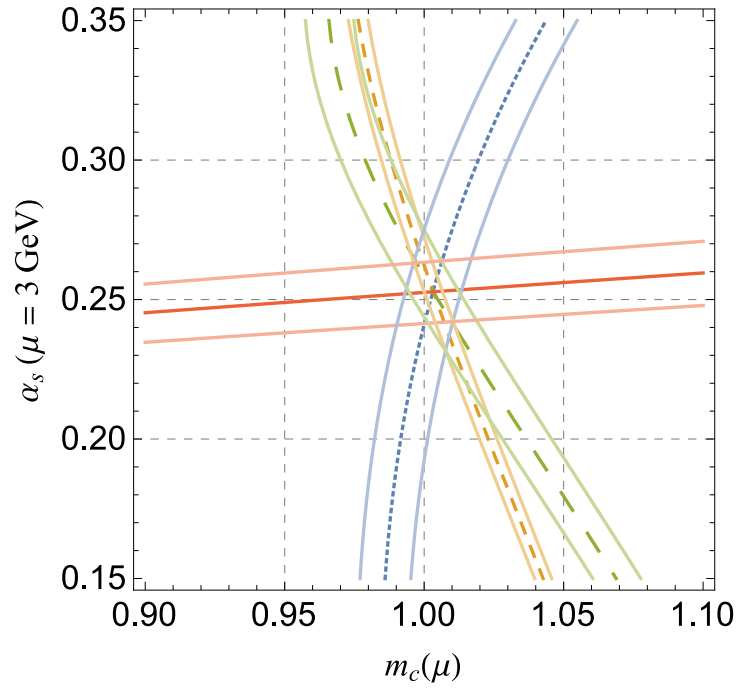


FIG. 10. Constraints on $m_c(\mu)$ and $\alpha_s(\mu)$ using R_6 (dotted curve), R_8 (dashed curve), R_{10} (long dashed curve), and R_6/R_8 (solid curve). The band represents the error from the truncation of perturbative expansion.

inputs	$m_c(\mu)$ [GeV]	pert	$t_0^{1/2}$	stat	$O(a^4)$	vol	$m_{\eta_c}^{\text{exp}}$	disc	EM
R_6, R_8, R_{10}	1.0032(98)	(82)	(51)	(5)	(16)	(4)	(3)	(4)	(6)
$R_6, R_6/R_8, R_{10}$	1.0031(194)	(176)	(78)	(6)	(18)	(5)	(4)	(4)	(7)
$R_6/R_8, R_8, R_{10}$	1.0033(96)	(77)	(49)	(4)	(30)	(4)	(3)	(4)	(6)
inputs	$\alpha_s(\mu)$	pert	$t_0^{1/2}$	stat	$O(a^4)$	vol	$m_{\eta_c}^{\text{exp}}$	disc	EM
R_6, R_8, R_{10}	0.2530(256)	(213)	(134)	(12)	(38)	(10)	(9)	(10)	(16)
$R_6, R_6/R_8, R_{10}$	0.2528(127)	(120)	(33)	(2)	(25)	(1)	(0)	(0)	(1)
$R_6/R_8, R_8, R_{10}$	0.2528(127)	(120)	(32)	(2)	(26)	(1)	(0)	(0)	(1)
inputs	$\frac{\langle(\alpha/\pi)G^2\rangle}{m^4}$	pert	$t_0^{1/2}$	stat	$O(a^4)$	vol	$m_{\eta_c}^{\text{exp}}$	disc	EM
R_6, R_8, R_{10}	-0.0005(99)	(85)	(45)	(4)	(23)	(4)	(3)	(4)	(6)
$R_6, R_6/R_8, R_{10}$	-0.0006(144)	(133)	(49)	(4)	(23)	(4)	(3)	(3)	(5)
$R_6/R_8, R_8, R_{10}$	-0.0006(78)	(68)	(29)	(3)	(22)	(3)	(2)	(3)	(5)

TABLE XI. Numerical results for $m_c(\mu)$ (top panel), $\alpha_s(\mu)$ (mid panel) and $\frac{\langle(\alpha/\pi)G^2\rangle}{m^4}$ (bottom panel). with the renormalization scale is $\mu = 3$ GeV. We also shows the estimated errors from the truncation of perturbative expansion, the input value of $t_0^{1/2}$, statistical, discretization error of $O(a^4)$ (or $O(\alpha_s a^2)$), finite volume, experimental data for $m_{\eta_c}^{\text{exp}}$, disconnected contributions, electromagnetic effects, in the order given. The total error is estimated by adding the individual errors in quadrature.

of R_6/R_8 , R_8 , and R_{10} in this plot. This figure demonstrates that each constraint has different sensitivities for $m_c(\mu)$ and $\alpha_s(\mu)$. As a typical example, the ratio R_6/R_8 is almost independent of $m_c(\mu)$ since it depends on $m_c(\mu)$ only logarithmically by definition (III.27).

Table XI lists the numerical results including the breakdown of estimated errors. We show the estimated errors from the truncation of perturbative expansion, the input value of $t_0^{1/2}$, statistical, discretization error of $O(a^4)$ (or $O(\alpha_s a^2)$), finite volume, experimental data for $m_{\eta_c}^{\text{exp}}$, disconnected contributions, electromagnetic effects, in the order given. We already discussed each error in previous sections.

We note that the truncation of the perturbative expansion is a dominant source of the uncertainty for these three quantities. As we discussed above, we estimate this error conservatively by using an independent renormalization scale for μ_m and μ_α in the range between

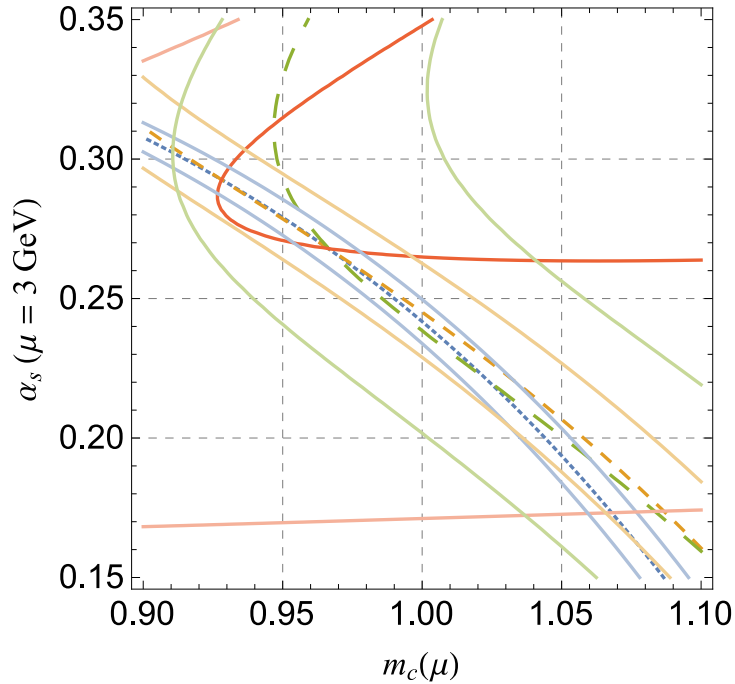


FIG. 11. Constraint from the vector-current moments R_n^V on the $(m_c(\mu), \alpha_s(\mu))$ plane. Dotted, dashed, long-dashed, and solid curves correspond to that of R_6 , R_8 , R_{10} , and R_6/R_8 , respectively.

2 GeV and 4 GeV without μ_m/μ_α being far away from 1. The subdominant part from the discretization effect of the lattice calculation. Any other sources are negligible when we take the summation in quadrature.

We do not precisely determine the gluon condensate. Our results are consistent with zero. We can understand this fact without surprise since the quantity is nothing but the small difference between the perturbative and non-perturbative calculations. It depends on the order of perturbation. Although our calculation is not so precise, it is consistent with previous studies [101–104].

We also consider the vector channel to extract three values. Unfortunately, we can not succeed as we can see in Figure 11. When we only use R_6 , R_8 , R_{10} , and their ratio, all of these have a similar dependence on the charm mass and the strong coupling⁹. Unless we use $\alpha_s(\mu)$ as an input, the determination of the charm quark mass fails. Also, the lattice calculation for the vector channel has 3–4 times larger statistical error compared to the

⁹ Although it can be different if we use R_4 , it contains too large discretization effect as we discussed.

pseudo-scalar channel.

We use the vector channel to determine Z_V in (III.2) with input for $m_c(\mu)$ and $\alpha_s(\mu)$ obtained from the pseudo-scalar channel. Our results are 0.925(19), 0.937(22) and 0.942(31) for $\beta = 4.17, 4.35$ and 4.47 , respectively. These results can be compared with the determination from the light quark-hadron correlators: 0.955(9), 0.964(6), 0.970(5) [98]. Although our data are slightly lower and have more significant errors, the ratio of these two determinations is consistent with one at the continuum limit.

G. Summary

In this work, we determine the charm quark mass $m_c(\mu)$ and strong coupling constant $\alpha_s(\mu)$ through the temporal moments of the charmonium current-current correlator on the lattice ensembles with 2+1 flavors of Möbius domain-wall fermion. The method itself was developed by the HPQCD-Karlsruhe collaboration [6–8]. We apply it to the lattice data of a different formulation.

Since the temporal moments in the vector channel relates to moments from experiments, we validate or calibrate our lattice calculations using experimental extraction. In order to determine $m_c(\mu)$ and $\alpha_s(\mu)$, we use the pseudo-scalar channel which has enough sensitivity to determine $m_c(\mu)$ and $\alpha_s(\mu)$ separately.

The sizable effect from discretization can be seen for charm quark. We control this effect by the continuum extrapolation using sufficiently small lattice spacings in the range 0.044–0.080 fm.

Our final results and the PDG numbers [106] are summarized in Table XII. Figure 12 shows our results and results from other collaborations. We chose the values of the smallest total error from Table XI as our final results. The charm quark mass $m_c(\mu = 3 \text{ GeV})$ is converted to $m_c(\mu = m_c)$, and the strong coupling constant $\alpha_s(3 \text{ GeV})$ is converted to the value at the Z boson mass scale using four-loop running formulae. The threshold effect at the bottom quark mass is incorporated at one-loop. Our extraction of $\alpha_s(M_Z)$ is consistent with the PDG.

The dominant error source is the truncation of the perturbative expansion. This uncertainty is known up to $O(\alpha_s^3)$. Because of this reason, in order to improve the precision of this method, higher order perturbative calculations are needed. At the same time, since the

	this work	PDG (2014)
$m_c(\mu = 3 \text{ GeV})$	1.0033(96) GeV	
$m_c(\mu = m_c)$	1.2871(123) GeV	1.275(25) GeV
$\alpha_s(\mu = 3 \text{ GeV})$	0.2528(127)	0.2567(34)
$\alpha_s(\mu = M_Z)$	0.1177(26)	0.1185(6)
$\Lambda_{\overline{\text{MS}}}^{n_f=4}$	286(37) MeV	297(8) MeV
$\Lambda_{\overline{\text{MS}}}^{n_f=5}$	205(32) MeV	214(7) MeV

TABLE XII. Our results and the values in the Review of Particle Properties (2014) [106] which are given in $\overline{\text{MS}}$ scheme.

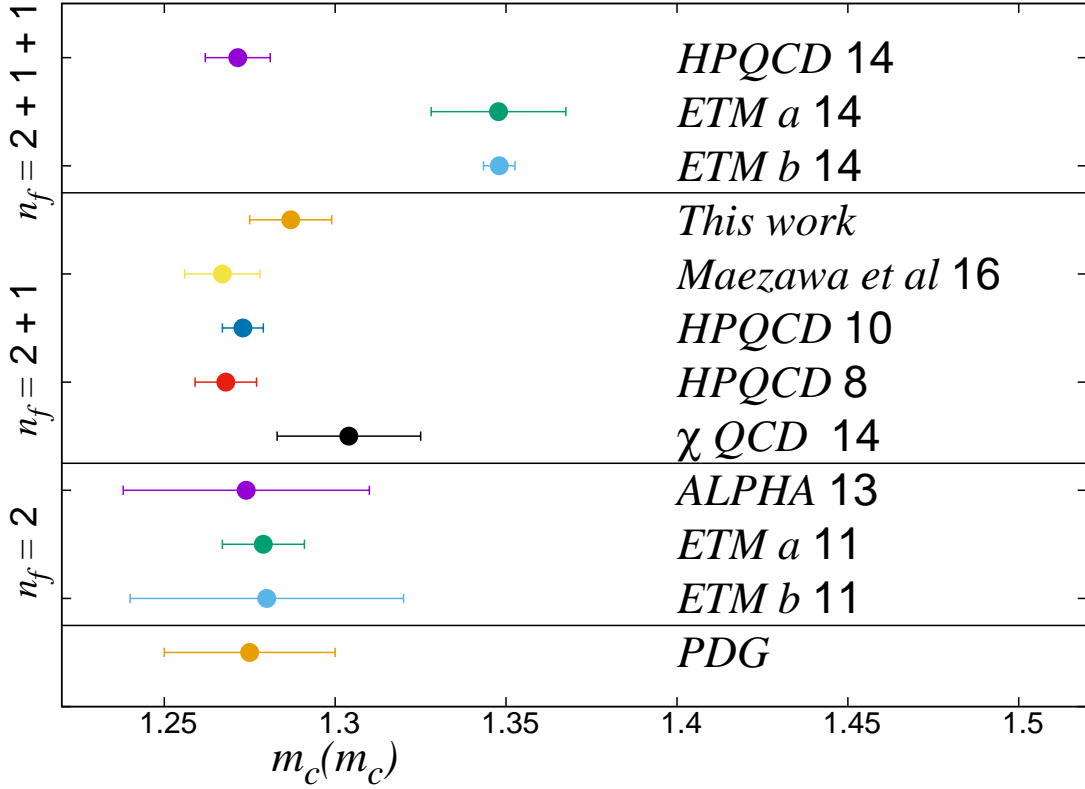


FIG. 12. Charm quark mass obtained in this work is compared with previous lattice determination. The previous results are separately shown for a different number of sea quarks. HPQCD 14 [8], ETM *a* 14 [107] and ETM *b* 14 [108] for $n_f = 2 + 1 + 1$, Maezawa *et al.* 16 [109], HPQCD 10 [7], HPQCD 08 [6], and χ QCD 14 [110] for $n_f = 2+1$, and ALPHA 13 [111], ETM *a* 11 [112], and ETM *b* 11 [113] for $n_f = 2$.

subdominant part comes from the scale uncertainty, we have to determine lattice spacings more precisely if higher order perturbative calculation will be completed.

IV. PERTURBATIVE EXPANSION OF DIRAC EIGENVALUE DENSITY

The Dirac operator D is an essential building block for QCD, and it defines the interaction between quarks and the gauge field with gauge invariance. Namely, after the path-integration of gauge configurations, the eigenvalue and eigenfunction of the Dirac operator can represent any observable consisting of quarks in QCD. Since eigenvalues are gauge invariant quantity, any observable is invariant under gauge transformations.

The eigenvalue distribution can relate to the dynamics of QCD. The Banks-Casher relation is a good example [114]. The near-zero eigenvalue density relates to the order parameter of the spontaneous chiral symmetry breaking in QCD: the chiral condensate $\langle \bar{\psi}\psi \rangle$. We can determine the chiral condensate by the numerically countings of the number of eigenvalues, utilizing this relation. In order to reduce systematic effects, we require the chiral symmetry on the lattice for the correct identification of near-zero eigenmodes. Previous works [115, 116] explicitly calculated the individual eigenvalues and its density on the lattice generated by overlap fermion formulation. We use a stochastic estimation of eigenvalue density, which is first introduced with Wilson fermions [117]. Recently we applied a slightly different stochastic approach to calculating the eigenvalue spectrum of domain-wall fermions, which are also chiral lattice fermions, and achieved a precise determination of the chiral condensate [15].

Not only the near-zero eigenvalue but also the spectrum $\rho(\lambda)$ has more information about the system. For example, we can extract the scale dependence $d\rho(\lambda)/d\lambda$. Since this scale dependence is precisely calculated in the perturbative eigenvalue scale $\lambda \gg \Lambda_{\text{QCD}}$ with the QCD scale Λ_{QCD} , we can test the perturbation theory comparing the lattice calculation to perturbation. So far, tests of high-order perturbative theory with non-perturbative lattice results have been performed for the vacuum polarization function at the order of α_s^4 [98, 118] and for the charmonium correlation function at α_s^3 [6, 9]. Moreover, stochastic perturbation theories have been applied to simple quantities such as the plaquette [119] and the static quark self-energy [120]. We perform another test at α_s^4 using the scale dependence of $\rho(\lambda)$. The precise calculation of the spectral function provides another way to determine the strong coupling constant.

We consider the so-called *conformal* regime of many-flavor QCD or related models have been studied on the lattice. The spectral function helps us to study the regime as we can

see in [121, 122] for instance. The same technique is applied to two-flavor QCD [123]. The mass anomalous dimension of fermions γ_* parametrizes the scale dependence of the spectral density. For the conformal (or scale) invariant system, the mass anomalous dimension γ_* is a constant. For QCD, the mass anomalous dimension is no longer a constant since the coupling constant runs and diverges in the low-energy region. Namely, the mass anomalous dimension does not parameterize the scale dependence of the spectral density. The subsection IV A shows details.

We calculate the Dirac spectral density in the perturbative regime. A stochastic method provides the Dirac spectral density in the whole energy range, and we use the high energy region as the regime. We extrapolate the data to the continuum limit using the results of three lattice spacings. After the extrapolation, we match our lattice calculation to the $O(\alpha_s^4)$ perturbative calculation. We also try to determine α_s .

The discretization error is crucial for our works since the high energy regime is sensitive to the uncertainty near the lattice cutoff $1/a$. We investigate the uncertainty at the tree level of the domain-wall fermion Dirac operator. From the study of the tree level, we show that the Pauli-Villars mass generalization reduces uncertainty. Domain-wall fermions are defined in five-dimension, and eigenmodes on the four-dimensional surface are identified as the physical mode. Our generalization corresponds to a slightly different procedure that eliminates the unphysical bulk effects from the five-dimensional modes. Taking the continuum limit by using a linear ansatz in a^2 , we make the discretization effects small.

This section is organized as follows. We first introduce the perturbative calculation for the Dirac spectral density in QCD in the subsection IV A. This subsection contains a review of perturbative results for the spectral function $\rho(\lambda)$ and its exponent. The subsection IV B shows the details of the perturbative coefficients. In the next subsection IV C, we discuss the discretization effects in the domain-wall fermion. The lattice setup and the procedure to calculate the eigenvalue density are shown in the subsection IV D. We compare our result with the perturbative calculation in the subsection IV E. Finally, we extract the strong coupling constant using the comparison in the subsection IV F. We use the properties for the modified Dirac operator which is discussed in the previous section.

A. Dirac eigenvalue density

The Dirac operator D eigenvalue density $\rho(\lambda)$ is represented as

$$\rho(\lambda) = \frac{1}{V} \left\langle \sum_k \delta(\lambda - \lambda_k) \right\rangle, \quad (\text{IV.1})$$

where $\langle \dots \rangle$ is an average over gauge field configurations. The λ_k is labeled by the momentum p_μ as $|\lambda_k|^2 = p_\mu^2$ in the free quark limit. In this limit, the eigenvalue density is explicitly represented as a surface of a three-dimensional sphere in momentum space: $\rho_{\text{free}}(\lambda) = (3/4\pi^2)|\lambda|^3$. In the theories that have conformal invariance or approaches a renormalization group fixed point, there is a relation $\rho_{\text{FP}} \sim |\lambda|^{4/(1+\gamma_*)-1}$. Now the mass anomalous dimension of theory γ_* is constant [124]. The relation between the eigenvalue density and the mass anomalous dimension has been used for studying the many-flavor QCD-like theories at the fixed point.

In QCD, the spectral density is perturbatively known up to the order α_s^3 [17, 18] using

$$\rho^{\overline{\text{MS}}}(\lambda) = \frac{3|\lambda|^3}{4\pi^2} \left[1 - \rho^{(1)} \frac{\alpha_s(\mu)}{\pi} - \rho^{(2)} \left(\frac{\alpha_s(\mu)}{\pi} \right)^2 - \rho^{(3)} \left(\frac{\alpha_s(\mu)}{\pi} \right)^3 + O \left(\left(\frac{\alpha_s(\mu)}{\pi} \right)^4 \right) \right], \quad (\text{IV.2})$$

with the coefficients $\rho^{(i)}$ are calculated as

$$\rho^{(1)} = 8 \left(L_\lambda - \frac{5}{12} \right), \quad (\text{IV.3})$$

$$\rho^{(2)} = \frac{1}{8} \left[\frac{1}{2} \left(52N_f - \frac{4406}{9} + \frac{32}{3}\zeta_3 \right) - \frac{32}{9}(5N_f - 141)L_\lambda + \frac{32}{9}(2N_f - 81) \left(\frac{3}{2}L_\lambda^2 - \frac{\pi^2}{8} \right) \right], \quad (\text{IV.4})$$

$$\rho^{(3)} = \frac{1}{32} \left[c_{40} \left(2L_\lambda^3 - \frac{\pi^2}{2}L_\lambda \right) + c_{41} \left(\frac{3}{2}L_\lambda^2 - \frac{\pi^2}{8} \right) + c_{42}L_\lambda + \frac{1}{2}c_{43} \right]. \quad (\text{IV.5})$$

The renormalization scale is μ in $L_\lambda \equiv \ln(\lambda/\mu)$. We also need the numerical constants $\zeta_3 \simeq 1.20205$ and $c_{40} \simeq 4533.33$, $c_{41} \simeq -11292.4$, $c_{42} \simeq 12648.1$, $c_{43} \simeq -15993.5$ for $N_f = 3$ dynamical fermion flavors [18]. $N_f = 2$ results are also in [18]. The Dirac eigenvalues and the quark mass is renormalized in the same way. After the renormalization, the eigenvalue is scale μ dependent. We often suppress this scale dependence for simplicity. The absolute value $|\lambda|$ is sometimes written as λ ¹⁰.

¹⁰ In the Euclidean continuum theory, λ is pure imaginary.

We discuss the perturbative calculation of the next order, $O(\alpha_s^4)$. Using the renormalization group equation,

$$0 = \left[\frac{\partial}{\partial \ln \mu} - \gamma_m(\alpha_s) \left(1 + \lambda \frac{\partial}{\partial \lambda} \right) + \beta(\alpha_s) \frac{\partial}{\partial \alpha_s} \right] \rho(\lambda). \quad (\text{IV.6})$$

This equation follows from the scale invariance of the mode number $\int_0^M d\lambda \rho(\lambda)$ with a parameter M [117]. We can also understand that this equation comes from the scale invariance of the $m\bar{q}q$. The renormalization group equation of the spectral function is identical to the chiral condensate $\langle \bar{q}q \rangle$ since $\rho(\lambda)$ is given by $\langle \bar{q}q \rangle$ with the artificial valence quark mass $i|\lambda|$. We define the mass anomalous dimension $\gamma_m(\alpha_s)$ and the beta function $\beta(\alpha_s)$ as

$$\beta(\alpha_s) \equiv \frac{\partial \alpha_s}{\partial \ln \mu}, \quad (\text{IV.7})$$

$$\gamma_m(\alpha_s) \equiv -\frac{\partial \ln m(\mu)}{\partial \ln \mu}, \quad (\text{IV.8})$$

which are known up to $O(\alpha_s^6)$ and $O(\alpha_s^5)$, respectively. The details are shown in the subsection IV B. We rewrite the (IV.6) using the fact that the μ -dependence of $\rho(\lambda)/\lambda^3$ is originated from $L_\lambda = \ln \lambda/\mu$,

$$(1 + \gamma_m) \frac{\partial}{\partial L_\lambda} K(\alpha_s, L_\lambda) = \left(\beta(\alpha_s) \frac{\partial}{\partial \alpha_s} - 4\gamma_m(\alpha_s) \right) K(\alpha_s, L_\lambda) \quad (\text{IV.9})$$

with $K(\alpha_s, L_\lambda)$ defined as $\rho(\lambda) = (3/4\pi^2)\lambda^3 K(\alpha_s, L_\lambda)$. We solve this equation to determine the spectral function iteratively. Since $\gamma_m(\alpha_s)$ and $\beta(\alpha_s)$ start at $O(\alpha_s)$ and $O(\alpha_s^2)$ respectively, the L_λ dependent term of $\rho(\lambda)$ can be determined up to α_s^{n+1} . While the L_λ independent term of $\rho(\lambda)$ is known at order α_s^n . The details are in the subsection IV B.

We remark that the relation $\rho(\lambda) \propto \lambda^{4/(1+\gamma_m)-1}$ is valid in QCD only at the one-loop level, *i.e.*, in $\overline{\text{MS}}$, and it is valid up to $\lambda^{3-8\alpha_s/\pi}$. This is consistent with the $\lambda^{4/(1+\gamma_m)-1}$ with the one-loop level calculation, $\gamma_m = 2\alpha_s/\pi$. The relation is violated in higher-loop order for QCD.

We also introduce $F(\lambda)$ as the exponent of the spectral function as

$$F(\lambda) \equiv \frac{\partial \ln \rho(\lambda)}{\partial \ln \lambda}. \quad (\text{IV.10})$$

We explicitly write the perturbative expansions up to order α_4 ,

$$F(\lambda) = 3 - F^{(1)} \frac{\alpha_s(\mu)}{\pi} - F^{(2)} \left(\frac{\alpha_s(\mu)}{\pi} \right)^2 - F^{(3)} \left(\frac{\alpha_s(\mu)}{\pi} \right)^3 - F^{(4)} \left(\frac{\alpha_s(\mu)}{\pi} \right)^4 + O(\alpha_s^5), \quad (\text{IV.11})$$

and the coefficients $F^{(k)}$ for $N_f = 3$ are

$$F^{(1)} = 8, \quad (\text{IV.12})$$

$$\begin{aligned} F^{(2)} &= \frac{4}{3} (22 - 27L_\lambda) \\ &= 29.3333 - 36L_\lambda, \end{aligned} \quad (\text{IV.13})$$

$$\begin{aligned} F^{(3)} &= \frac{1}{36} (6061 - 9216L_\lambda + 5832L_\lambda^2 - 1350\pi^2 - 936\zeta_3) \\ &= -233.003 - 256L_\lambda + 162L_\lambda^2, \end{aligned} \quad (\text{IV.14})$$

$$\begin{aligned} F^{(4)} &= \frac{1}{5184} [(-3583861 + 1015200\pi^2 - 69984\bar{\rho}^{(3)} + 3888\pi^4 - 315168\zeta_3 - 432000\zeta_5) \\ &\quad + (-10980576 + 2624400\pi^2 + 1819584\zeta_3) L_\lambda + 8771328L_\lambda^2 - 3779136L_\lambda^3] \\ &= -1348.6655 + 3300.2425L_\lambda + 1692L_\lambda^2 - 729L_\lambda^3, \end{aligned} \quad (\text{IV.15})$$

where $\zeta_5 \simeq 1.03692$, and $\bar{\rho}^{(3)}$ is the value of $\rho^{(3)}$ at $\lambda = \mu$, $-\bar{\rho}^{(3)} = -c_{43}/(64\pi^3) + c_{41}/(256\pi)$ which is from (IV.5). The exponent $F(\lambda)$ is also provided in the $\overline{\text{MS}}$ scheme. It depends on the renormalization scale μ .

We can extract the term of $O(\alpha_s^5)$ except for the L_λ independent term. We introduce an unknown constant $\bar{\rho}^{(4)}$ analogue with $\bar{\rho}^{(3)}$, and then the term at $O(\alpha_s^5)$ is represented as

$$\begin{aligned} F^{(5)} &= \frac{1}{108864} \left[-30717197 + 85848525\pi^2 + 6858432\bar{\rho}^{(3)} - 16438275\pi^4 \right. \\ &\quad - 1959552\bar{\rho}^{(4)} + 54000\pi^6 - 51803465\zeta_3 - 5443200\pi^2\zeta_3 \\ &\quad + 73592064\zeta_3^2 - 280468510\zeta_5 + 179028360\zeta_7 \\ &\quad + L_\lambda (1526603652 - 395992800\pi^2 + 26453952\bar{\rho}^{(3)}) \\ &\quad \quad - 1469664\pi^4 + 66824352\zeta_3 + 163296000\zeta_5) \\ &\quad + L_\lambda^2 (1986475428 - 496011600\pi^2 - 343901376\zeta_3) \\ &\quad \quad \left. - 1087551360L_\lambda^3 + 357128352L_\lambda^4 \right] \\ &= -18.0000\bar{\rho}^{(4)} + 3751.43 + 24167.1L_\lambda - 30518.4L_\lambda^2 - 9990L_\lambda^3 + \frac{6561}{2}L_\lambda^4, \end{aligned} \quad (\text{IV.16})$$

where $\zeta_7 \simeq 1.00835$.

We estimate the uncertainty from the unknown constant $\bar{\rho}^{(4)}$. Since we use λ in the range 0.8–1.2 GeV for determination of $\alpha_s(\mu)$, we take $\lambda = 1.2$ GeV as a typical value in the estimation. The series (IV.11) is simple at $\mu = \lambda$,

$$F(\lambda)_{\mu=\lambda} = 3 - 2.54648\alpha_s - 2.97209\alpha_s^2 + 7.51469\alpha_s^3 + 13.8454\alpha_s^4 - d_5\alpha_s^5 + \dots \quad (\text{IV.17})$$

The unknown constant $d_5 = (-18.0000\bar{\rho}^{(4)} + 3751.43)/\pi^5$ is contained in the last term. We can assume the size of d_5 is about 25 since the coefficient grows by a factor of 2 from any order to the next in (IV.17). We allow ± 50 for the error from d_5 conservatively. The size of $O(\alpha_s^5)$ is 18% of the total at $\mu = 1.2$ GeV.

The uncertainty from this unknown constant depends on the renormalization scale μ . Namely, we also show exponents in $\mu = 2.5\lambda$ and 5λ ,

$$F(\lambda)_{\mu=2.5\lambda} = 3 - 2.54648\alpha_s - 6.31432\alpha_s^2 - 4.43721\alpha_s^3 + 24.5484\alpha_s^4 - (d_5 - 123.421)\alpha_s^5 + \dots, \quad (\text{IV.18})$$

and

$$F(\lambda)_{\mu=5\lambda} = 3 - 2.54648\alpha_s - 8.84261\alpha_s^2 - 19.3071\alpha_s^3 - 7.81967\alpha_s^4 - (d_5 - 177.403)\alpha_s^5 + \dots. \quad (\text{IV.19})$$

Although some coefficients are larger than those of $\mu = \lambda$, we should pay attention to the value of α_s . Since $\alpha_s(3 \text{ GeV}) = 0.244$ and $\alpha_s(6 \text{ GeV}) = 0.191$ are smaller than $\alpha_s(1.2 \text{ GeV}) = 0.406$, the uncertainty from d_5 is 1.4% and 0.4% for $\mu = 2.5\lambda$ and 5λ , respectively¹¹. For the case of $\mu = 5\lambda$, we roughly estimate the μ -dependent coefficient to be a factor of 4 from any order to the next. We also estimate one higher order contribution as $\sim \pm 700\alpha_s^6$. This contribution is 2.6% for $F(\lambda)$. We use this estimate for our result of $\alpha_s(6 \text{ GeV})$ from (IV.19).

We show the convergence of the perturbative expansion for $F(\lambda)$ in Figure 13 with unknown parameter $d_5 = 0$. The figure clearly shows a bad convergence of $\mu=1.2$ GeV. On the other hand, others have better convergence on some scale. The convergence range extends to lower values of $\lambda \approx 1$ GeV if we set $\mu=6$ GeV. This scale setting might be counter-intuitive since we are usually recommended that the renormalization scale μ should be taken at the scale of interest, $\mu \approx \lambda$. The convergence of the perturbations, however, depends on the quantity. For our case, $F(\lambda)$ has better convergence with the higher renormalization scale μ .

With the choice of $\mu=6$ GeV, the convergence is good up to the $\lambda = 0.8$ GeV. Since our lattice results are in $\lambda = 1.2$ GeV or slightly lower, we choose $\mu = 6$ GeV for the convergence.

¹¹ The reduction of uncertainty potentially suffer from enhancements of higher order term which comes from logarithmic term, $\sim \ln \lambda/\mu$.

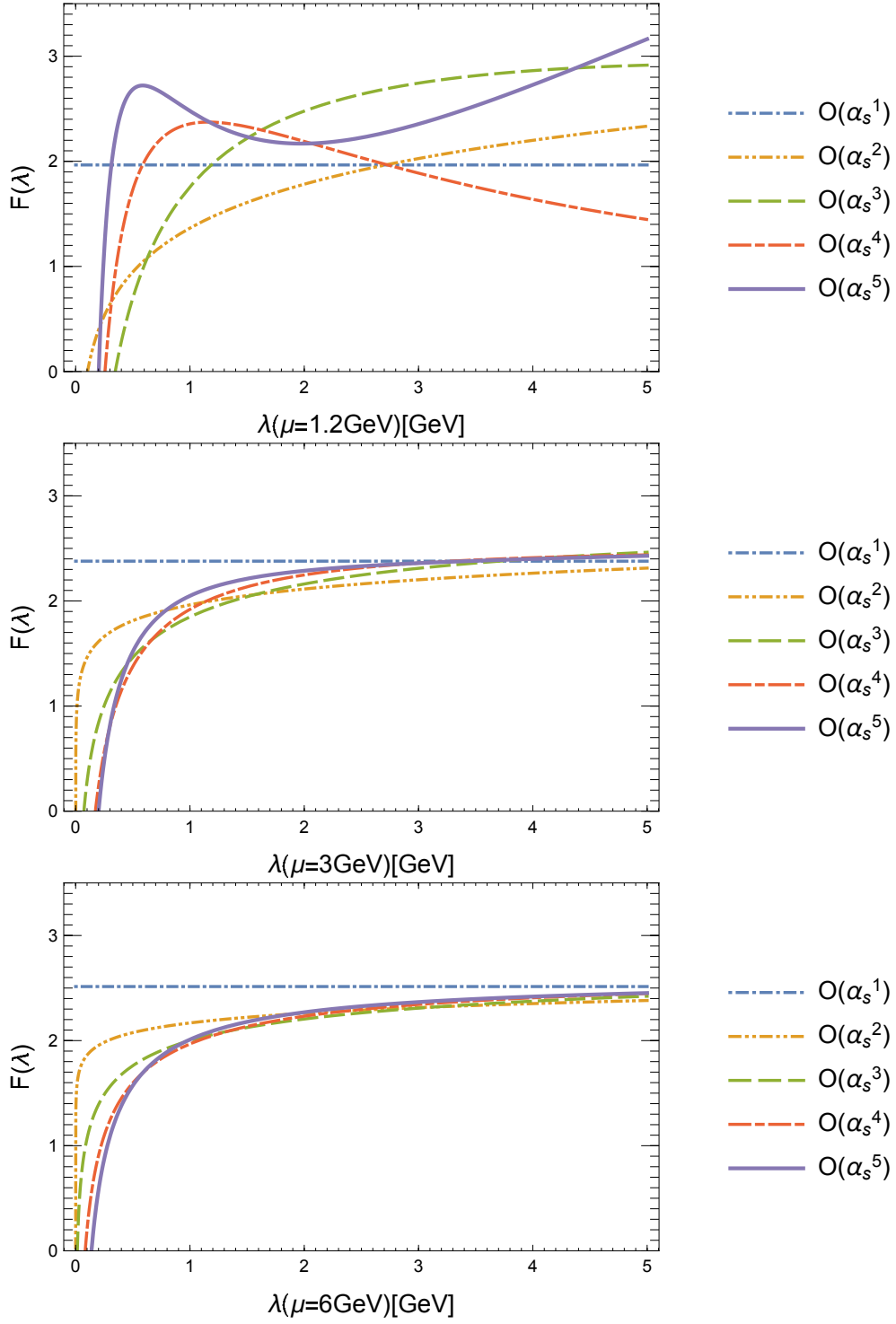


FIG. 13. The convergence of the exponent $F(\lambda)$ of the Dirac pectral density in $N_f = 3$ QCD are plotted. $\overline{\text{MS}}$ scheme at the renormalization scale μ is 1.2 GeV (upper panel), 3 GeV (middle) and 6 GeV (lower panel). Any perturbative order from $O(\alpha_s)$ to $O(\alpha_s^5)$ are shown. We set the unknown constant term $d_5 = 0$.

B. Perturbative formulae for Dirac spectral density

We summarize useful formulae for the Dirac spectral density in the perturbative expansion.

The definitions of the β -function and the mass anomalous dimension γ_m are given by [125, 126]

$$\beta(\mu) \equiv \frac{\partial \alpha_s}{\partial \ln \mu} = \beta_0 \alpha_s^2 + \beta_1 \alpha_s^3 + \beta_2 \alpha_s^4 + \beta_3 \alpha_s^5 + \beta_4 \alpha_s^6 + O(\alpha_s^7), \quad (\text{IV.20})$$

$$\gamma_m(\mu) \equiv -\frac{\partial \ln m(\mu)}{\partial \ln \mu} = \gamma_0 \alpha_s + \gamma_1 \alpha_s^2 + \gamma_2 \alpha_s^3 + \gamma_3 \alpha_s^4 + \gamma_4 \alpha_s^5 + O(\alpha_s^6). \quad (\text{IV.21})$$

Now, the coefficients are

$$\begin{aligned} \pi \beta_0 &= -5.5 + 0.333333n_f, \\ \pi^2 \beta_1 &= -12.75 + 1.583333n_f, \\ \pi^3 \beta_2 &= -44.6406 + 8.73785n_f - 0.188079n_f^2, \\ \pi^4 \beta_3 &= -228.461 + 54.2679n_f - 3.16476n_f^2 - 0.0117134n_f^3, \\ \pi^5 \beta_4 &= -1049.12 + 363.598n_f - 34.312n_f^2 + 0.451714n_f^3 + 0.00359858n_f^4, \end{aligned} \quad (\text{IV.22})$$

and

$$\begin{aligned} \pi \gamma_0 &= 2, \\ \pi^2 \gamma_1 &= 8.41667 - 0.277778n_f, \\ \pi^3 \gamma_2 &= 39.0313 - 4.56824n_f - 0.0540123n_f^2, \\ \pi^4 \gamma_3 &= 197.887 - 38.2149n_f + 0.552325n_f^2 + 0.0115864n_f^3, \\ \pi^5 \gamma_4 &= 1119.41 - 287.373n_f + 14.9648n_f^2 + 0.216637n_f^3 - 0.000170718n_f^4. \end{aligned} \quad (\text{IV.23})$$

We also show the coefficients of the spectral function $\rho(\lambda)$ with scale dependence,

$$\begin{aligned} -\frac{\rho_1}{\pi} &= c_1 - 4L_\lambda \gamma_0, \\ -\frac{\rho_2}{\pi^2} &= c_2 - 2L_\lambda^2 \gamma_0 [\beta_0 - 4\gamma_0] + L_\lambda [\beta_0 c_1 - 4(c_1 \gamma_0 - \gamma_0^2 + \gamma_1)], \\ -\frac{\rho_3}{\pi^3} &= c_3 - \frac{4}{3} L_\lambda^3 \gamma_0 [\beta_0^2 - 6\beta_0 \gamma_0 + 8\gamma_0^2] \\ &\quad + L_\lambda^2 [\beta_0^2 c_1 - 2\gamma_0(\beta_1 - 4c_1 \gamma_0 + 8\gamma_0^2 - 8\gamma_1) + \beta_0(-6c_1 \gamma_0 + 6\gamma_0^2 - 4\gamma_1)] \\ &\quad + L_\lambda [\beta_1 c_1 + \beta_0(2c_2 - c_1 \gamma_0) - 4(c_2 \gamma_0 - c_1 \gamma_0^2 + \gamma_0^3 + c_1 \gamma_1 - 2\gamma_0 \gamma_1 + \gamma_2)], \end{aligned}$$

$$\begin{aligned}
-\frac{\rho_4}{\pi^4} &= c_4 + \frac{1}{3}L_\lambda^4\gamma_0 [-3\beta_0^3 + 22\beta_0^2\gamma_0 - 48\beta_0\gamma_0^2 + 32\gamma_0^3] \\
&+ \frac{1}{3}L_\lambda^3 [3\beta_0^3c_1 - 2\beta_0^2(11c_1\gamma_0 - 11\gamma_0^2 + 6\gamma_1) + 2\beta_0\gamma_0(-5\beta_1 + 24c_1\gamma_0 - 48\gamma_0^2 + 36\gamma_1)] \\
&+ \frac{1}{3}L_\lambda^3 [8\gamma_0^2(3\beta_1 - 4(c_1\gamma_0 - 3\gamma_0^2 + 3\gamma_1))] \\
&+ L_\lambda^2 \left[\beta_0^2(3c_2 - 5c_1\gamma_0/2) + \frac{1}{2}\beta_0(5\beta_1c_1 - 4(5c_2\gamma_0 - 7c_1\gamma_0^2 + 6\gamma_0^3 + 4c_1\gamma_1 - 9\gamma_0\gamma_1 + 3\gamma_2)) \right] \\
&+ L_\lambda^2 [2(-\beta_2\gamma_0 + \beta_1(-3c_1\gamma_0 + 3\gamma_0^2 - 2\gamma_1))] \\
&+ L_\lambda^2 [8(c_2\gamma_0^2 - 2c_1\gamma_0^3 + 3\gamma_0^4 + 2c_1\gamma_0\gamma_1 - 6\gamma_0^2\gamma_1 + \gamma_1^2 + 2\gamma_0\gamma_2)] \\
&+ L_\lambda [\beta_2c_1 + 2\beta_1c_2 + 3\beta_0c_3 - \beta_1c_1\gamma_0 - 2\beta_0c_2\gamma_0 - 4c_3\gamma_0 + \beta_0c_1\gamma_0^2 + 4c_2\gamma_0^2 - 4c_1\gamma_0^3 + 4\gamma_0^4] \\
&+ L_\lambda [-\beta_0c_1\gamma_1 - 4c_2\gamma_1 + 8c_1\gamma_0\gamma_1 - 12\gamma_0^2\gamma_1 + 4\gamma_1^2 - 4c_1\gamma_2 + 8\gamma_0\gamma_2 - 4\gamma_3], \\
-\frac{\rho_5}{\pi^5} &= c_5 - \frac{4}{15}L_\lambda^5\gamma_0 [3\beta_0^4 - 25\beta_0^3\gamma_0 + 70\beta_0^2\gamma_0^2 - 80\beta_0\gamma_0^3 + 32\gamma_0^4] \\
&+ \frac{1}{3}L_\lambda^4 [3\beta_0^4c_1 + 4\beta_0\gamma_0^2(13\beta_1 - 20c_1\gamma_0 + 60\gamma_0^2 - 48\gamma_1)] \\
&+ \frac{1}{3}L_\lambda^4 [\beta_0^3(-25c_1\gamma_0 + 25\gamma_0^2 - 12\gamma_1) - 16\gamma_0^3(3\beta_1 - 2c_1\gamma_0 + 8\gamma_0^2 - 8\gamma_1)] \\
&+ \frac{1}{3}L_\lambda^4 [\beta_0^2\gamma_0(-13\beta_1 + 70c_1\gamma_0 - 140\gamma_0^2 + 88\gamma_1)] \\
&+ \frac{1}{3}L_\lambda^3 [\beta_0^3(12c_2 - 13c_1\gamma_0) + \beta_0^2(13\beta_1c_1 - 52c_2\gamma_0 + 88c_1\gamma_0^2 - 70\gamma_0^3 - 36c_1\gamma_1 + 88\gamma_0\gamma_1 - 24\gamma_2)] \\
&+ \frac{1}{3}L_\lambda^3 [-4\beta_0(3\beta_2\gamma_0 + \beta_1(13c_1\gamma_0 - 13\gamma_0^2 + 7\gamma_1))] \\
&+ \frac{1}{3}L_\lambda^3 [-4\beta_0(-6(3c_2\gamma_0^2 - 7c_1\gamma_0^3 + 10\gamma_0^4 + 5c_1\gamma_0\gamma_1 - 16\gamma_0^2\gamma_1 + 2\gamma_1^2 + 4\gamma_0\gamma_2))] \\
&+ \frac{1}{3}L_\lambda^3 [-2\gamma_0(3\beta_1^2 - 12\beta_1(2c_1\gamma_0 - 4\gamma_0^2 + 3\gamma_1))] \\
&+ \frac{1}{3}L_\lambda^3 [-2\gamma_0(4(-3\beta_2\gamma_0 + 4(c_2\gamma_0^2 + 3(-c_1\gamma_0^3 + 2\gamma_0^4 + c_1\gamma_0\gamma_1 - 4\gamma_0^2\gamma_1 + \gamma_1^2 + \gamma_0\gamma_2))))] \\
&+ L_\lambda^2 \left[\frac{3\beta_1^2c_1}{2} + \beta_0^2(6c_3 - 7c_2\gamma_0 + \frac{9c_1\gamma_0^2}{2} - 3c_1\gamma_1) \right] \\
&+ L_\lambda^2 [\beta_1(\beta_0(7c_2 - 6c_1\gamma_0) - 2(5c_2\gamma_0 - 7c_1\gamma_0^2 + 6\gamma_0^3 + 4c_1\gamma_1 - 9\gamma_0\gamma_1 + 3\gamma_2))] \\
&+ L_\lambda^2 [\beta_0(3\beta_2c_1 - 2(7c_3\gamma_0 - 11c_2\gamma_0^2))] \\
&+ L_\lambda^2 [-2\beta_0(+12c_1\gamma_0^3 - 10\gamma_0^4 + 6c_2\gamma_1 - 17c_1\gamma_0\gamma_1 + 24\gamma_0^2\gamma_1 - 6\gamma_1^2 + 5c_1\gamma_2 - 12\gamma_0\gamma_2 + 4\gamma_3)] \\
&+ L_\lambda^2 [-2(\beta_3\gamma_0 + \beta_2(3c_1\gamma_0 - 3\gamma_0^2 + 2\gamma_1) - 4(c_3\gamma_0^2 - 2c_2\gamma_0^3 + 3c_1\gamma_0^4 - 4\gamma_0^5 + 2c_2\gamma_0\gamma_1))] \\
&+ L_\lambda^2 [-2(-4(-6c_1\gamma_0^2\gamma_1 + 12\gamma_0^3\gamma_1 + c_1\gamma_1^2 - 6\gamma_0\gamma_1^2 + 2c_1\gamma_0\gamma_2 - 6\gamma_0^2\gamma_2 + 2\gamma_1\gamma_2 + 2\gamma_0\gamma_3))] \\
&+ L_\lambda [\beta_3c_1 + 2\beta_2c_2 + 3\beta_1c_3 + 4\beta_0c_4 - \beta_2c_1\gamma_0 - 2\beta_1c_2\gamma_0 - 3\beta_0c_3\gamma_0 - 4c_4\gamma_0 + \beta_1c_1\gamma_0^2 + 2\beta_0c_2\gamma_0^2] \\
&+ L_\lambda [4c_3\gamma_0^2 - \beta_0c_1\gamma_0^3 - 4c_2\gamma_0^3 + 4c_1\gamma_0^4 - 4\gamma_0^5 - \beta_1c_1\gamma_1 - 2\beta_0c_2\gamma_1 - 4c_3\gamma_1 + 2\beta_0c_1\gamma_0\gamma_1]
\end{aligned}$$

$$\begin{aligned}
& +L_\lambda [8c_2\gamma_0\gamma_1 - 12c_1\gamma_0^2\gamma_1 + 16\gamma_0^3\gamma_1 + 4c_1\gamma_1^2 - 12\gamma_0\gamma_1^2 - \beta_0c_1\gamma_2 - 4c_2\gamma_2 + 8c_1\gamma_0\gamma_2 - 12\gamma_0^2\gamma_2] \\
& +L_\lambda [8\gamma_1\gamma_2 - 4c_1\gamma_3 + 8\gamma_0\gamma_3 - 4\gamma_4], \tag{IV.24}
\end{aligned}$$

where $L_\lambda = \ln(\lambda/\mu)$, and the numerical coefficients are

$$\begin{aligned}
c_1 &= \frac{10}{3\pi}, \\
c_2 &= \frac{2203 - 234n_f - 324\pi^2 + 8n_f\pi^2 - 48\zeta_3}{72\pi^2}, \\
c_3 &= \begin{cases} -5.98134 & (n_f = 3) \\ -5.90468 & (n_f = 2) \end{cases}. \tag{IV.25}
\end{aligned}$$

C. Discretization effects with lattice domain-wall fermion

The Dirac eigenvalue spectrum in 1 GeV or higher can contain sizable discretization error since our lattice spacings are in $1/a = 2.4\text{--}4.6$ GeV. We investigate the size of lattice artifacts in the Dirac spectral density at the free field limit. Since our lattice calculation is done using domain-wall fermion formulation [37, 38], we mainly analyze the lattice artifacts of the domain-wall fermion.

The Möbius generalization of the domain-wall fermion [41] provides the Dirac operator as

$$aD_{\text{ov}}(m_f, m_{\text{PV}}) \equiv (2 - cM_0) M_0 a m_{\text{PV}} [\mathcal{P}^{-1} D_{\text{DW}}^{-1}(m_{\text{PV}}) D_{\text{DW}}(m_f) \mathcal{P}]_{11}, \tag{IV.26}$$

where $D_{\text{DW}}(m_f)$ is the five-dimensional Dirac operator with a fermion mass m_f . As we discussed in Section II, the dimensionless parameters c and M_0 are in the kernel operator. The definition contains 5D Dirac operator with a heavier Pauli-Villars mass to eliminate the unphysical bulk mode in the 5D with respect the exponential locality. We usually set the Pauli-Villars mass m_{PV} to be $1/a$. The details of this definition are in the Section II and [41, 127]. Equation (IV.26) can represent the overlap operator as

$$aD_{\text{ov}}(m_f, m_{\text{PV}}) = (2 - cM_0) M_0 a m_{\text{PV}} \frac{(1 + am_f) + (1 - am_f)\gamma_5 \text{sgn}(\gamma_5 a D_M)}{(1 + am_{\text{PV}}) + (1 - am_{\text{PV}})\gamma_5 \text{sgn}(\gamma_5 a D_M)}, \tag{IV.27}$$

in the limit of $L_s \rightarrow \infty$. The conventional choice is $am_{\text{PV}} = 1$. Here, the Möbius kernel operator D_M is

$$aD_M = \frac{baD_W}{2 + caD_W}, \tag{IV.28}$$

in terms of the Wilson-Dirac operator D_W with dimensionless parameter b . In our work, we take $M_0 = 1$ and $c = 1$. Since the choice of b does not contribute to the Dirac eigenvalue in the tree level, we do not need to take b at the typical value.

As shown in Section II, the general form of the 4D overlap operator (IV.27) still holds the Ginsparg-Wilson relation and the exponential locality. In this work, we use $am_{\text{PV}} = 1$ in the simulation and reinterpret our results to the case of $am_{\text{PV}} \neq 1$ for valence quarks.

We calculate the eigenvalues of $a^2 D_{\text{ov}}^\dagger(m_f, m_{\text{PV}}) D_{\text{ov}}(m_f, m_{\text{PV}})$ in the massless limit, $m_f = 0$. We denote the corresponding eigenvalue as $a^2 \lambda^2(am_{\text{PV}})$. Since any $a^2 D_{\text{ov}}^\dagger D_{\text{ov}}$ of am_{PV} commute with each other, we find the relation of their eigenvalues as

$$a^2 \lambda^2(am_{\text{PV}}) = \frac{a^2 \lambda^2(1)}{1 + \left(\frac{1}{a^2 m_{\text{PV}}^2} - 1 \right) \frac{a^2 \lambda^2(1)}{(2 - (b - c)M_0)^2 M_0^2}}. \quad (\text{IV.29})$$

The projection from eigenvalue to the imaginary axis can be represented as the limit $am_{\text{PV}} \rightarrow \infty$, which is utilized in [15, 115, 116].

We calculate the eigenvalue $a^2 \lambda^2$ with given four-momentum ap_μ for plane wave states at tree-level. We count the number of states in an eigenvalue interval $[a^2 \lambda^2, a^2(\lambda \pm \delta\lambda)^2]$ with random momenta ap_μ . The sampling number is $\sim 10^{12}$ to ignore the statistical error with our choice of bin size $a\delta\lambda = 0.0025$.

We show results of domain-wall fermions with different Pauli-Villars masses and Wilson fermion in Figure 14. Any formulations are consistent with the continuum limit at the lower eigenvalue regime which is below $a\lambda \simeq 0.3$. On the other hand, the spectral density of the domain-wall fermion with $am_{\text{PV}} = 1$ overshoots the continuum curve. We can understand this discrepancy as the cut-off effects of the Pauli-Villars mass. When the Pauli-Villars mass is set to 1, the maximum of the eigenvalue is also 1. It means that the eigenvalue becomes dense around $\lambda \sim 1$. This property holds to any Pauli-Villars mass $am_{\text{PV}} > 1$; the maximum of the eigenvalue is the same as the Pauli-Villars mass¹². The spectral densities for $am_{\text{PV}} = 3$ and ∞ are consistent with that of the continuum theory up to $a\lambda \sim 0.5$ – 0.6 . We remark that the Wilson fermions also match to the continuum up to the same region.

We now consider the exponent of the spectral density $F(\lambda)$ (IV.10). We use the symmetric difference as an $O(\delta\lambda^2)$ approximation of the difference,

$$\frac{\partial \rho}{\partial \lambda} \simeq \frac{\rho(\lambda + \delta\lambda) - \rho(\lambda - \delta\lambda)}{2\delta\lambda}. \quad (\text{IV.30})$$

¹² This holds when we set parameters $b - c = M_0 = 1$

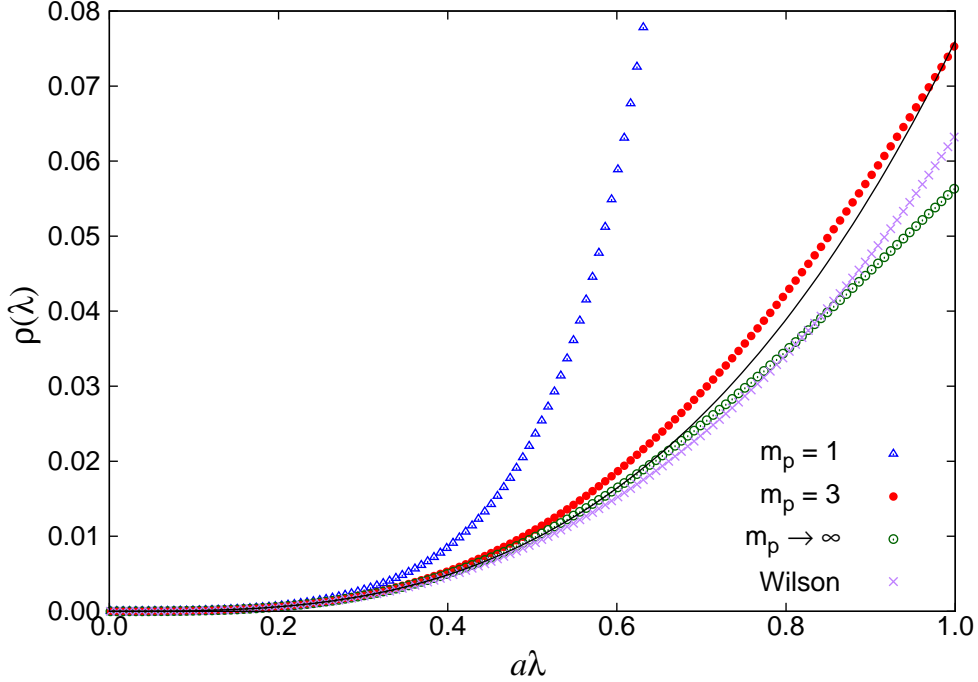


FIG. 14. Tree-level $\rho(\lambda)$ are plotted. We show $am_{\text{PV}} = 1$ (triangles), $am_{\text{PV}} = 3$ (filled circles), $am_{\text{PV}} \rightarrow \infty$ (open circles), and for Wilson fermion (crosses). The black solid line is $\rho(\lambda) = 3\lambda^3/4\pi^2$ as a continuum result.

The leading error for $F(\lambda)$ is $2\delta\lambda^2/\lambda^2$. We focus on $\delta\lambda/\lambda < 0.07$ to take the uncertainty is below 0.01. The reliable range is $a\lambda > 0.07$ with our choice of $a\delta\lambda = 0.005$.

The tree level exponent $F_0(\lambda)$ with bin size $a\delta\lambda = 0.005$ are shown in Figure 15. In the continuum limit, it should be a constant, *i.e.*, 3. The results of continuum theory with the same finite difference (IV.30) have some deviation from 3 near $a\lambda = 0$ (black dots). This deviation originated from the approximation of the derivative. Since we do not use the points below $a\lambda < 0.025$, the discretization uncertainty from this approximation is negligible.

The discretization effects of the spectral density are magnified in its exponent. There is a significant deviation for $am_{\text{PV}} = 1$ from the continuum theory below $a\lambda \sim 0.1$. The generalization of the Pauli-Villars mass reduces the discretization effect. We investigate the discretization effect using numerical approximation by a polynomial in $(a\lambda)^2$,

$$\begin{aligned}
 F_0(\lambda) &= 3 + 6.93(a\lambda)^2 + 2.08(a\lambda)^4 - 13.0(a\lambda)^6 + 24.9(a\lambda)^8 & (am_{\text{PV}} = 1), \\
 F_0(\lambda) &= 3 + 1.59(a\lambda)^2 - 6.58(a\lambda)^4 + 6.95(a\lambda)^6 - 2.51(a\lambda)^8 & (am_{\text{PV}} = 3). \quad (\text{IV.31})
 \end{aligned}$$

The approximation is valid for $a\lambda < 0.6$. We find the suppression of the discretization error

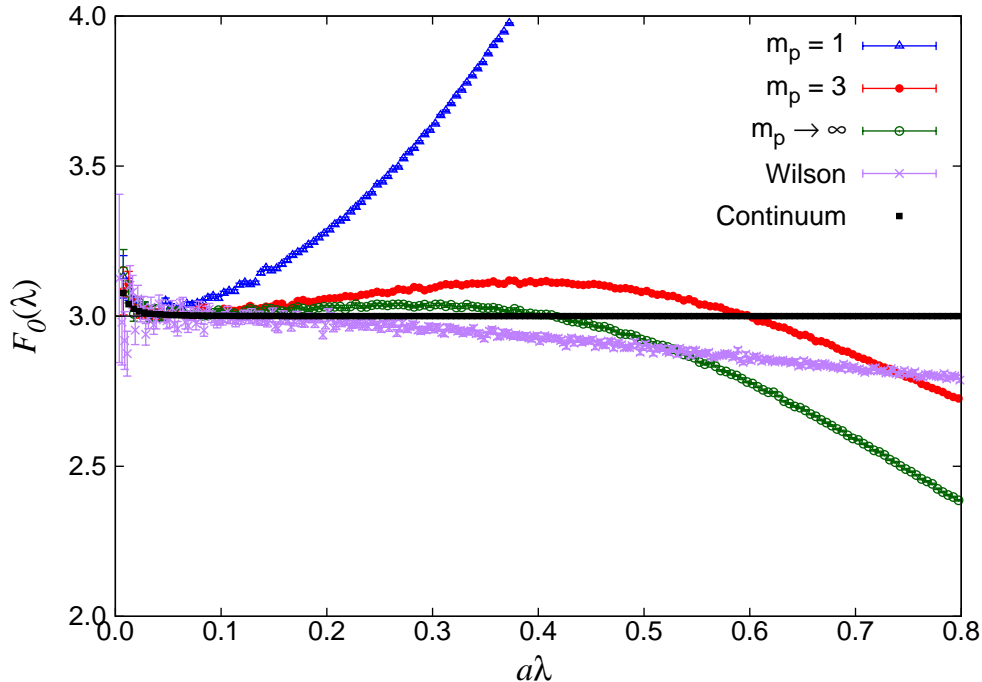


FIG. 15. Tree-level exponent of the Dirac spectral density $F(\lambda) = \partial\rho(\lambda)/\partial\lambda$ of the domain-wall fermion with $am_{PV} = 1$ (triangles), $am_{PV} = 3$ (filled circles), and $am_{PV} \rightarrow \infty$ (open circles) are shown. We also show that of the Wilson fermion (crosses). We set the bin size $a\delta\lambda = 0.005$. To show the size of uncertainty from the finite bin size, The numerical derivative of the free field spectral density, $\sim \lambda^3$, is also represented (black dots).

as the small coefficients for $am_{PV} = 3$.

We analyze the lattice data with $am_{PV} = 3$. Namely, we translate our lattice calculation of $\lambda(am_{PV} = 1)$ to $\lambda(am_{PV} = 3)$ using (IV.29). We use the parametrization (IV.31) to further correction multiplying by $3/F_0(\lambda)$. This procedure eliminates the leading discretization error. After all, we take the continuum limit with the assumption that the remaining discretization effects are linear in a^2 .

Strictly speaking, the different choice of sea and valence fermion formulation is a partially quenched theory. However, since the correspondence is one-to-one even in the interacting case, the results are the same after taking the continuum limit. We find this correspondence explicitly in (IV.29) as $a^2\lambda^2(am_{PV}) = a^2\lambda^2(1) + O(a^4\lambda^4(1))$. We only utilize the small $a\lambda(1)$ regime, the corresponding $a\lambda(am_{PV})$ are reliable in the continuum.

One might have concern about the validity of the formulation with $am_{PV} \neq 1$. As we described in Section II with the formulations of domain-wall fermion, the locality and

β	a^{-1}	$L^3 \times T(\times L_s)$	#meas	am_{ud}	am_s	m_π	$m_\pi L$
	[GeV]					[MeV]	
4.17	2.453(4)	$32^3 \times 64(\times 12)$	100	0.0035	0.040	230(1)	3.0
				0.007	0.030	310(1)	4.0
				0.007	0.040	309(1)	4.0
				0.012	0.030	397(1)	5.2
				0.012	0.040	399(1)	5.2
				0.019	0.030	498(1)	6.5
				0.019	0.040	499(1)	6.5
		$48^3 \times 96(\times 12)$	100	0.0035	0.040	226(1)	4.4
4.35	3.610(9)	$48^3 \times 96(\times 8)$	50	0.0042	0.0180	296(1)	3.9
				0.0042	0.0250	300(1)	3.9
				0.0080	0.0180	407(1)	5.4
				0.0080	0.0250	408(1)	5.4
				0.0120	0.0180	499(1)	6.6
				0.0120	0.0250	501(1)	6.6
4.47	4.496(9)	$64^3 \times 128(\times 8)$	39	0.0030	0.015	284(1)	4.0

TABLE XIII. Lattice ensembles used in this section.

chirality still hold for finite am_{PV} .

We also show the result for Wilson fermion by crosses, and the results have a smooth and mild slope. Its polynomial approximation is

$$F_0(\lambda) = 3 - 0.459(a\lambda)^2 + 0.208(a\lambda)^4 \quad (\text{Wilson}), \quad (\text{IV.32})$$

and the coefficient of $O(a^2)$ term is even smaller than that for the domain-wall fermion $am_{\text{PV}} = 3$ or ∞ .

D. Lattice calculation

1. Lattice ensembles

Our lattice QCD simulation is again performed with flavors of dynamical quarks. The parameter choice is the same as in Table in Section III except for the number of measurements. In this work, the finite volume effect and the sea quark mass dependence of the spectral density are negligible in the high-energy region. We only count the number of eigenvalues of massless Dirac operator for valence quarks. “#meas” in the Table is 39–100 depending on the ensemble.

For the renormalization of the Dirac eigenvalue, we use the constants $Z_m(2 \text{ GeV}) = Z_S^{-1}(2 \text{ GeV})$,

$$\lambda^{\overline{\text{MS}}}(2 \text{ GeV}) = Z_m(2 \text{ GeV})\lambda. \quad (\text{IV.33})$$

The numerical values are $Z_S(2 \text{ GeV}) = 1.0372(145)$ at $\beta = 4.17$, $0.9342(87)$ at $\beta = 4.35$, and $0.8926(67)$ at $\beta = 4.47$. We quote the uncertainty as for the summation of statistical and systematic errors in quadrature. The renormalization constants are also used for renormalization of the spectral density. However, the renormalization is implicitly done when we calculate the eigenvalue spectral density by dividing the number of eigenvalues in a bin of λ by the corresponding bin size. As we discussed in the subsection IV C, we shift the scale from 2 GeV to 6 GeV in order to get more convergent perturbative expansions.

2. Stochastic calculation of the spectral density

We use the stochastic estimator to calculate the Dirac eigenvalue density. The details are described in [15], and see [128] as a related work. We provide a brief review in this section.

We introduce a filtering function $h(x)$ which is equal to 1 in a range $[v, w]$ and is zero elsewhere. The stochastic procedure estimates the number of eigenvalues of a Hermitian matrix A in a range $[v, w]$ as

$$n[v, w] \simeq \frac{1}{N} \sum_{k=1}^N \langle \xi_k h(A) \xi_k \rangle. \quad (\text{IV.34})$$

The number of normalized random noise vectors ξ_k is N . For numerical calculation, we

approximate the filtering function by the Chebyshev polynomial $T_j(x)$ through

$$h(x) \simeq \sum_{j=0}^p \gamma_j T_j(x) \quad (\text{IV.35})$$

where constants γ_j depends on v and w . This approximation is only valid in the range $-1 \leq x \leq 1$. We also introduce another factor g_j^p for stabilization. We calculate the chebyshev polynomial using a recursion relation: $T_0(x) = 1$, $T_1(x) = x$, and $T_j(x) = 2xT_{j-1}(x) - T_{j-2}(x)$. The polynomial is constructed by order $p = 8,000\text{--}16,000$.

We calculate the mode number $n[v, w]$,

$$n[v, w] \simeq \frac{1}{N} \sum_{k=1}^N \sum_{j=0}^p g_j^p \gamma_j \langle \xi_k^\dagger T_j(A) \xi_k \rangle. \quad (\text{IV.36})$$

We note that the $\langle \xi_k^\dagger T_j(A) \xi_k \rangle$ is independent of the sampling range $[v, w]$. Once we calculate the inner products $\langle \xi_k^\dagger T_j(A) \xi_k \rangle$ for all j with upper limit p , we can estimate $n[v, w]$ for arbitrary $[v, w]$ using the known factors $g_j^p \gamma_j$. This estimation calculates the whole spectrum from $\lambda = 0$ to the lattice cut-off scale.

For calculation of the Dirac eigenvalue density, we define the hermitian operator $A = 2a^2 D_{\text{ov}}(m_f, 1)^\dagger D_{\text{ov}}(m_f, 1) - 1$, whose range is $[-1, +1]$. We define the range as $v = 2a^2(\lambda - \delta/2)^2 - 1$ and $w = 2a^2(\lambda + \delta/2)^2 - 1$ with the bin size δ . The spectral function at λ is obtained by

$$a^3 \rho(\lambda) = \frac{1}{2V/a^4} \frac{n[v, w]}{a\delta}. \quad (\text{IV.37})$$

As we discussed above, the systematic error from the finite bin size is taken into account when we get the derivative of the spectral density. The finiteness of the Chebyshev polynomial also provides uncertainty. Although smaller bin sizes enhance this error, we confirm that this uncertainty is much smaller than the statistical error with our choice of bin size.

E. Lattice results for the spectral function and its exponent

We calculate the spectral density $\rho(\lambda)$ as summarized in Table XIII. For each configuration, we introduce one noise vector. Our results are in the $\overline{\text{MS}}$ scheme. First, we calculate the spectral density at $\mu = 2$ GeV and translate it to 6 GeV. After the transformation, we match our result with the perturbative series. We chose the bin size $\delta = 0.05$ GeV in physical

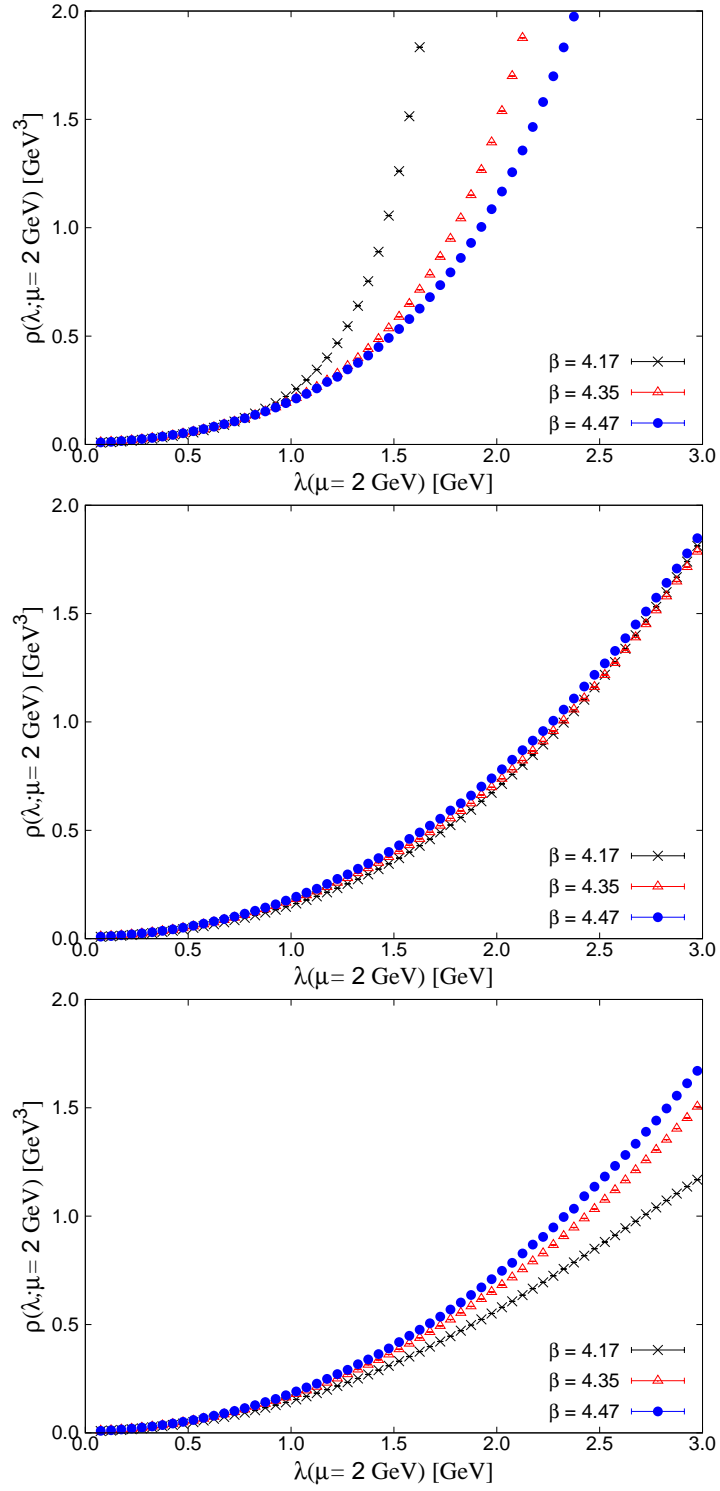


FIG. 16. Dirac spectral density $\rho(\lambda)$ as a function of $\lambda(\mu = 2 \text{ GeV})$ with $am_{PV} = 1$ (top panel), $am_{PV} = 3$ (middle), and $am_{PV} \rightarrow \infty$ (bottom). Each lattice spacings $\beta = 4.17$ (crosses), $\beta = 4.35$ (triangles) and $\beta = 4.47$ (circles) are plotted. each points are mean value of different sea quark masses.

units for the scale of 2 GeV. With this bin size, the truncation of the Chebyshev polynomial does not contribute to the uncertainty.

Figure 16 shows the Dirac spectral density at each β with different Pauli-Villars masses. Since there is only negligible dependence on the sea quark mass, we average over the ensembles with different sea quark masses. As we discussed for tree-level, the low-lying Dirac eigenvalue region $\lambda \leq 0.5$ GeV is sufficiently independent of the lattice spacings. Besides, relatively higher Dirac eigenvalue spectral density suffers from the discretization effects, and part of this contribution is reduced by introducing the generalized Pauli-Villars mass $am_{\text{PV}} = 3$ and $am_{\text{PV}} \rightarrow \infty$. The results are almost an analog of discussion in the subsection IV C.

As we described in the subsections IV A and IV C, we utilize the exponent of the Dirac eigenvalue spectral density, $F(\lambda)$. We perform the numerical approximation of the derivative using (IV.30). The systematic error from the discretized derivative is about 0.008 (0.3%) at the eigenvalue scale $\lambda_{\text{min}} = 0.8$ GeV with the choice of bin size $\delta\lambda = 0.05$ GeV. This contribution is smaller than that from statistical fluctuations.

The exponent $F(\lambda)$ at each lattice spacing is plotted in Figure 17. We set the renormalization scale $\mu = 6$ GeV. The leading discretization effects are eliminated by the multiplying the factor $3/F_0(\lambda)$ from (IV.31). Our finding is the standard Pauli-Villars mass domain-wall fermion has strong discretization effects even after the correction by the factor $3/F_0(\lambda)$, as shown in the top panel ($am_{\text{PV}} = 1$). The Pauli-Villars mass generalization improves the uncertainty as one can see in the middle and bottom panel ($am_{\text{PV}} = 3$ and $am_{\text{PV}} \rightarrow \infty$). Gray symbols of the data points are $a\lambda > 0.5$, which has significant discretization effects even after the correction.

We also show results at each order perturbative calculation from $O(\alpha_s)$ to $O(\alpha_s^5)$. The input value of the strong coupling constant for this plot is taken from the world average $\Lambda_{\text{QCD}}^{(3)} = 332(17)$ MeV for three-flavor QCD [129]. We set the unknown fifth-order constant to be $d_5 = 0$ as a representative value. We transform the lattice results from $\mu = 2$ GeV to 6 GeV by the renormalization group equation with the same value of the strong coupling constant. The consistency between our lattice calculation with $am_{\text{PV}} = 3$ (middle panel) and the perturbative estimate can be seen except gray points.

In order to compare our lattice results with perturbative calculations more precisely, we extrapolate the lattice data for the exponent $F(\lambda)$ to the continuum limit. We assume

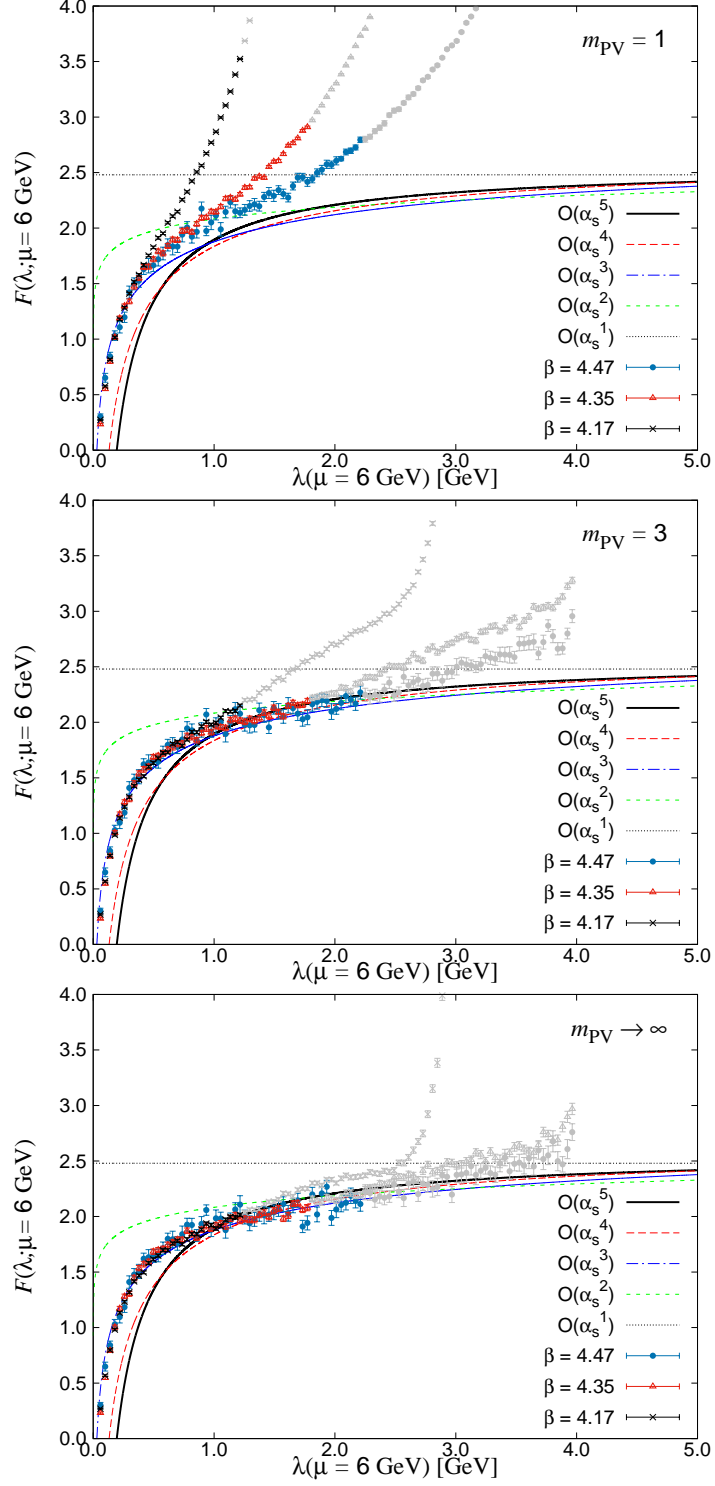


FIG. 17. Exponent of the Dirac spectral density $F(\lambda)$ with the Pauli-Villars mass $am_{\text{PV}} = 1$ (top), $m_{\text{PV}} = 3$ (middle), and $am_{\text{PV}} \rightarrow \infty$ (bottom) are shown. We set the renormalization scale $\mu = 6 \text{ GeV}$. We show the data at $\beta = 4.17$ (crosses), 4.35 (triangle) and 4.47 (dots). Grayed data points are $a\lambda > 0.5$. Lines represent results from each order of perturbative expansion.

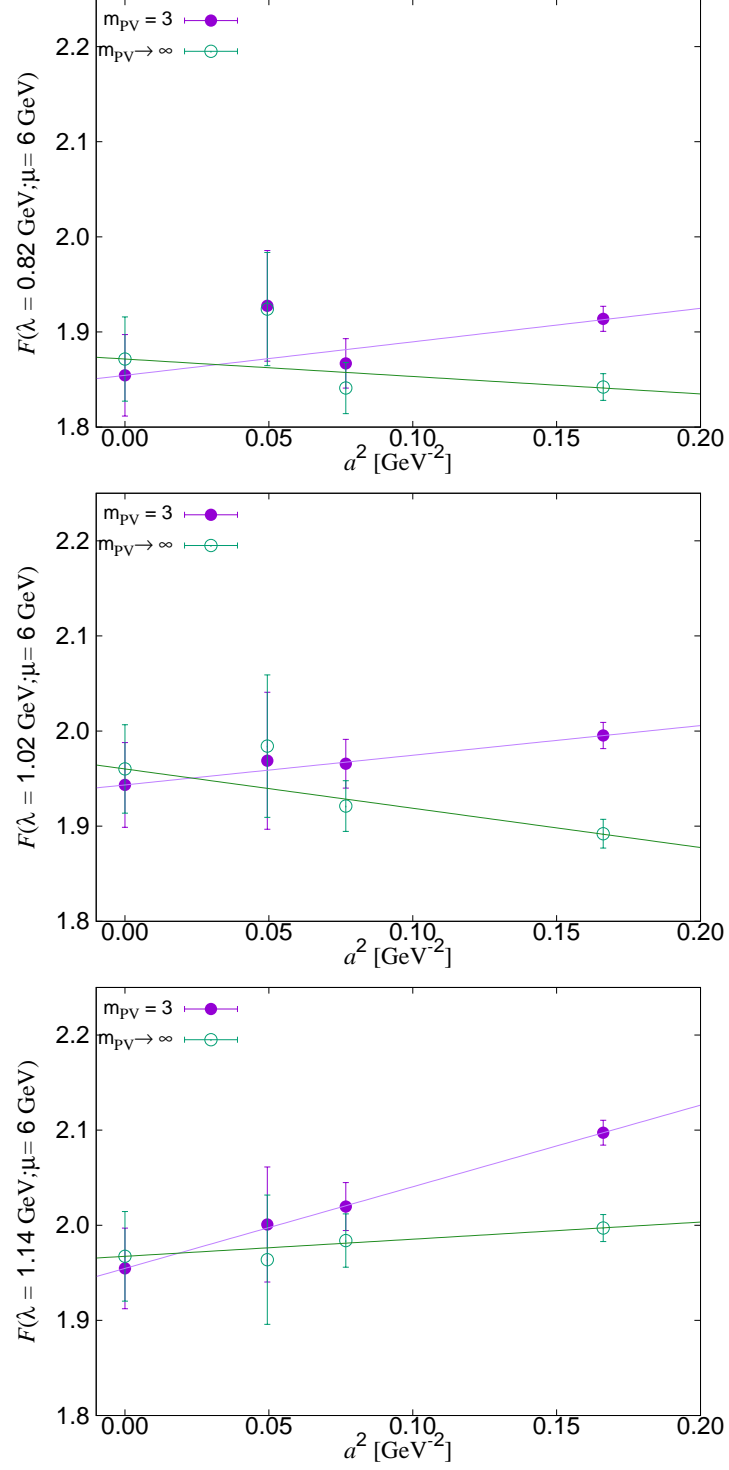


FIG. 18. Exponents $F(\lambda)$ at $\lambda = 0.82$ GeV (top panel) 1.02 GeV (middle), 1.14 GeV (bottom) in the continuum limit. The results with $am_{PV} = 3$ (circles) and with $am_{PV} \rightarrow \infty$ (crosses) as a function of a^2 [GeV⁻²] are plotted.

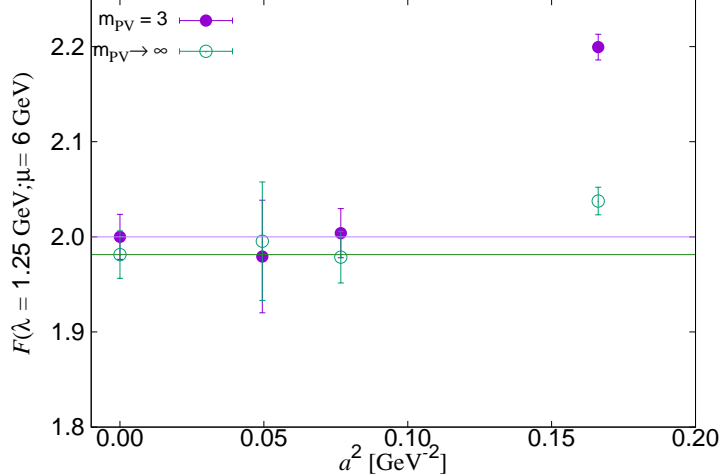


FIG. 19. Exponents $F(\lambda)$ at $\lambda = 1.25$ GeV in the continuum limit. Results with $m_{PV} = 3$ (circles) and with $m_{PV} \rightarrow \infty$ (crosses) as a function of a^2 [GeV $^{-2}$] are plotted.

a linear dependence in a^2 for the data at $am_{PV} = 3$ and $am_{PV} \rightarrow \infty$. Figures 18 and 19 show the extrapolation for some representative values of λ . The condition $a\lambda < 0.5$ is satisfied for all three lattice spacings when we focus on the eigenvalue at $\lambda = 1.22$ GeV or below. For this sufficiently small eigenvalue region, the remaining a^2 dependence is under control as one can see in Figure 18. The extrapolated value of $am_{PV} = 3$ and $am_{PV} \rightarrow \infty$ agrees with each other with small slope in a^2 . The results are consistent with our naive expectation: remaining discretization effects are naive $O(\alpha_s a^2 \lambda^2)$, which is about 5%. After the extrapolation, the uncertainty is much smaller.

The coarsest lattice does not satisfy the condition $a\lambda < 0.5$ in the eigenvalue region above $\lambda \simeq 1.22$ GeV. We extrapolate the data without the coarsest lattice assuming no dependence on a^2 , *i.e.*, we take a weighted average for the extrapolation. We show an example at the $\lambda = 1.25$ GeV and the extrapolated value is consistent with each other in Figure 19. The large discretization error at the coarsest lattice spacing can be seen at around $a^2 = 0.16$ GeV $^{-2}$ as the deviation from the straight lines.

Exponents $F(\lambda)$ in the continuum limit is shown in Figure 20. The results from $am_{PV} = 3$ are plotted. We plot an extrapolation using three lattice spacings (filled circles), two lattice spacings (open circles), and those of the finest lattice (green triangles). Since we set the condition $a\lambda < 0.5$, the highest eigenvalue is 2.2 GeV.

Perturbative results are also drawn with various orders from $O(\alpha_s)$ (dotted line) to $O(\alpha_s^5)$ (thin solid curve) with unknown coefficient d_5 in (IV.17) set to zero. Our lattice results

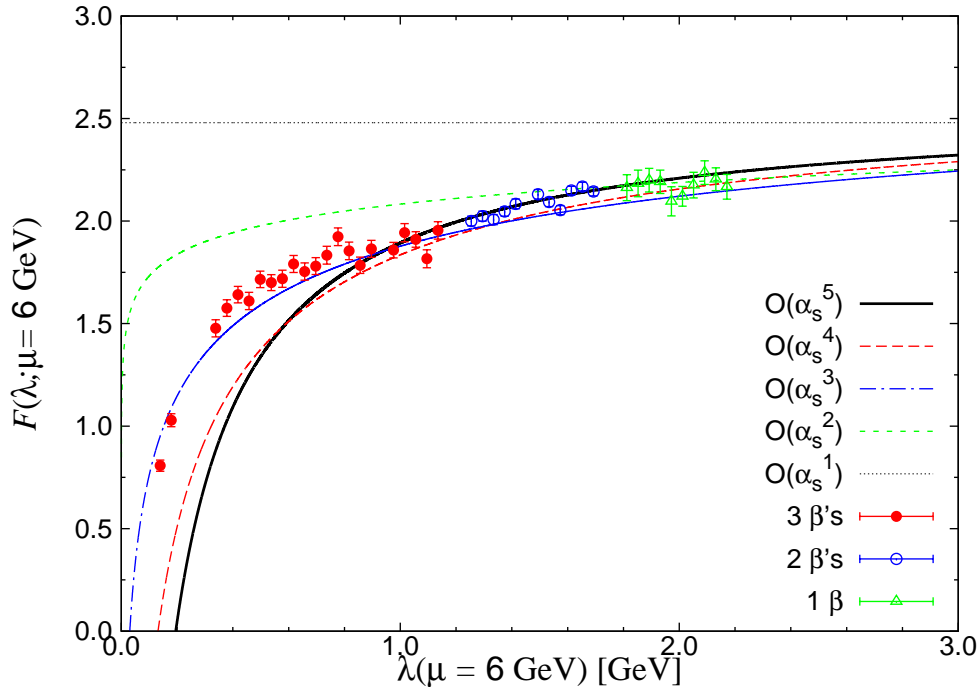


FIG. 20. Exponent of the Dirac spectral density $F(\lambda)$ as a function of $\lambda(\mu = 6 \text{ GeV})$ for Pauli-Villars mass $am_{\text{PV}} = 3$. We plot extrapolation using three lattice spacings (filled circles), two lattice spacings (open circles), and those of the finest lattice (green triangles). Perturbative results are also drawn with various orders from $O(\alpha_s)$ (dotted line) to $O(\alpha_s^5)$ (thin solid curve).

agree with the perturbative calculation with the input $\alpha_s(6 \text{ GeV}) = 0.191$ in the range $\lambda \simeq 0.8 \text{ GeV}$ and 2.2 GeV . This consistency suggests that our lattice calculation can extract the numerical value of the strong coupling constant $\alpha_s(6 \text{ GeV})$ without loss of the agreement with the world average.

In order to compare the perturbative expansion with the lattice data, we should pay attention to the non-perturbative effect. The non-perturbative contribution can be a power correction to the spectral function. The general form of the operator product expansion (OPE) tells us that the spectral function $\rho(\lambda)$ has a correction from $\sim \langle \bar{\psi}\psi \rangle$ at the first non-trivial order. Since the leading order contribution is $\sim \lambda^3$, the power correction is relatively suppressed. The Banks-Casher relation supports this suppression although it is valid in the limit of $\lambda \rightarrow 0$. In any case, the power correction which is represented as a constant in $\rho(\lambda)$ does not contribute to the exponent $F(\lambda)$. Namely, the power correction to the exponent $F(\lambda)$ is highly suppressed. Figure 20 shows the lattice QCD results, and also supports this suppression.

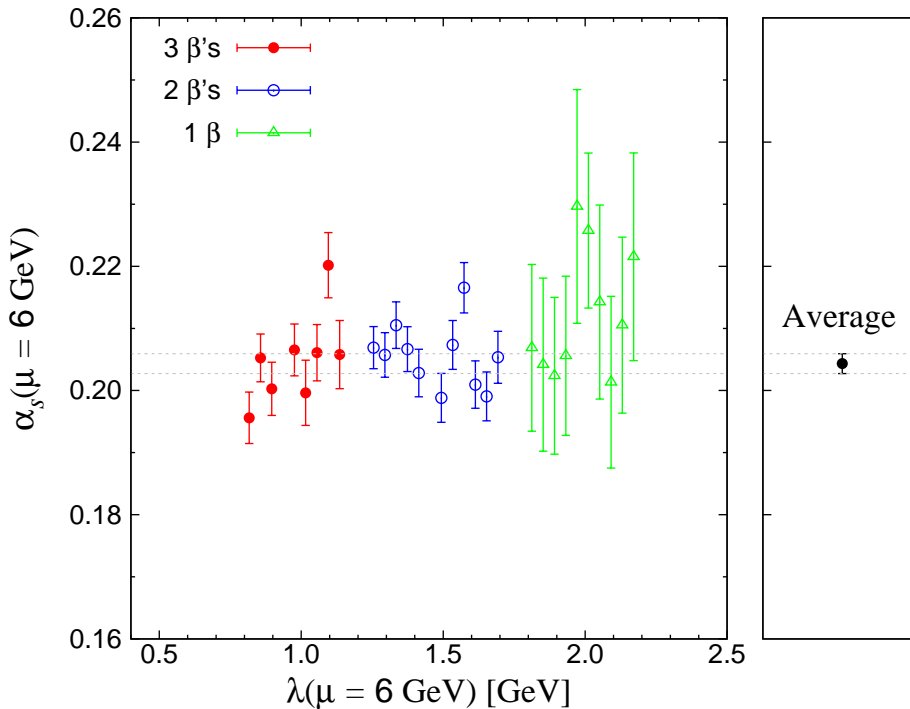


FIG. 21. Strong coupling constant $\alpha_s(\mu = 6 \text{ GeV})$ extracted from the exponent $F(\lambda)$ of the Dirac spectral function $\rho(\lambda)$.

F. Extraction of α_s

We attempt to extract the strong coupling constant α_s by the lattice results. The perturbative series for the exponent $F(\lambda)$ is known up to order α_s^4 as well as an estimate for the $O(\alpha_s^5)$ term as explicitly shown in (IV.11)-(IV.16). We solve the equation for the strong coupling constant at the renormalization scale $\mu = 6 \text{ GeV}$ with an input $F(\lambda)$ on the right-hand side. The uncertainty originated from the unknown parameter in the fifth-order is estimated below.

We can determine $\alpha_s(6 \text{ GeV})$ for each bin of λ by solving the equation (IV.11) as plotted in Figure 21. There is only tiny dependence on λ for $\alpha_s(6 \text{ GeV})$ in the eigenvalue region $\lambda \simeq 0.8 \text{ GeV}$ or higher. This is consistent with Figure 20, which shows that the results of the perturbative calculation agree with our lattice data down to $\lambda \simeq 0.8 \text{ GeV}$. The statistical error becomes larger in $\lambda > 1.8 \text{ GeV}$ since the lattice results are solely from the data of the finest lattice spacing ($\beta = 4.47$). The average from the bins between $\lambda = 0.8$ and 1.25 GeV is taken as our final result since the extrapolations are performed with the data for all three lattice spacings. On the right panel in Figure 21, we plot the statistically averaged value

$\alpha_s(6 \text{ GeV}) = 0.204(2)$. In the following, we estimate the possible systematic error since the above value only contains the statistical error.

The continuum extrapolation well controls the leading discretization effects. We estimate the remaining discretization effects from the result with Pauli-Villars masses $am_{\text{PV}} = 3$ and ∞ . We estimate the error for $\alpha_s(6 \text{ GeV})$ as ± 0.003 from the difference between these two calculations.

We also estimate the discretization error by the difference between the extrapolation with three and two points of data. We attempt to fit the data without points from coarsest lattice spacings. The deviation from the extrapolated value from three lattice points is an estimate of the systematic error. The estimate numerically leads the systematic error ± 0.006 for $\alpha_s(6 \text{ GeV})$. For a conservative estimate, we combine these estimates in quadrature. The estimate is ± 0.007 .

As we discussed in the subsection IV A, the perturbative error is estimated by varying ± 50 for d_5 of the $O(\alpha_s^5)$ term. This estimate leads an uncertainty of ± 0.012 for $F(\lambda)$ and propagate to $\alpha_s(6 \text{ GeV})$, ± 0.002 . We also consider another contribution from unknown $O(\alpha_s^6)$ term. This adds ± 0.052 for $F(\lambda)$ and ± 0.007 for $\alpha_s(6 \text{ GeV})$. Therefore we find that the perturbative uncertainty for $\alpha_s(6 \text{ GeV})$ is ± 0.007 .

The uncertainty due to the scale setting contributes as an overall shift of the physical scale. For $\alpha_s(6 \text{ GeV})$, this is a shift of the QCD scale Λ_{QCD} . We use leading scale dependence $\alpha_s(\mu) \simeq (-2\beta_0 \ln(\mu^2/\Lambda_{\text{QCD}}^2))^{-1}$ to estimate the error. The relative uncertainty 1.7% for the input value of t_0 becomes ± 0.001 for $\alpha_s(6 \text{ GeV})$. Also, the error from the renormalization constant $Z_S(2 \text{ GeV})$ causes an overall shift of the eigenvalue. The relative uncertainty is 1.5% for the constant $Z_S(2 \text{ GeV})$ which becomes ± 0.001 for $\alpha_s(6 \text{ GeV})$.

The summarized values of uncertainties are in Table XIV. We estimate the total error by averaging them in quadrature. The result is $\alpha_s(6 \text{ GeV}) = 0.204(10)$. Our estimate shows the dominant part of the uncertainty is discretization effects and the truncation of the perturbative expansion.

We convert the result to the value at the Z boson mass scale by using the four-loop β function. The threshold effect is taken into account in order to transform the results of four flavors result in those of five flavors. We obtain $\alpha_s^{(5)}(M_Z) = 0.1226(36)$ as a numerical result. It can be compared to the average of the lattice results 0.1182(12) [5] (the original works contributing to this average are [7, 8, 130–132]) as well as the world average which is

statistical	± 0.002
discretization	± 0.007
perturbative	± 0.007
lattice scale	± 0.001
renormalization	± 0.001
total	± 0.010

TABLE XIV. Estimated error for the determination of $\alpha_s(6 \text{ GeV})$ from the spectral density.

shown in the Particle Data Group, 0.1181(11) [129]. Our final result is slightly larger but consistent within about one standard deviation. Compared to our result, 0.1177(26) from the Section III, the present result is higher by about 1.1 standard deviations.

G. Summary

In this section, we provide a lattice calculation of the Dirac spectral density in QCD by the stochastic method to estimate the number of eigenvalues. Discretization effects are subtracted as far as possible using a calculation in the free quark limit. Our lattice calculations are extrapolated to the continuum limit by the linear fitting using data at three lattice spacings.

The extrapolated results for the exponent of the spectral density agree with those of the α_s^4 QCD perturbative calculation. This consistency of the eigenvalue λ dependence is highly non-trivial since the exponent of the spectral density is about 30–40% smaller than its asymptotic value. Our calculation adds another evidence of the validity of QCD in both non-perturbative and perturbative regimes.

We determine the strong coupling constant using the lattice calculation as an input. The discretization contribution is essential as in other methods to determine α_s . Our results are in agreement with those from other methods, although the precision is not competitive. The origin of relatively large errors is the remaining discretization uncertainty. Since the lattice data are limited in the eigenvalue range up to 1.2 GeV, the convergence for the perturbative expansion is also limited. In order to improve the precision for this determination, we should calculate the spectral density with finer lattice spacings and with reduced discretization

uncertainty.

V. CONCLUSIONS

In this thesis, I utilized the lattice simulation to determine parameters in perturbative expansions such as the charm quark mass and strong coupling constant. The lattice calculation with fine lattice spacings allowed us to reach the perturbative regime without loss of the non-perturbative contributions. I use the lattice data as an input to extract parameters in the perturbative series. Although there are many kinds of systematic errors such as the discretization errors, finite volume effects, disconnected diagram contributions, electromagnetic effects, and the truncation of perturbative series, I can determine physical parameters with high precision.

For parameters in QCD, I focused on the charm quark mass m_c and the strong coupling constant α_s . The temporal moment from short-distance correlator is a perturbative quantity, which is represented as a function of m_c and α_s . I match our lattice calculation to the $O(\alpha_s^3)$ perturbative expansion to extract parameters. After the discussion of systematic errors, I determined the m_c and α_s from the pseudo-scalar channel. Our result for m_c in $\overline{\text{MS}}$ scheme has $\sim 1\%$ precision.

Besides, the experimental data support the results of our lattice simulations. In order to demonstrate this consistency, I also studied the temporal moment of the vector currents, which could be defined by R ratio $\sigma_{e^+e^- \rightarrow q\bar{q}}/\sigma_{e^+e^- \rightarrow \mu^+\mu^-}$. I compared our lattice results to the experimental data and showed that the results coincided with each other.

I also investigated the Dirac eigenvalue density in the perturbative regime to determine parameters in QCD. Since the exponent of the Dirac eigenvalue density is perturbatively expanded up to $O(\alpha_s^4)$, our work is a test of the Standard Model in this order. Although our final result has $\sim 3\%$ error, our work confirmed that the procedure was an alternative way to determine α_s .

Through our studies in QCD, we may understand that one of the significant uncertainty comes from the truncation of the perturbative expansion. Although tireless efforts provide $O(\alpha_s^3)$ temporal moment and $O(\alpha_s^4)$ exponent of the Dirac eigenvalue, the truncation is still a dominant part of the error source. In order to reduce this systematic contribution, further studies for the fermion formulation are essential as I have shown in the domain-wall fermion formulation with generalized Pauli-Villars mass.

I provided detailed analysis for the fermion formulation which respects the chirality and

the locality for the Pauli-Villars mass generalization. I also provided a series of studies of parameter dependences in the domain-wall fermion. Since the Pauli-Villars mass extends the cut-off scale for the lattice formulation, the eigenvalue approximation was modified.

In the appendix, I briefly reviewed the tensor network representation. I also showed the analysis for the various parameters in fermion formulation. The generalization for the Pauli-Villars mass provides a better approximation for the Dirac eigenvalue.

ACKNOWLEDGMENTS

I would like to thank Shoji Hashimoto as my supervisor at KEK, and my supervisor Kazuhiro Tobe at Nagoya University. I also thank Brendan Fahy, Hidenori Fukaya, and Daisuke Kadoh as collaborators. JLQCD members, KEK theory center, and EHQG laboratory in Nagoya University supports are also much appreciated. I am very grateful to Masaaki Tomii, Kei Suzuki, Naoto Kan, Yuta Ito, Wataru Kuramoto, Mamiya Kawaguchi, Tsutomu Ishikawa, Hiroshi Suzuki, Taku Izubuchi, and Ryuichiro Kitano for fruitful discussions.

A. TENSOR NETWORK REPRESENTATION

We briefly review the tensor representation and related works such as the worldline and worldsheet representation, loop formulation, dual representation, dimer-monomer approach, and tensor renormalization group method. As a simple example, we consider fermionic fields and the path integral quantization. We introduce the functional integral with constants A_t and B_t which are contact and hopping term in the action. For the fermionic correlator $\langle \psi_N \bar{\psi}_k \rangle$,

$$\begin{aligned} \langle \psi_N \bar{\psi}_k \rangle &\equiv \int D\bar{\psi} D\psi \psi_N \bar{\psi}_k e^{\sum_{t=1}^N \bar{\psi}_t A_t \psi_t + \bar{\psi}_t B_t \psi_{t-1}} \\ &= \int D\bar{\psi} D\psi \psi_N \bar{\psi}_k e^{\sum_{t=1}^N \bar{\psi}_t A_t \psi_t} \prod_{t=1}^N \sum_{b_t=0}^1 (\bar{\psi}_t B_t \psi_{t-1})^{b_t}, \end{aligned} \quad (\text{A.1})$$

with the index b_t . We use Taylor expansion for the hopping term and use the Grassmann property $\psi^2 = 0$. We could integrate out all field variables ψ leaving the index b_t from the expansion. This index could be identified as the spin variables, and construct a tensor (matrix) representation of the fermion propagator. Namely, we translate measurements in the other representation, $\{\bar{\psi}, \psi\} \rightarrow \{b_t\}$ in this example. We will show details for supersymmetric quantum mechanics.

For scalar field, one of the most simple extension also take the Taylor expansion with the occupation number n_x^b . The hopping term $e^{\sum_t B_t \phi_t \phi_{t-1}}$ is represented as

$$e^{\sum_t B_t \phi_t \phi_{t-1}} = \prod_x \left(\sum_{n_x^b=0}^{\infty} \frac{1}{n_x^b!} (B_t \phi_t \phi_{t-1})^{n_x^b} \right). \quad (\text{A.2})$$

The index is no more finite set of integer. For numerical simulation, we could introduce the cutoff parameter $n_x^b < \Lambda_x$ which has to be sufficiently large to ignore the systematic error. This formulation is called as the loop formulation [23–25]. We can use Monte-Carlo simulation after this transformation from field variable ϕ to index parameter n_x^b . This strategy is known as the worm algorithm [133, 134]. It is also called as the world line representation in some works [31].

They also extend the “dual” representation for the gauge field theory without numerical calculation. The path integral with the Taylor expansion translates link variables of $SU(3)$ gauge field $U_{x,\mu\nu}^{abcd}$ to flux tubes $n_{x,\mu\nu}^{abcd}$. This application for the gauge field theory is the world

sheet representation [20]. They show that the equation could represent the color conservation law and symmetry of the gauge field in the world sheet representation.

The tensor renormalization group method relates to the dual representation in a higher dimension (or larger number of the hopping term). Let us consider the two-dimensional free Dirac fermion as an example. It could be represented as the two-flavor fermionic system,

$$\begin{aligned} \bar{\Psi} [\gamma_\mu \nabla_\mu] \Psi &= \bar{\psi}_{x,y} \psi_{x,y} + \bar{\psi}_{x,y} \xi_{x,y} - \bar{\xi}_{x,y} \xi_{x,y} + \bar{\xi}_{x,y} \psi_{x,y} \\ &\quad - \bar{\psi}_{x,y} \psi_{x,y+1} - \bar{\psi}_{x,y} \xi_{x+1,y} + \bar{\xi}_{x,y} \xi_{x,y+1} - \bar{\xi}_{x,y} \psi_{x+1,y}. \end{aligned} \quad (\text{A.3})$$

We take Taylor expansion to translate field variables to the spin variables. The four hopping terms are in the second line in (A.3). We expand each hopping terms by introducing the four indices $\{\psi_i, \xi_i\} \rightarrow \{a_i, b_i, c_i, d_i\}$. After the integrating out field variables, the system is represented by the network of the tensor,

$$T_{a_{x,y}, a_{x-1,y}, b_{x,y}, b_{x-1,y}, c_{x,y}, c_{x,y-1}, d_{x,y}, d_{x,y-1}}. \quad (\text{A.4})$$

In any case, the tensor representation introduces some indices which could be identified as the spin or flux tube degree of freedom after integrating out the field variables. Since the calculation does not use the importance sampling like as the Monte-Carlo method, the tensor network representation may not suffer from the sampling problem. We will show an example in the supersymmetric quantum mechanics.

a. SUSY QM

We use the $\mathcal{N} = 2$ supersymmetric quantum mechanics on the lattice with one exact supercharge according to [135].

First, we introduce the theory on the continuum space-time. The system has scalar $\phi(t)$ and Grassmann variables $\psi(t)$ and $\bar{\psi}(t)$, with the periodic boundary condition in finite period β .

The action of SUSY QM is given by

$$S = \int_0^\beta dt \left\{ \frac{1}{2} (\partial_t \phi(t))^2 + \frac{1}{2} W(\phi(t))^2 + \bar{\psi}(t) (\partial_t + W'(\phi(t))) \psi(t) \right\}. \quad (\text{A.5})$$

We refer to $W(\phi)$, which is an arbitrary function of ϕ , as a superpotential. (A.5) has

supersymmetry as the invariance under the transformation,

$$\delta\phi = \epsilon\psi + \bar{\epsilon}\bar{\psi}, \quad (\text{A.6})$$

$$\delta\psi = -\bar{\epsilon}(\partial_t\phi - W(\phi)), \quad (\text{A.7})$$

$$\delta\bar{\psi} = -\epsilon(\partial_t\phi + W(\phi)), \quad (\text{A.8})$$

where ϵ and $\bar{\epsilon}$ are one-component Grassmann numbers.

We use the path integral quantization and define the partition function as

$$Z = \int D\phi D\bar{\psi} D\psi e^{-S}, \quad (\text{A.9})$$

The partition function Z corresponds to the Witten index $\text{Tr}(-1)^F$, which is an order parameter of the breaking of the supersymmetry in the supersymmetric quantum mechanics. Namely, the supersymmetry must be broken if the system has $Z = 0$. For the supersymmetric quantum mechanics case, the spontaneous symmetry breaking is controlled by the superpotential $W(\phi)$ [136, 137].

We introduced the tensor representation for the supersymmetric quantum mechanics in Ref. [138, 139]. For the system with the superpotential $W(\phi) = m\phi + g\phi^2$ with the mass m and the coupling g , the supersymmetry is spontaneously broken. Besides, for the weak coupling regime, there is a sampling problem since the potential has degenerated minimum which is separated by the potential barrier. In order to demonstrate the tensor representation could overcome this problem, we calculate the energy.

At the weak coupling limit, our numerical calculation is consistent with the perturbative expansion. We estimate the systematic error from fitting by the difference from the fit for the finest four data points, and the result is $R = 0.998(7) - 0.91(16)\lambda^2$. Since the result from perturbative expansion is $R = 1$, our result is consistent with the perturbation. Details are in Ref [138, 139].

B. MORE CONTINUUM LIKE EIGENVALUE WITH GENERALIZED PARAMETERS

a. Eigenvalue on the lattice

We can calculate Dirac eigenvalue from operator representation in each momentum, $p_\mu^{\text{para}} \equiv (p, \alpha p, \beta p, \gamma p)$ with constants α, β, γ . To compare our lattice formulation with continuum, we define continuum Dirac operator with parameterized momentum,

$$D_{\text{cont}}^\dagger D_{\text{cont}}(p_\mu^{\text{para}}, m_f^{\text{scaled}}) \equiv (1 + \alpha^2 + \beta^2 + \gamma^2)p^2 + (m_f^{\text{scaled}})^2 \quad (\text{B.1})$$

and its rescaled version,

$$\lambda_{\text{cont}}(p_\mu^{\text{para}}) \equiv \sqrt{p^2 + (m_f^{\text{scaled}})^2} = \sqrt{\frac{D_{\text{cont}}^\dagger D_{\text{cont}}(p_\mu^{\text{para}}, \sqrt{(1 + \alpha^2 + \beta^2 + \gamma^2)}m_f^{\text{scaled}})}{(1 + \alpha^2 + \beta^2 + \gamma^2)}}. \quad (\text{B.2})$$

For comparison, we also define lattice rescaled absolute values of Dirac eigenvalue with parameterized momentum p_μ^{para} ,

$$\lambda_{\text{lat}}(p_\mu^{\text{para}}) \equiv \sqrt{\frac{D_{\text{OV}}^\dagger D_{\text{OV}}(p_\mu^{\text{para}}, \sqrt{(1 + \alpha^2 + \beta^2 + \gamma^2)}m_f^{\text{scaled}}, M_0, r, c, m_p, u_0)}{(1 + \alpha^2 + \beta^2 + \gamma^2)}}. \quad (\text{B.3})$$

By this rescaling, we can compare our parameters tuned lattice Dirac operator with continuum operator with any momenta. We will discuss each parameters.

1. Domain Wall height M_0

First we focus on the massless fermion $m_f = 0$ for simplicity. Since the domain wall height M_0 changes the overall scale, it affect on the all region of the eigenvalue. Figure 22 shows that M_0 dependence of massless eigenvalue, with the parameter $(M_0, r = 1, c = 1, m_p = 1)$. In this parameterization, $M_0 = 1$ might be most suitable for approximations.

We have to pay attention to the Domain-wall height from another point of view, especially the constraint

$$(2 - cM_0) > 0, \quad (\text{B.4})$$

from consistency at the continuum limit. We also have to pay attention to the unphysical oscillation which relates to the Wilson term. For $c = 1$, the correlator has no oscillational

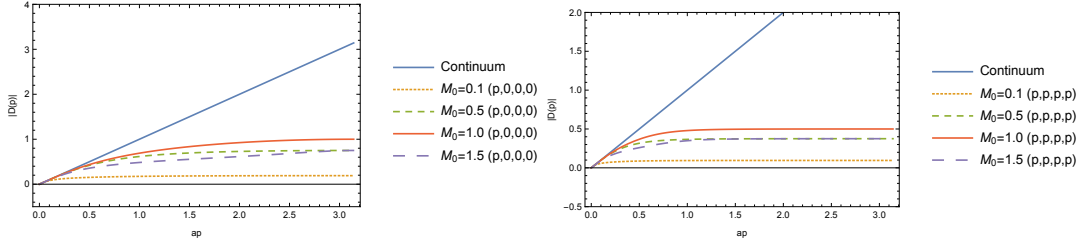


FIG. 22. The eigenvalues of different domain-wall heights M_0 with the momentum $(p, 0, 0, 0)$ (left) and (p, p, p, p) (right).

behavior if the parameters satisfy the condition,

$$1 - M_0 + 4r(1 - u_0) > 0. \quad (\text{B.5})$$

Usually we choose $M_0 = 1$ for $u_0 \sim 1$ by smearing, and $M_0 \sim 1.4$ for $u_0 \sim 0.88$ without smearing. In any case, we can tune our domain-wall height within these constraints.

2. Wilson mass term r

Wilson mass term is induced for elimination of doubler particle, and it can change mainly higher momentum region. Note that this term r cannot change scale of Dirac operator since it is not contained in scale factor. Namely, this term cannot change eigenvalue cutoff scale. Figure 23 shows the Wilson mass term r dependence of massless eigenvalue, with the parameters ($M_0 = 1, r, c = 1, m_p = 1$). In order to eliminate doublers, these parameters have to be satisfy

$$r(1 + u_0) > M_0. \quad (\text{B.6})$$

For the Wilson coefficient, $r \sim 3$ provides a good approximation.

3. Möbius parameter c

Möbius parameter has effects on $O(a^2)$ contribution of the sign function. Figure 24 shows the Möbius parameter c dependence of massless eigenvalue, with the parameters ($M_0 = 1, r = 1, c, m_p = 1$). Again it has to satisfy the condition,

$$(2 - cM_0) > 0 \quad (\text{B.7})$$

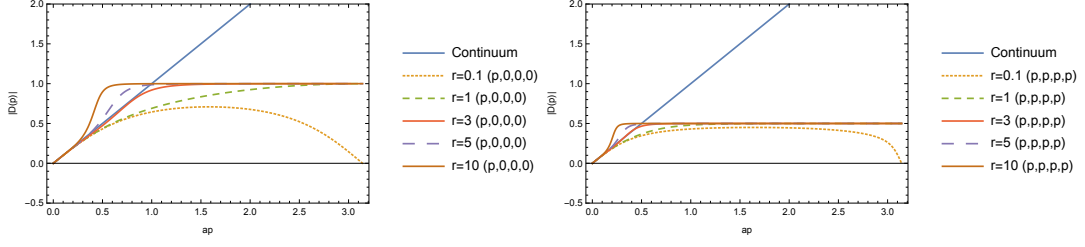


FIG. 23. The eigenvalues of different Wilson coefficients r with the momentum $(p, 0, 0, 0)$ (left) and (p, p, p, p) (right).

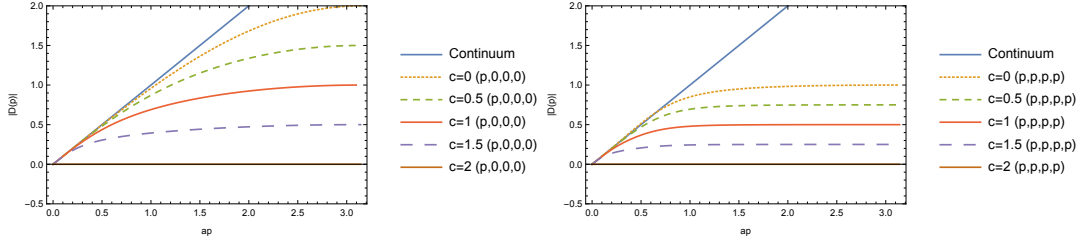


FIG. 24. The eigenvalue of different kernel parameters c with the momentum $(p, 0, 0, 0)$ (left) and (p, p, p, p) (right).

for continuum limit. For the Möbius parameter, $c = 0$ is the most suitable for the massless case without considering the numerical cost.

4. Pauli-Villars mass m_p

Since the Pauli-Villars mass can only change a cutoff scale of the eigenvalue, it mainly affects higher momentum regions. Figure 25 shows the Möbius parameter m_p dependence of massless eigenvalue, with the parameters $(M_0 = 1, r = 1, c = 1, m_p)$. For the Pauli-Villars mass, $m_p \sim 3$ is suitable for the approximation.

b. Lorentz symmetry in momentum space

If we take lattice regularization to construct quantum field theory, discretized space-time breaks the Lorentz symmetry. This violation is partially represented as the difference between longitudinal $(p, 0, 0, 0)$ and diagonal (p, p, p, p) direction. More precisely, we inves-

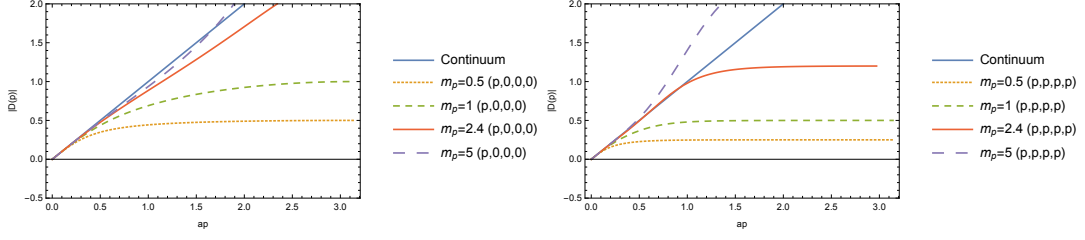


FIG. 25. The eigenvalue of different Pauli-Villars masses m_p with the momentum $(p, 0, 0, 0)$ (left) and (p, p, p, p) (right).

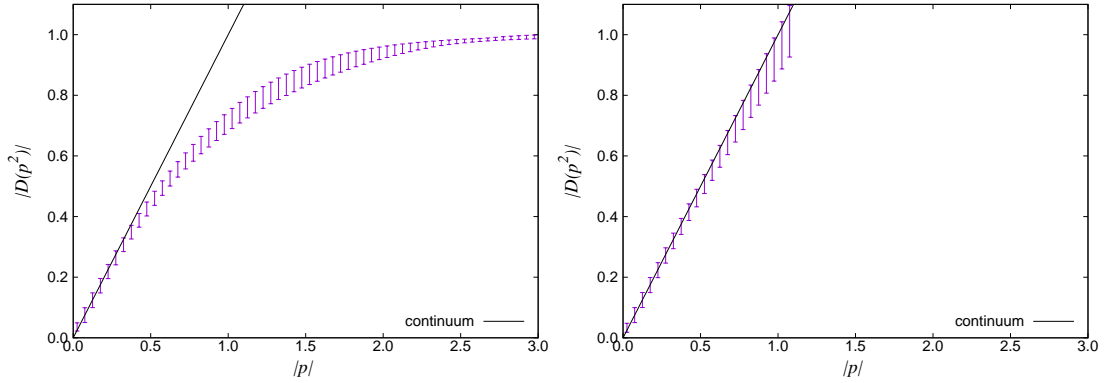


FIG. 26. The Lorentz symmetry violation of Shamir domain-wall fermion with usual $m_p = 1.0$ (Left) and $m_p = 2.4$ (Right). Bands represent maximum and minimum eigenvalues as Lorentz violation. This graph is plotted by 10^9 sets of momenta, which is sufficient statistics.

tigate the symmetry using $\lambda_{\text{lat}}(p^2)$ which is the function of p^2 . We statistically calculate the function by generating large amount of random momenta p_μ . We use 10^9 sets of momenta for this study.

Figure 26 shows Lorentz symmetry of usual Shamir domain-wall fermion ($M_0 = 1, r = 1, c = 1$) with different Pauli-Villars mass $m_p = 1.0$ and $m_p = 2.4$. In this figure, bands represent maximum and minimum eigenvalues (not error), and then it represents these relates Lorentz symmetry violation in momentum space. As we already discussed above, $m_p = 2.4$ realizes a better approximation, but it might enhance Lorentz symmetry violation in higher momentum region $ap \sim 1$.

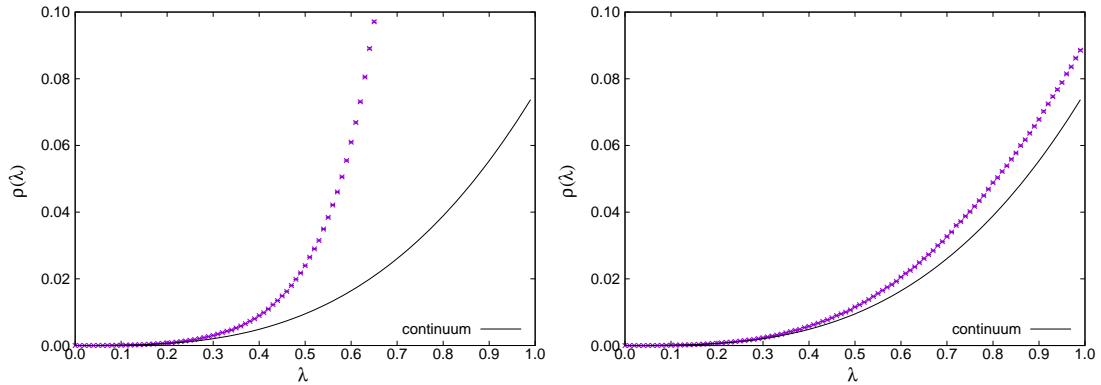


FIG. 27. The eigenvalue density of Shamir domain-wall fermion with usual $m_p = 1.0$ (Left) and $m_p = 2.4$ (Right) with its statistical error. This graph is plotted by 10^9 sets of momenta, which is sufficient statistics.

c. Eigenvalue density

We also consider the eigenvalue density. This approximation strongly relates the mean value of eigenvalue in each momentum $\langle \lambda_{\text{lat}}(p) \rangle$. For more finer tuning, we calculate $\langle \lambda_{\text{lat}}(p) \rangle$ by numerical calculations. For the free field continuum theory, the eigenvalue density is written as follows,

$$\rho(\lambda) = \frac{3}{4\pi^2} \lambda^3. \quad (\text{B.8})$$

Figure 27 shows eigenvalue densities of usual Shamir domain-wall fermion ($M_0 = 1, r = 1, c = 1$) with different Pauli-Villars mass $m_p = 1.0$ and $m_p = 2.4$. Again, $m_p = 2.4$ is a better approximation.

C. TUNED PARAMETER SETS EXAMPLES

a. Massless $m_f = 0$

For more precise investigation, we first focused on massless fermion $m_f = 0$. We will show approximations of various sets of the parameters.

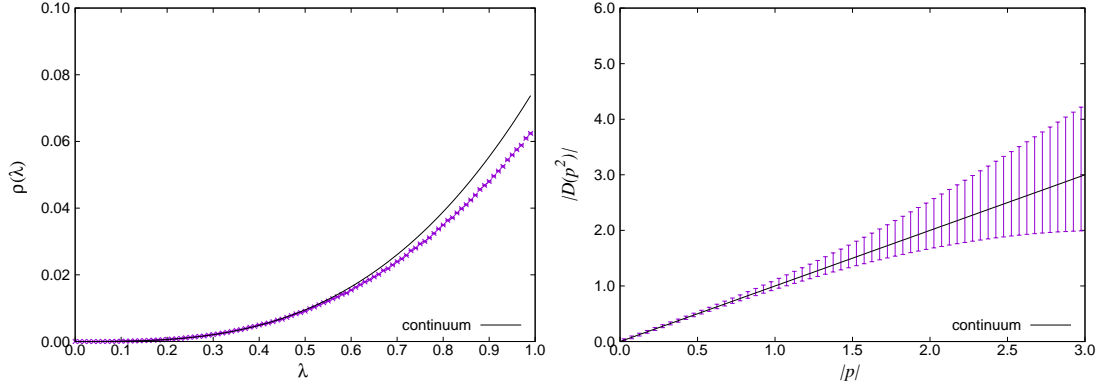


FIG. 28. The eigenvalue density (left) and the Lorentz symmetry violation (right) of Wilson fermion ($r = 1$). This graph is plotted by 10^9 sets of momenta, which is sufficient statistics.

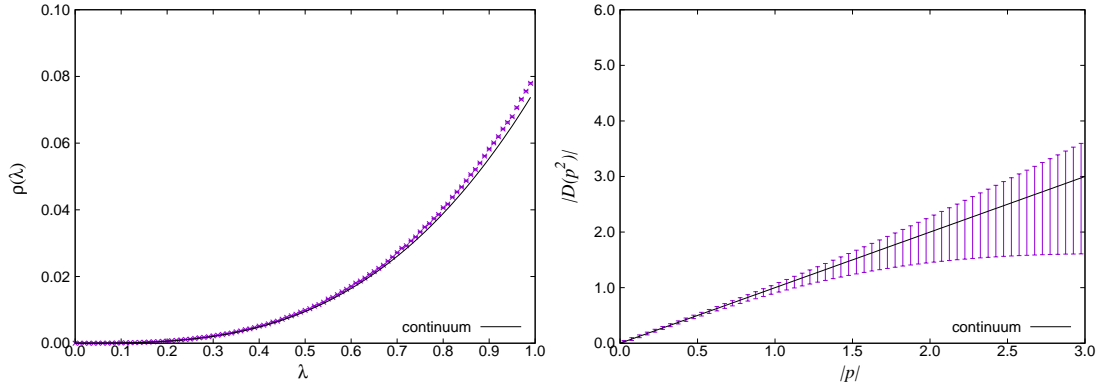


FIG. 29. The eigenvalue density (left) and the Lorentz symmetry violation (right) of Wilson fermion ($r = 0.8053$). This graph is plotted by 10^9 sets of momenta, which is sufficient statistics.

1. For comparison: Wilson fermion

For comparison, we consider the eigenvalue of Wilson fermion and its Lorentz symmetry violation. Figure 28 shows the results for $r = 1$ and Figure 29 shows the those for $r = 0.8053$.

- (1): The approximation is good up to $\lambda \sim 0.6$.
- (2): The eigenvalue is cutoffed $|aD| = 8r$ by definition. In the momentum region $|ap| < \pi$, the eigenvalue is cutoffed $|aD| \sim \sqrt{4 + 16r^2}$.
- (3): Lorentz symmetry violation grows up in higher momentum region.

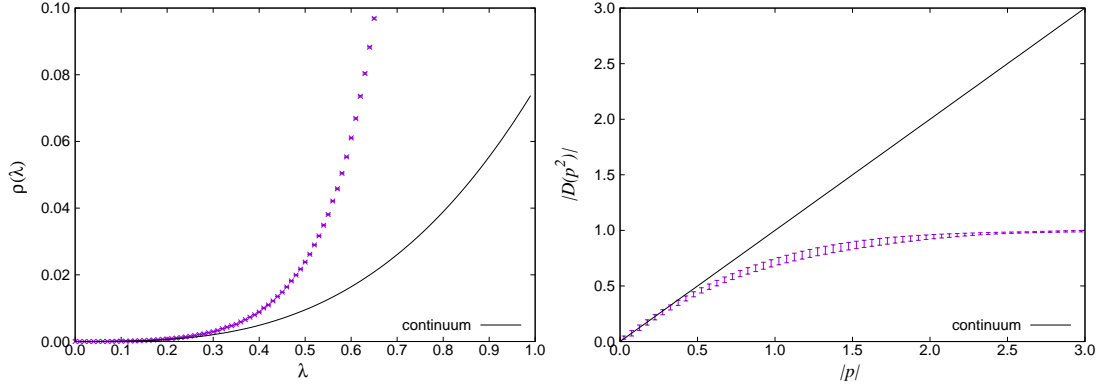


FIG. 30. The eigenvalue density (left) and the Lorentz symmetry violation (right) of Shamir domain-wall fermion ($M_0 = 1, r = 1, c = 1, m_p = 1$). This graph is plotted by 10^9 sets of momenta, which is sufficient statistics.

2. For comparison: Shamir domain-wall fermion

We also show Shamir type domain-wall fermion eigenvalue and its Lorentz violation bands. Figure 30 shows the results.

- (1): The approximation is good up to $\lambda \sim 0.3$.
- (2): The eigenvalue is cutoffed $|aD| = 1$ by definition.
- (3): The Lorentz symmetry in higher momentum region is better than Wilson fermion because of the cutoff.

3. $m_p \rightarrow \infty$ limit

Pauli-Villars mass tends to infinite limit is the eigenvalue projection to imaginary axis. Figure 31 shows the results.

- (1): The approximation is good up to $ap \sim 1$ and $\lambda \sim 0.7$.
- (2): Since the eigenvalue is cutoffed $|aD| = m_p$ by definition, the eigenvalue at $m_p \rightarrow \infty$ limit is not cutoffed.
- (3): Since there is no cutoff, the Lorentz symmetry violation grows up in higher momentum region.

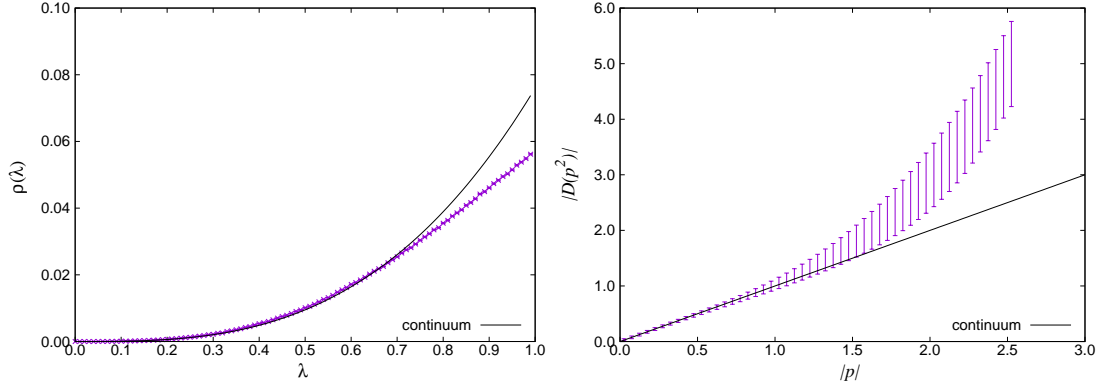


FIG. 31. The eigenvalue density (left) and the Lorentz symmetry violation (right) with parameter $m_p \rightarrow \infty$. This graph is plotted by 10^9 sets of momenta, which is sufficient statistics.

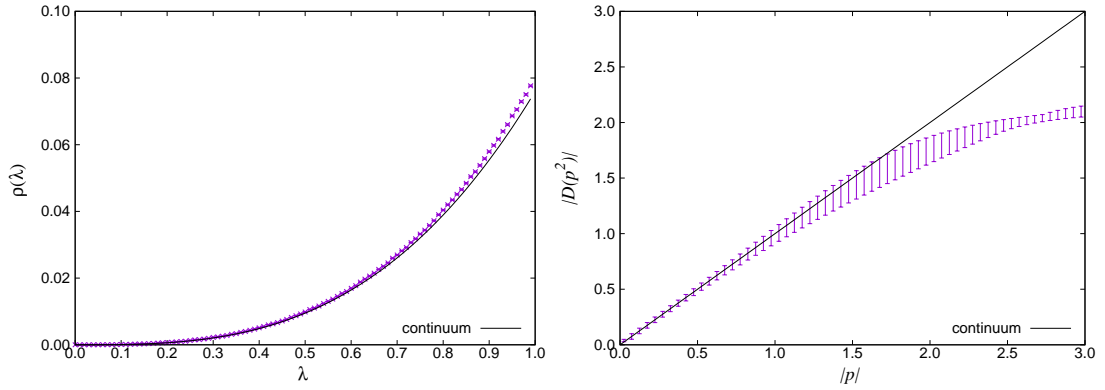


FIG. 32. The eigenvalue density (left) and the Lorentz symmetry violation (right) with parameter $M_0 = 1.4, c = 0.4$. This graph is plotted by 10^9 sets of momenta, which is sufficient statistics.

4. $(M_0 = 1.4, r = 1, c = 0.3265, m_p = 1)$

As an example, we tune M_0 and c for the approximation of the eigenvalue density. Figure 32 shows the result,

- (1): The approximation is good up to $ap \sim 1$ and $\lambda \sim 0.8$.
- (2): The eigenvalue is cutoffed $|aD| = M_0(2 - cM_0) = 2.16006$ by definition.

5. $(M_0 = 0.6478, r = 0.925, c = 0.0, m_p = 2.827)$

We also show the result of tuned parameters with $c = 0$. Figure 33 shows the result,

- (1): The approximation is good up to $ap \sim 1$ and $\lambda \sim 1$.
- (2): The eigenvalue is cutoffed $|aD| = M_0(2 - cM_0)m_p = 3.66266$ by definition.

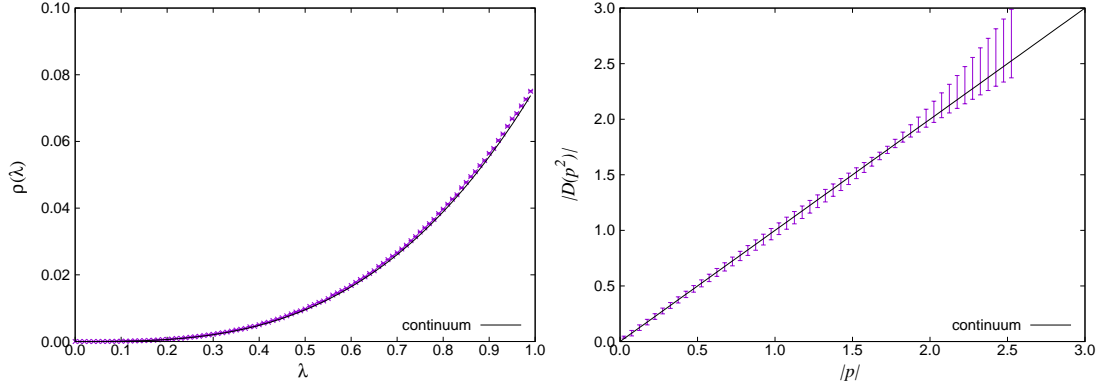


FIG. 33. The eigenvalue density (left) and the Lorentz symmetry violation (right) with parameter ($M_0 = 0.6478, r = 0.925, c = 0.0, m_p = 2.827$). This graph is plotted by 10^9 sets of momenta, which is sufficient statistics.

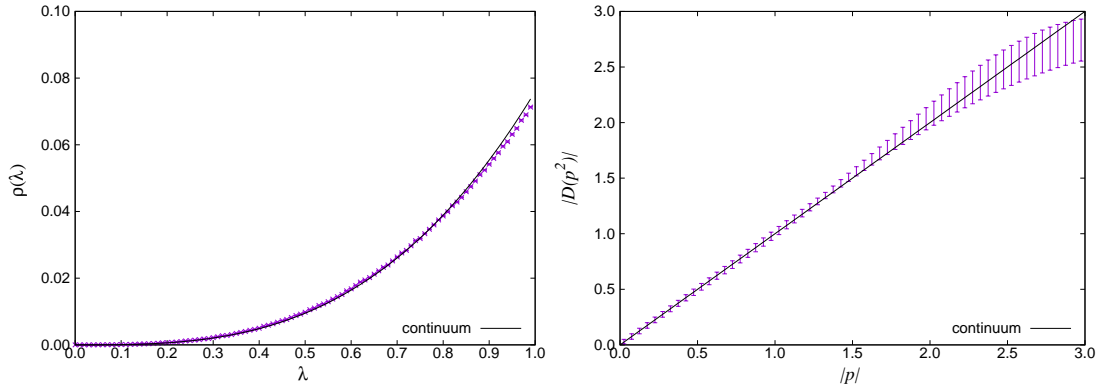


FIG. 34. The eigenvalue density (left) and the Lorentz symmetry violation (right) with parameter ($M_0 = 0.405, r = 1.28, c = 0.21, m_p = 3.8$). This graph is plotted by 10^9 sets of momenta, which is sufficient statistics.

(3): Lorentz symmetry is modified in $ap < 1$.

$$6. \quad (M_0 = 0.405, r = 1.28, c = 0.21, m_p = 3.8)$$

As another example, we can tune all of these parameters in the formulation. Figure 34 shows the result,

(1): The approximation is good up to $ap \sim 1$ and $\lambda \sim 0.8$.

(2): The eigenvalue is cutoffed $|aD| = M_0(2 - cM_0)m_p = 2.94711$ by definition.

(3): Lorentz symmetry is modified in $ap < 1$.

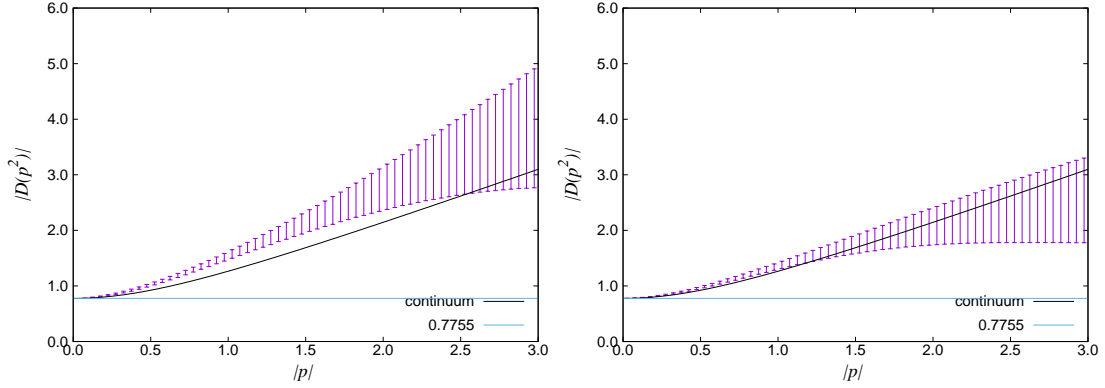


FIG. 35. The eigenvalue of Wilson fermion for $r = 1$ (left) and $r = 0.5$ (right). This graph is plotted by 10^9 sets of momenta, which is sufficient statistics.

b. Massive case $m_f \neq 0$

The approximation of the higher momentum region relates to the approximation of the massive fermion Dirac operators. For this case, the Pauli-Villars mass generalization is more important to approximate the eigenvalue at the continuum limit since the mass is a cutoff scale.

1. For comparison: Wilson fermion

For comparison we consider eigenvalue of Wilson fermion and its Lorentz symmetry violation. Figure 35 shows $r = 1$ and $r = 0.5$ result.

- (1): The approximation is not good since the fermion mass is too heavy.
- (2): The Lorentz symmetry violation grows up in the higher momentum region.

2. For comparison: Shamir domain-wall fermion

We also show Shamir type domain-wall fermion eigenvalue and its Lorentz violation bands. Figure 36 shows the result,

- (1): The approximation is not good since the cutoff scale is $|aD| = 1$.

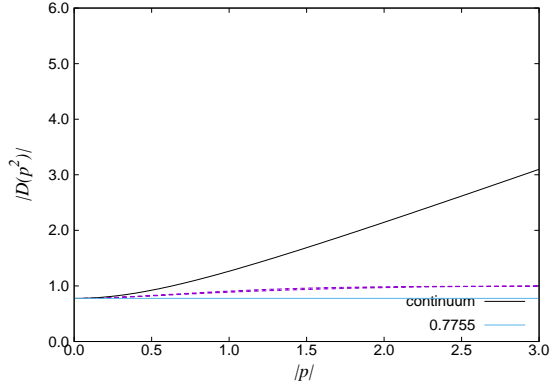


FIG. 36. The eigenvalue density (left) and the Lorentz symmetry violation (right) of Shamir domain-wall fermion ($M_0 = 1, r = 1, c = 1, m_p = 1$). This graph is plotted by 10^9 sets of momenta, which is sufficient statistics.

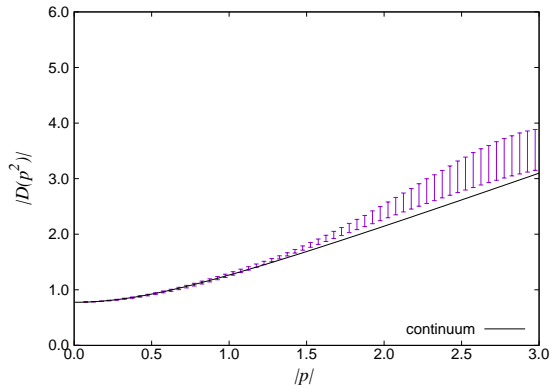


FIG. 37. The eigenvalue density (left) and the Lorentz symmetry violation (right) of Möbius domain-wall fermion ($M_0 = 0.405, r = 1.28, c = 0.21, m_p = 5.06$). This graph is plotted by 10^9 sets of momenta, which is sufficient statistics.

$$3. \quad m_f = 1, m_p = 5.06, M_0 = 0.405, r = 1.28, c = 0.21$$

We discuss the eigenvalue of the same pole mass with tuned parameters. Figure 37 shows the result,

- (1): The approximation is good up to $ap \sim 1$.
- (2): The eigenvalue is cutoffed $|aD| = M_0(2 - cM_0)m_p = 3.92431$ by definition.
- (3): Lorentz symmetry is also tuned to realize in a region $ap < 1$.

D. POLE AND DOUBLER

We also investigate the pole and the doubler for overlap fermion by numerical integration. We set $m_p = 1$ since the pole does not depend on the Pauli-Villars mass after introducing the scaled mass m_f^{scaled} . For the calculation of the pole mass and locality, we consider

$$\frac{1}{2\pi} \int_{-\pi}^{\pi} dp e^{ipt} D_{\text{OV}}^{-1} = \frac{1}{2\pi} \frac{m_p - m_f}{M_0(2 - cM_0)m_p} \int dp e^{ipt} \langle q\bar{q} \rangle \quad (\text{D.1})$$

This relation is satisfied since a constant term can be ignored by integral. We choose $p_\mu = (p, 0, 0, 0)$,

$$N(t) \equiv \frac{1}{M_0(2 - cM_0)} \frac{1}{2\pi} \int dp e^{ipt} \langle q\bar{q} \rangle \equiv \frac{(1 + \gamma_0)}{2} [K e^{-m_{\text{pole}}t} + L e^{-m_{\text{doubler}}t}], \quad (\text{D.2})$$

$$\equiv \frac{(1 + \gamma_0)}{2} P(t). \quad (\text{D.3})$$

We define $E_{\text{eff}}^{\text{pole}}(t)$, $E_{\text{eff}}^{\text{doubler}}(t)$, K_{eff} , and L_{eff} ,

$$E_{\text{eff}}^{\text{pole}}(t) \equiv \log \left[\frac{P(t)}{P(t+1)} \right], \quad (\text{D.4})$$

$$K_{\text{eff}}(t) \equiv e^{E_{\text{eff}}^{\text{pole}}t} P(t), \quad (\text{D.5})$$

$$E_{\text{eff}}^{\text{doubler}}(t) \equiv E_{\text{eff}}^{\text{pole}} + \log \left[\frac{e^{E_{\text{eff}}^{\text{pole}}t} P(t) - K_{\text{eff}}}{e^{E_{\text{eff}}^{\text{pole}}(t+1)} P(t+1) - K_{\text{eff}}} \right], \quad (\text{D.6})$$

$$L_{\text{eff}}(t) \equiv e^{E_{\text{eff}}^{\text{doubler}}t} \left[e^{E_{\text{eff}}^{\text{pole}}t} P(t) - K_{\text{eff}} \right], \quad (\text{D.7})$$

where functions without variable are defined as the value at sufficiently large t . The overall scale K_{eff} is the factor studied by Lepage, Mackenzie, and Kronfeld [140, 141] for the validity of the lattice. This coefficient is the KLM factor.

We define the effective dynamical mass $M_{\text{mom}}(p)$ as a function of $|\mathbf{p}|$ from the $i\gamma_0$ part of quark propagator with momentum \mathbf{p} ,

$$Q(t; p_1, p_2, p_3) \equiv \frac{1}{M_0(2 - cM_0)} \frac{1}{2\pi} \int dp e^{ipt} \langle q\bar{q} \rangle \text{ (of gamma zero part)} \quad (\text{D.8})$$

$$\equiv \frac{\gamma_0}{2} U(t; p_1, p_2, p_3), \quad (\text{D.9})$$

The dynamical mass $M_{\text{mom}}(p_1, p_2, p_3)$ is written as follows,

$$M_{\text{mom}}(\mathbf{p}) \equiv \frac{\mathbf{p}^2}{2} \frac{1}{\log \left[\frac{U(t; \mathbf{p})}{U(t+1; \mathbf{p})} \right] - m_{\text{pole}}}. \quad (\text{D.10})$$

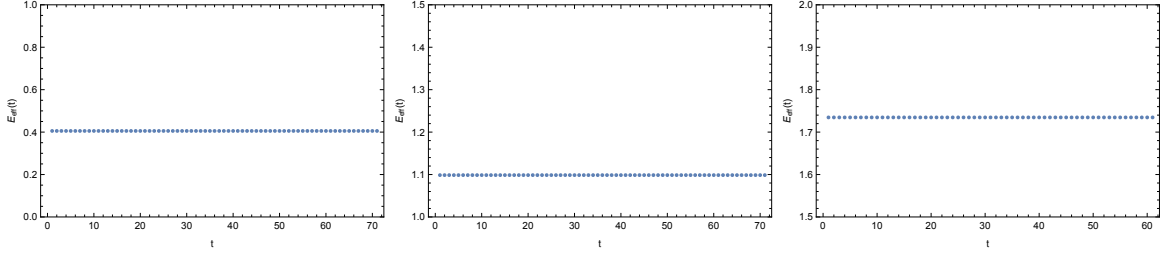


FIG. 38. The pole mass with $c = 0$ for the bare mass $m_f = 0.2$ (left), $m_f = 0.5$ (middle), and $m_f = 0.7$ (right) are shown.

This is related to dynamical mass of the heavy quark effective theory,

$$E(\mathbf{p}) = m_{\text{pole}} + m_{\text{doublers}} + \frac{\mathbf{p}^2}{2M_{\text{mom}}(\mathbf{p} = 0)} + \dots \quad (\text{D.11})$$

For continuum theory, the effective dynamical mass and the pole mass should be equal, $M_{\text{mom}}(\mathbf{p}) = E_{\text{eff}}^{\text{pole}}$ in $O(\mathbf{p}^4)$ order. We compare the mass for investigating the discretization effect.

a. Effective mass and doubler

We show the pole structure for various Möbius parameter c as the effective mass and doubler mass. For $c = 0$, there is no doubler pole as shown in Figure 38. In any bare mass m , the numerical integration uniquely determines the pole. For finite $c \neq 0$, there are other contributions from doublers as shown in Figures 39 and 40. From our numerical integration, larger Möbius parameter c generates lighter doubler mass. Since the doubler mass has no dependence on the bare mass, the doubler contribution becomes more severe for heavier fermion. The small Möbius parameter is preferable since the doubler mass becomes heavy.

We also compare the effective pole mass E_{eff} and the kinematic mass M_{mom} in order to investigate the discretization effect. Figure 41 shows the numerical calculation. In any Möbius parameter c , while the effective pole mass E_{eff} and the kinematic mass M_{mom} has deviation from scaled pole mass m_f^{scaled} in larger m_f^{scaled} . We could tune the Möbius parameter $c \simeq 0.6$ to satisfy the equation $E_{\text{eff}} = m_f^{\text{scaled}}$.

Figure 42 shows the KLM factor K_{eff} . This factor should be 1.0 for the continuum theory. Then the discretization effect is the deviation of the KLM factor from 1.0. For a better approximation, we should choose $c < 0.6$.

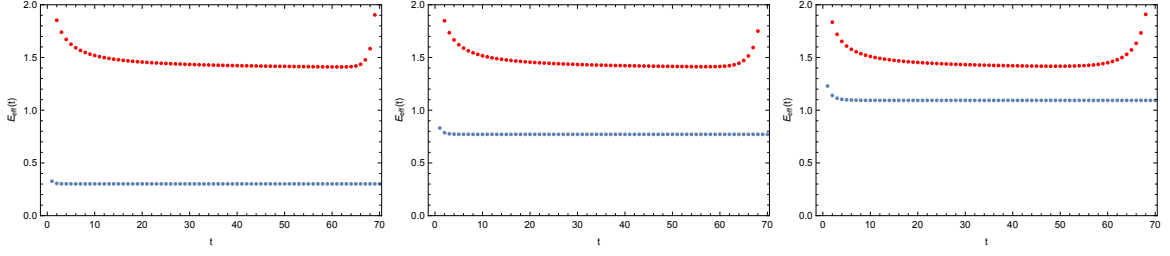


FIG. 39. The pole mass (blue) and doubler mass (red) with $c = 0.5$ for the bare mass $m_f = 0.2$ (left), $m_f = 0.5$ (middle), and $m_f = 0.7$ (right) are shown.

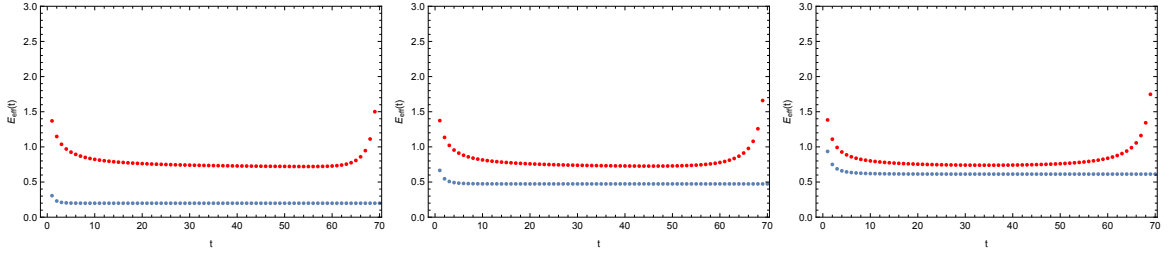


FIG. 40. The pole mass (blue) and doubler mass (red) with $c = 1$ for the bare mass $m_f = 0.2$ (left), $m_f = 0.5$ (middle), and $m_f = 0.7$ (right) are shown.

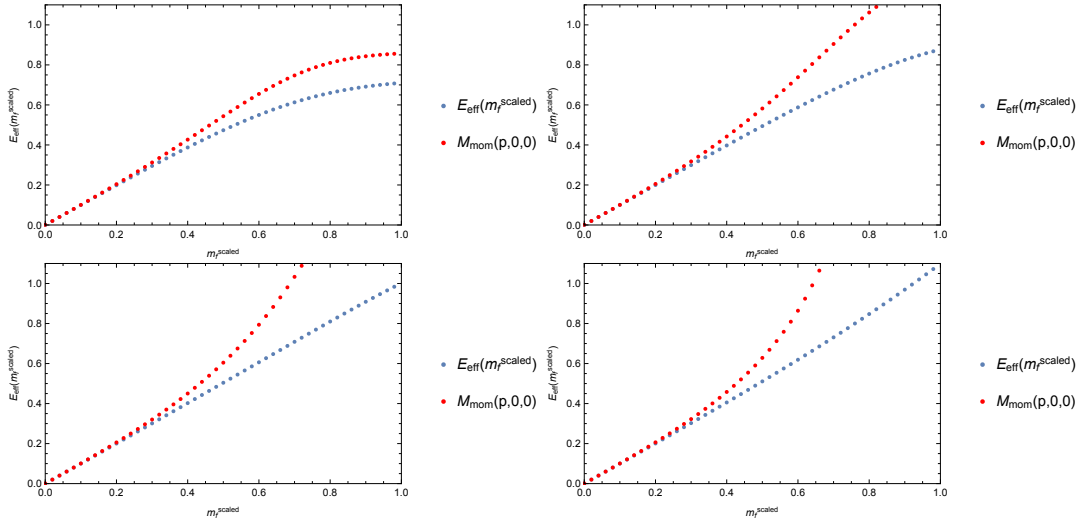


FIG. 41. The pole mass $E_{\text{eff}}(p)$ and the kinematic mass $M_{\text{mom}}(\mathbf{p})$ as the function of the scaled mass $m_f^{\text{scaled}} \equiv (2 - cM_0)M_0m_f$ with Möbius parameters $c = 1.0$ (top left), $c = 0.8$ (top right), $c = 0.6$ (bottom left), $c = 0$ (bottom right). All calculations are at $t = 30$.

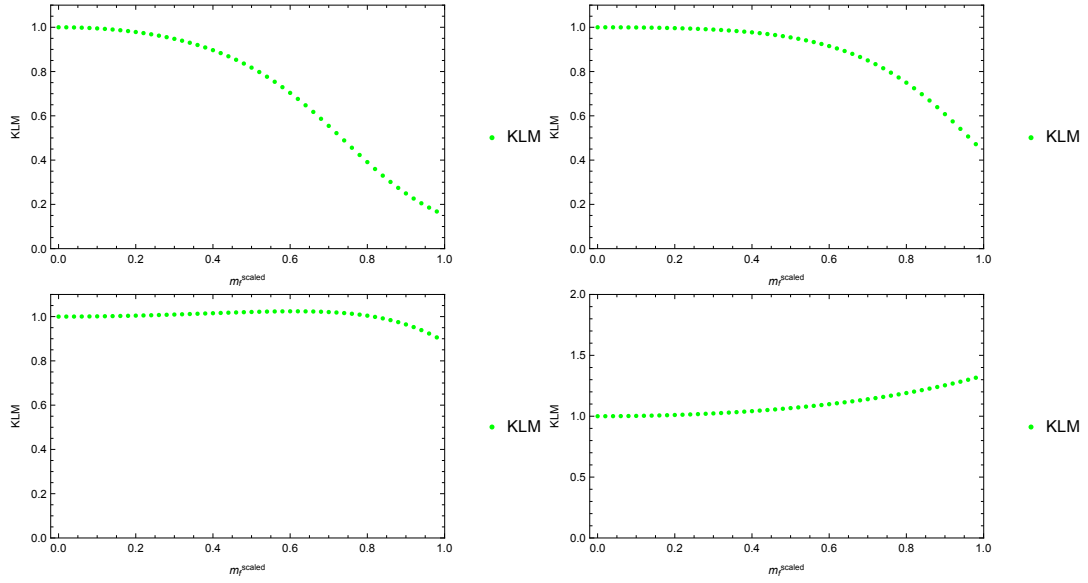


FIG. 42. The KLM factor as the function of the scaled mass $m_f^{\text{scaled}} \equiv (2 - cM_0)M_0m_f$ with Möbius parameters $c = 1.0$ (top left), $c = 0.8$ (top right), $c = 0.6$ (bottom left), $c = 0$ (bottom right). All calculations are at $t = 30$.

References

- [1] A. Maier, P. Maierhofer, and P. Marquard, Nucl. Phys. **B797**, 218 (2008), arXiv:0711.2636 [hep-ph].
- [2] A. Maier, P. Maierhofer, P. Marquard, and A. V. Smirnov, Nucl. Phys. **B824**, 1 (2010), arXiv:0907.2117 [hep-ph].
- [3] S. Aoki *et al.* (PACS-CS), Phys. Rev. **D79**, 034503 (2009), arXiv:0807.1661 [hep-lat].
- [4] Z. Fodor and C. Hoelbling, Rev. Mod. Phys. **84**, 449 (2012), arXiv:1203.4789 [hep-lat].
- [5] S. Aoki *et al.*, Eur. Phys. J. **C77**, 112 (2017), arXiv:1607.00299 [hep-lat].
- [6] I. Allison *et al.* (HPQCD), Phys. Rev. **D78**, 054513 (2008), arXiv:0805.2999 [hep-lat].
- [7] C. McNeile, C. T. H. Davies, E. Follana, K. Hornbostel, and G. P. Lepage, Phys. Rev. **D82**, 034512 (2010), arXiv:1004.4285 [hep-lat].
- [8] B. Chakraborty, C. T. H. Davies, B. Galloway, P. Knecht, J. Koponen, G. C. Donald, R. J. Dowdall, G. P. Lepage, and C. McNeile, Phys. Rev. **D91**, 054508 (2015), arXiv:1408.4169 [hep-lat].
- [9] K. Nakayama, B. Fahy, and S. Hashimoto, Phys. Rev. **D94**, 054507 (2016), arXiv:1606.01002 [hep-lat].
- [10] B. Dehnadi, A. H. Hoang, V. Mateu, and S. M. Zebarjad, JHEP **09**, 103 (2013), arXiv:1102.2264 [hep-ph].
- [11] J. H. Kuhn, M. Steinhauser, and C. Sturm, Nucl. Phys. **B778**, 192 (2007), arXiv:hep-ph/0702103 [HEP-PH].
- [12] J. H. Kuhn and M. Steinhauser, Nucl. Phys. **B619**, 588 (2001), [Erratum: Nucl. Phys. **B640**, 415 (2002)], arXiv:hep-ph/0109084 [hep-ph].
- [13] A. H. Hoang and M. Jamin, Phys. Lett. **B594**, 127 (2004), arXiv:hep-ph/0403083 [hep-ph].
- [14] K. Nakayama, H. Fukaya, and S. Hashimoto, Phys. Rev. **D98**, 014501 (2018), arXiv:1804.06695 [hep-lat].
- [15] G. Cossu, H. Fukaya, S. Hashimoto, T. Kaneko, and J.-I. Noaki, PTEP **2016**, 093B06 (2016), arXiv:1607.01099 [hep-lat].
- [16] E. E. Di Napoli and Y. Saad, arXiv:1308.4275 [cs NA].

- [17] K. G. Chetyrkin and J. H. Kuhn, Nucl. Phys. **B432**, 337 (1994), arXiv:hep-ph/9406299 [hep-ph].
- [18] J.-L. Kneur and A. Neveu, Phys. Rev. **D92**, 074027 (2015), arXiv:1506.07506 [hep-ph].
- [19] M. Levin and C. P. Nave, Phys. Rev. Lett. **99**, 120601 (2007), arXiv:cond-mat/0611687 [cond-mat.stat-mech].
- [20] C. Marchis and C. Gattringer, Phys. Rev. **D97**, 034508 (2018), arXiv:1712.07546 [hep-lat].
- [21] H. Kawauchi and S. Takeda, Phys. Rev. **D93**, 114503 (2016), arXiv:1603.09455 [hep-lat].
- [22] D. Kadoh, Y. Kuramashi, Y. Nakamura, R. Sakai, S. Takeda, and Y. Yoshimura, (2018), arXiv:1801.04183 [hep-lat].
- [23] D. Baumgartner and U. Wenger, Nucl. Phys. **B894**, 223 (2015), arXiv:1412.5393 [hep-lat].
- [24] D. Baumgartner and U. Wenger, Nucl. Phys. **B897**, 39 (2015), arXiv:1503.05232 [hep-lat].
- [25] D. Baumgartner and U. Wenger, Nucl. Phys. **B899**, 375 (2015), arXiv:1505.07397 [hep-lat].
- [26] R. Sakai, S. Takeda, and Y. Yoshimura, PTEP **2017**, 063B07 (2017), arXiv:1705.07764 [hep-lat].
- [27] Y. Shimizu and Y. Kuramashi, Phys. Rev. **D90**, 074503 (2014), arXiv:1408.0897 [hep-lat].
- [28] Y. Shimizu and Y. Kuramashi, Phys. Rev. **D90**, 014508 (2014), arXiv:1403.0642 [hep-lat].
- [29] Y. Shimizu and Y. Kuramashi, Phys. Rev. **D97**, 034502 (2018), arXiv:1712.07808 [hep-lat].
- [30] S. Takeda and Y. Yoshimura, PTEP **2015**, 043B01 (2015), arXiv:1412.7855 [hep-lat].
- [31] C. Gattringer, M. Giuliani, and O. Orasch, Phys. Rev. Lett. **120**, 241601 (2018), arXiv:1804.01580 [hep-lat].
- [32] K. G. Wilson, Phys. Rev. **D10**, 2445 (1974), [,319(1974)].
- [33] K. G. Wilson, in *New Phenomena in Subnuclear Physics: Proceedings, International School of Subnuclear Physics, Erice, Sicily, Jul 11-Aug 1 1975. Part A* (1975) p. 99, [,0069(1975)].
- [34] H. B. Nielsen and M. Ninomiya, Nucl. Phys. **B185**, 20 (1981), [,533(1980)].
- [35] H. B. Nielsen and M. Ninomiya, Nucl. Phys. **B193**, 173 (1981).
- [36] D. Friedan, Commun. Math. Phys. **85**, 481 (1982).
- [37] D. B. Kaplan, Phys. Lett. **B288**, 342 (1992), arXiv:hep-lat/9206013 [hep-lat].
- [38] Y. Shamir, Nucl. Phys. **B406**, 90 (1993), arXiv:hep-lat/9303005 [hep-lat].
- [39] V. Furman and Y. Shamir, Nucl. Phys. **B439**, 54 (1995), arXiv:hep-lat/9405004 [hep-lat].
- [40] P. H. Ginsparg and K. G. Wilson, Phys. Rev. **D25**, 2649 (1982).
- [41] R. C. Brower, H. Neff, and K. Orginos, Comput. Phys. Commun. **220**, 1 (2017),

- arXiv:1206.5214 [hep-lat].
- [42] X.-L. Qi, T. Hughes, and S.-C. Zhang, Phys. Rev. **B78**, 195424 (2008), arXiv:0802.3537 [cond-mat.mes-hall].
 - [43] X.-L. Qi, Y.-S. Wu, and S.-C. Zhang, Phys. Rev. **B74**, 085308 (2006), arXiv:0505308 [cond-mat.mes-hall].
 - [44] C. L. Kane and E. J. Mele, Phys. Rev. Lett. **95**, 226801 (2005), arXiv:cond-mat/0411737 [cond-mat.mes-hall].
 - [45] S. Elitzur, Phys. Rev. **D12**, 3978 (1975).
 - [46] J. B. Kogut and L. Susskind, Phys. Rev. **D11**, 395 (1975).
 - [47] L. H. Karsten, Phys. Lett. **104B**, 315 (1981).
 - [48] F. Wilczek, Phys. Rev. Lett. **59**, 2397 (1987).
 - [49] M. Creutz, JHEP **04**, 017 (2008), arXiv:0712.1201 [hep-lat].
 - [50] A. Borici, Phys. Rev. **D78**, 074504 (2008), arXiv:0712.4401 [hep-lat].
 - [51] M. Creutz and T. Misumi, Phys. Rev. **D82**, 074502 (2010), arXiv:1007.3328 [hep-lat].
 - [52] S. Durr and G. Koutsou, Phys. Rev. **D83**, 114512 (2011), arXiv:1012.3615 [hep-lat].
 - [53] S. D. Drell, M. Weinstein, and S. Yankielowicz, Phys. Rev. **D14**, 487 (1976).
 - [54] J. Bartels and G. Kramer, Z. Phys. **C20**, 159 (1983).
 - [55] M. Kato, M. Sakamoto, and H. So, JHEP **05**, 057 (2008), arXiv:0803.3121 [hep-lat].
 - [56] G. Bergner, JHEP **01**, 024 (2010), arXiv:0909.4791 [hep-lat].
 - [57] A. D’Adda, N. Kawamoto, and J. Saito, JHEP **12**, 089 (2017), arXiv:1706.02615 [hep-lat].
 - [58] G. Bergner, T. Kaestner, S. Uhlmann, and A. Wipf, Annals Phys. **323**, 946 (2008), arXiv:0705.2212 [hep-lat].
 - [59] D. Weingarten and B. Velikson, Nucl. Phys. **B270**, 10 (1986).
 - [60] O. F. Hernandez and B. R. Hill, Phys. Lett. **B178**, 405 (1986).
 - [61] M. Gross, G. P. Lepage, and P. E. L. Rakow, Phys. Lett. **B197**, 183 (1987).
 - [62] M. Bernaschi, S. Cabasino, E. Marinari, and R. Sarno, Phys. Lett. **B228**, 383 (1989).
 - [63] S. Higashikawa, M. Nakagawa, and M. Ueda, (2018), arXiv:1806.06868 [cond-mat.mes-hall].
 - [64] E. Follana, Q. Mason, C. Davies, K. Hornbostel, G. P. Lepage, J. Shigemitsu, H. Trotter, and K. Wong (HPQCD, UKQCD), Phys. Rev. **D75**, 054502 (2007), arXiv:hep-lat/0610092 [hep-lat].
 - [65] P. Lepage, *Lattice QCD on parallel computers. Proceedings, International Workshop*,

- Tsukuba, Japan, March 10-15, 1997*, Nucl. Phys. Proc. Suppl. **60A**, 267 (1998), [,267(1997)], arXiv:hep-lat/9707026 [hep-lat].
- [66] G. P. Lepage, Phys. Rev. **D59**, 074502 (1999), arXiv:hep-lat/9809157 [hep-lat].
- [67] E. Zohar, J. I. Cirac, and B. Reznik, Rept. Prog. Phys. **79**, 014401 (2016), arXiv:1503.02312 [quant-ph].
- [68] G. Magnifico, D. Vodola, E. Ercolessi, S. P. Kumar, M. Müller, and A. Bermudez, (2018), arXiv:1804.10568 [cond-mat.quant-gas].
- [69] E. Zohar, J. I. Cirac, and B. Reznik, Phys. Rev. **A88**, 023617 (2013), arXiv:1303.5040 [quant-ph].
- [70] J. H. Weber, *Properties of minimally doubled fermions*, Ph.D. thesis, Mainz U. (2015), arXiv:1706.07104 [hep-lat].
- [71] B. Sheikholeslami and R. Wohlert, Nucl. Phys. **B259**, 572 (1985).
- [72] R. Frezzotti, P. A. Grassi, S. Sint, and P. Weisz (Alpha), JHEP **08**, 058 (2001), arXiv:hep-lat/0101001 [hep-lat].
- [73] R. Frezzotti, P. A. Grassi, S. Sint, and P. Weisz, *Lattice field theory. Proceedings, 17th International Symposium, Lattice'99, Pisa, Italy, June 29-July 3, 1999*, Nucl. Phys. Proc. Suppl. **83**, 941 (2000), arXiv:hep-lat/9909003 [hep-lat].
- [74] R. Frezzotti and G. C. Rossi, JHEP **08**, 007 (2004), arXiv:hep-lat/0306014 [hep-lat].
- [75] H. Neuberger, Phys. Lett. **B427**, 353 (1998), arXiv:hep-lat/9801031 [hep-lat].
- [76] P. Hernandez, K. Jansen, and M. Luscher, Nucl. Phys. **B552**, 363 (1999), arXiv:hep-lat/9808010 [hep-lat].
- [77] T.-W. Chiu, Phys. Rev. Lett. **90**, 071601 (2003), arXiv:hep-lat/0209153 [hep-lat].
- [78] G. Cossu, H. Fukaya, S. Hashimoto, and A. Tomiya (JLQCD), Phys. Rev. **D93**, 034507 (2016), arXiv:1510.07395 [hep-lat].
- [79] N. H. Christ and G. Liu, *Lattice field theory. Proceedings, 21st International Symposium, Lattice 2003, Tsukuba, Japan, July 15-19, 2003*, Nucl. Phys. Proc. Suppl. **129**, 272 (2004), [,272(2004)].
- [80] M. Tomii, Phys. Rev. **D96**, 074504 (2017), arXiv:1706.03099 [hep-lat].
- [81] S. Aoki, T. Izubuchi, Y. Kuramashi, and Y. Taniguchi, Phys. Rev. **D67**, 094502 (2003), arXiv:hep-lat/0206013 [hep-lat].
- [82] K. G. Chetyrkin, J. H. Kuhn, and C. Sturm, Eur. Phys. J. **C48**, 107 (2006), arXiv:hep-

- ph/0604234 [hep-ph].
- [83] R. Boughezal, M. Czakon, and T. Schutzmeier, Phys. Rev. **D74**, 074006 (2006), arXiv:hep-ph/0605023 [hep-ph].
- [84] A. H. Hoang, V. Mateu, and S. Mohammad Zebarjad, Nucl. Phys. **B813**, 349 (2009), arXiv:0807.4173 [hep-ph].
- [85] Y. Kiyo, A. Maier, P. Maierhofer, and P. Marquard, Nucl. Phys. **B823**, 269 (2009), arXiv:0907.2120 [hep-ph].
- [86] D. Greynat and S. Peris, Phys. Rev. **D82**, 034030 (2010), [Erratum: Phys. Rev.D82,119907(2010)], arXiv:1006.0643 [hep-ph].
- [87] D. Greynat, P. Masjuan, and S. Peris, Phys. Rev. **D85**, 054008 (2012), arXiv:1104.3425 [hep-ph].
- [88] V. A. Novikov, L. B. Okun, M. A. Shifman, A. I. Vainshtein, M. B. Voloshin, and V. I. Zakharov, Phys. Rept. **41**, 1 (1978).
- [89] C. Morningstar and M. J. Peardon, Phys. Rev. **D69**, 054501 (2004), arXiv:hep-lat/0311018 [hep-lat].
- [90] M. Luscher, JHEP **08**, 071 (2010), [Erratum: JHEP03,092(2014)], arXiv:1006.4518 [hep-lat].
- [91] S. Borsanyi *et al.*, JHEP **09**, 010 (2012), arXiv:1203.4469 [hep-lat].
- [92] T. Kaneko, S. Aoki, G. Cossu, H. Fukaya, S. Hashimoto, and J. Noaki (JLQCD), *Proceedings, 31st International Symposium on Lattice Field Theory (Lattice 2013): Mainz, Germany, July 29-August 3, 2013*, PoS **LATTICE2013**, 125 (2014), arXiv:1311.6941 [hep-lat].
- [93] J. Noaki, S. Aoki, G. Cossu, H. Fukaya, S. Hashimoto, and T. Kaneko (JLQCD), *Proceedings, 31st International Symposium on Lattice Field Theory (Lattice 2013): Mainz, Germany, July 29-August 3, 2013*, PoS **LATTICE2013**, 263 (2014).
- [94] H. Fukaya, S. Aoki, G. Cossu, S. Hashimoto, T. Kaneko, and J. Noaki (JLQCD), Phys. Rev. **D92**, 111501 (2015), arXiv:1509.00944 [hep-lat].
- [95] M. Tomii, G. Cossu, B. Fahy, H. Fukaya, S. Hashimoto, and J. Noaki (JLQCD), (2015), arXiv:1511.09170 [hep-lat].
- [96] B. Fahy, G. Cossu, S. Hashimoto, T. Kaneko, J. Noaki, and M. Tomii (JLQCD), *Proceedings, 33rd International Symposium on Lattice Field Theory (Lattice 2015): Kobe, Japan, July 14-18, 2015*, PoS **LATTICE2015**, 074 (2016), arXiv:1512.08599 [hep-lat].
- [97] G. Cossu, J. Noaki, S. Hashimoto, T. Kaneko, H. Fukaya, P. A. Boyle, and J. Doi, in

- Proceedings, 31st International Symposium on Lattice Field Theory (Lattice 2013): Mainz, Germany, July 29-August 3, 2013* (2013) arXiv:1311.0084 [hep-lat].
- [98] M. Tomii, G. Cossu, B. Fahy, H. Fukaya, S. Hashimoto, T. Kaneko, and J. Noaki (JLQCD), *Phys. Rev.* **D94**, 054504 (2016), arXiv:1604.08702 [hep-lat].
- [99] B. Dehnadi, A. H. Hoang, and V. Mateu, *Proceedings, 7th International Workshop on Charm Physics, CHARM 2015: Detroit, USA, May 18-22, 2015*, *JHEP* **08**, 155 (2015), arXiv:1504.07638 [hep-ph].
- [100] D. J. Broadhurst, P. A. Baikov, V. A. Ilyin, J. Fleischer, O. V. Tarasov, and V. A. Smirnov, *Phys. Lett.* **B329**, 103 (1994), arXiv:hep-ph/9403274 [hep-ph].
- [101] B. V. Geshkenbein, B. L. Ioffe, and K. N. Zyablyuk, *Phys. Rev.* **D64**, 093009 (2001), arXiv:hep-ph/0104048 [hep-ph].
- [102] B. L. Ioffe and K. N. Zyablyuk, *Eur. Phys. J.* **C27**, 229 (2003), arXiv:hep-ph/0207183 [hep-ph].
- [103] B. L. Ioffe, *Prog. Part. Nucl. Phys.* **56**, 232 (2006), arXiv:hep-ph/0502148 [hep-ph].
- [104] S. Narison, *Phys. Lett.* **B706**, 412 (2012), arXiv:1105.2922 [hep-ph].
- [105] C. T. H. Davies, E. Follana, I. D. Kendall, G. P. Lepage, and C. McNeile (HPQCD), *Phys. Rev.* **D81**, 034506 (2010), arXiv:0910.1229 [hep-lat].
- [106] K. A. Olive *et al.* (Particle Data Group), *Chin. Phys.* **C38**, 090001 (2014).
- [107] C. Alexandrou, V. Drach, K. Jansen, C. Kallidonis, and G. Koutsou, *Phys. Rev.* **D90**, 074501 (2014), arXiv:1406.4310 [hep-lat].
- [108] N. Carrasco *et al.* (European Twisted Mass), *Nucl. Phys.* **B887**, 19 (2014), arXiv:1403.4504 [hep-lat].
- [109] Y. Maezawa and P. Petreczky, *Phys. Rev.* **D94**, 034507 (2016), arXiv:1606.08798 [hep-lat].
- [110] Y.-B. Yang *et al.*, *Phys. Rev.* **D92**, 034517 (2015), arXiv:1410.3343 [hep-lat].
- [111] J. Heitger, G. M. von Hippel, S. Schaefer, and F. Virotta, *Proceedings, 31st International Symposium on Lattice Field Theory (Lattice 2013): Mainz, Germany, July 29-August 3, 2013*, *PoS LATTICE2013*, 475 (2014), arXiv:1312.7693 [hep-lat].
- [112] K. Jansen, M. Petschlies, and C. Urbach, *Proceedings, 29th International Symposium on Lattice field theory (Lattice 2011): Squaw Valley, Lake Tahoe, USA, July 10-16, 2011*, *PoS LATTICE2011*, 234 (2011), arXiv:1111.5252 [hep-lat].
- [113] B. Blossier, P. Dimopoulos, R. Frezzotti, V. Lubicz, M. Petschlies, F. Sanfilippo, S. Simula,

- and C. Tarantino (ETM), Phys. Rev. **D82**, 114513 (2010), arXiv:1010.3659 [hep-lat].
- [114] T. Banks and A. Casher, Nucl. Phys. **B169**, 103 (1980).
- [115] H. Fukaya, S. Aoki, S. Hashimoto, T. Kaneko, J. Noaki, T. Onogi, and N. Yamada (JLQCD), Phys. Rev. Lett. **104**, 122002 (2010), [Erratum: Phys. Rev. Lett.105,159901(2010)], arXiv:0911.5555 [hep-lat].
- [116] H. Fukaya, S. Aoki, T. W. Chiu, S. Hashimoto, T. Kaneko, J. Noaki, T. Onogi, and N. Yamada (TWQCD, JLQCD), Phys. Rev. **D83**, 074501 (2011), arXiv:1012.4052 [hep-lat].
- [117] L. Giusti and M. Luscher, JHEP **03**, 013 (2009), arXiv:0812.3638 [hep-lat].
- [118] M. Tomii, G. Cossu, B. Fahy, H. Fukaya, S. Hashimoto, T. Kaneko, and J. Noaki (JLQCD), Phys. Rev. **D96**, 054511 (2017), arXiv:1703.06249 [hep-lat].
- [119] G. S. Bali, C. Bauer, and A. Pineda, Phys. Rev. **D89**, 054505 (2014), arXiv:1401.7999 [hep-ph].
- [120] G. S. Bali, C. Bauer, A. Pineda, and C. Torrero, Phys. Rev. **D87**, 094517 (2013), arXiv:1303.3279 [hep-lat].
- [121] A. Patella, Phys. Rev. **D86**, 025006 (2012), arXiv:1204.4432 [hep-lat].
- [122] A. Cheng, A. Hasenfratz, G. Petropoulos, and D. Schaich, JHEP **07**, 061 (2013), arXiv:1301.1355 [hep-lat].
- [123] K. Cichy, JHEP **08**, 127 (2014), arXiv:1311.3572 [hep-lat].
- [124] L. Del Debbio and R. Zwicky, Phys. Rev. **D82**, 014502 (2010), arXiv:1005.2371 [hep-ph].
- [125] P. A. Baikov, K. G. Chetyrkin, and J. H. Kuhn, JHEP **10**, 076 (2014), arXiv:1402.6611 [hep-ph].
- [126] P. A. Baikov, K. G. Chetyrkin, and J. H. Kuhn, Phys. Rev. Lett. **118**, 082002 (2017), arXiv:1606.08659 [hep-ph].
- [127] P. A. Boyle (UKQCD), *Proceedings, 32nd International Symposium on Lattice Field Theory (Lattice 2014): Brookhaven, NY, USA, June 23-28, 2014*, PoS **LATTICE2014**, 087 (2015).
- [128] Z. Fodor, K. Holland, J. Kuti, S. Mondal, D. Nogradi, and C. H. Wong, *Proceedings, 33rd International Symposium on Lattice Field Theory (Lattice 2015): Kobe, Japan, July 14-18, 2015*, PoS **LATTICE2015**, 310 (2016), arXiv:1605.08091 [hep-lat].
- [129] C. Patrignani *et al.* (Particle Data Group), Chin. Phys. **C40**, 100001 (2016).
- [130] A. Bazavov, N. Brambilla, X. Garcia i Tormo, P. Petreczky, J. Soto, and A. Vairo, Phys. Rev. **D90**, 074038 (2014), arXiv:1407.8437 [hep-ph].

- [131] S. Aoki *et al.* (PACS-CS), JHEP **10**, 053 (2009), arXiv:0906.3906 [hep-lat].
- [132] K. Maltman, D. Leinweber, P. Moran, and A. Sternbeck, Phys. Rev. **D78**, 114504 (2008), arXiv:0807.2020 [hep-lat].
- [133] N. Prokof'ev and B. Svistunov, Phys. Rev. Lett. **87**, 160601 (2001).
- [134] M. Giuliani and C. Gattringer, (2017), arXiv:1702.04771 [hep-lat].
- [135] S. Catterall and E. Gregory, Phys. Lett. **B487**, 349 (2000), arXiv:hep-lat/0006013 [hep-lat].
- [136] E. Witten, Nucl. Phys. **B188**, 513 (1981).
- [137] E. Witten, Nucl. Phys. **B202**, 253 (1982).
- [138] D. Kadoh and K. Nakayama, (2018), arXiv:1803.07960 [hep-lat].
- [139] D. Kadoh and K. Nakayama, (2018), arXiv:1812.10642 [hep-lat].
- [140] G. P. Lepage and P. B. Mackenzie, Phys. Rev. **D48**, 2250 (1993), arXiv:hep-lat/9209022 [hep-lat].
- [141] A. S. Kronfeld, *The International Symposium on Lattice Field Theory: Lattice 92 Amsterdam, Netherlands, September 15-19, 1992*, Nucl. Phys. Proc. Suppl. **30**, 445 (1993), arXiv:hep-lat/9211043 [hep-lat].